Physics of the Neutrino Factory and Related Long Baseline Designs

TESIS DOCTORAL

Jordi Burguet Castell

2008

Table of contents

Abstract . . . 0

1 Introduction . . . 1

1.1 Overview . . . 1
1.2 Historical Context . . . 1
1.2.1 Discovery of the Neutrino . . . 1
1.2.2 The Solar Neutrino Problem . . . 2
1.2.3 The Atmospheric Neutrino Problem . . . 5
1.3 Theoretical Framework . . . 8
1.3.1 Neutrino Flavors . . . 8
1.3.1.1 Why Three? . . . 9
1.3.2 Dirac and Majorana . . . 10
1.3.3 Neutrino Mass . . . 10
1.3.4 Mixing . . . 11
1.3.4.1 2-Family Mixing . . . 11
1.3.4.2 3-Family Mixing . . . 12
1.3.5 Matter Effects . . . 14

2 The Neutrino Factory . . . 17

2.1 Origin of the Idea . . . 17
2.2 Characteristics . . . 17
2.3 General Design . . . 18
2.4 Muon Beams, Fluxes and Rates . . . 20
2.5 Wrong Sign Muons . . . 22
2.6 Detection . . . 23
2.6.1 A Large Magnetized Calorimeter . . . 23
2.7 Oscillation Physics at the Neutrino Factory . . . 24
2.7.1 Oscillation Probabilities in Matter . . . 24
2.7.2 Precision Measurement of Known Oscillations . . . 25
2.7.3 Sensitivity to θ_{13} . . . 26
2.7.4 Sensitivity to CP violation . . . 26

3 Reducing Uncertainties . . . 29

3.1 HARP's Measure of Hadronic Cross-Sections . . . 29
3.2 Forward Tracking and Particle Identification . . . 30
3.2.1 Tracking . . . 30

3.2.2 Particle Identification . . . 31
3.3 Implications for Neutrino Physics . . . 31
3.3.1 MiniBooNE and SciBooNE . . . 31
3.3.2 K2K . . . 34
3.3.3 Atmospheric Neutrinos . . . 37
3.3.4 Neutrino Factory . . . 38

4 Suppressing Correlations and Degeneracies . . . 39

4.1 Superbeams as an Intermediate Step . . . 39
4.1.1 Rationale . . . 39
4.1.2 Neutrino Generation in a Superbeam . . . 40
4.1.3 Detection . . . 42
4.1.4 Water Cerenkov Detectors . . . 42
4.1.5 Sensitivity . . . 43
4.1.5.1 Sensitivity to the Atmospheric Parameters . . . 43
4.1.5.2 Sensitivity to CP violation . . . 44
4.2 Correlations . . . 45
4.3 Degeneracies . . . 46
4.4 Status at the Neutrino Factory . . . 47
4.4.1 Correlation Between δ and θ_{13} . . . 48
4.4.2 Intrinsic Degeneracies . . . 49
4.4.2.1 Atmospheric Regime . . . 49
4.4.2.2 Solar Regime . . . 51
4.4.3 Simultaneous Determination of δ and θ_{13} . . . 51
4.4.3.1 Atmospheric Regime . . . 52
4.4.3.2 Solar Regime . . . 54
4.5 Combinations . . . 54
4.5.1 Neutrino Factory with Superbeam . . . 55
4.5.2 Resolution of Intrinsic Degeneracies . . . 55
4.5.2.1 Effect of Δm^2_{23} . . . 59
4.5.2.2 Effect of Δm^2_{12} . . . 60
4.5.3 sign(Δm^2_{23}) Degeneracy . . . 62
4.5.4 $\theta_{23} \to \pi/2 - \theta_{23}$ Degeneracy . . . 66
4.5.4.1 Atmospheric Regime . . . 67
4.5.4.2 Solar Regime . . . 70
4.5.5 The Silver Channels . . . 72
4.5.5.1 Resolving Intrinsic Degeneracies . . . 72
4.5.5.2 Resolving Fake θ_{23} Solutions . . . 72
4.5.5.3 Resolving Fake sign(Δm^2_{23}) Solutions . . . 73

5 New Long Baseline Experiments: How It All Fits Together . . . 75

5.1 Beta Beam . . . 75
5.1.1 Energy Regimes . . . 76
5.1.2 Neutrino Fluxes . . . 78

5.1.3 Measurements . . . 80
5.1.4 Cross-Sections . . . 80
5.1.5 Detectors: Efficiencies and Backgrounds . . . 81
5.1.5.1 Signal Selection and Background Suppression in Water . . . 82
5.1.5.2 Atmospheric Background . . . 83
5.1.6 Systematic Errors . . . 86
5.1.7 Signal and Backgrounds in Setup-1 . . . 86
5.1.8 Signal and Backgrounds in Setup-2 . . . 88
5.1.9 Setup-3 . . . 91
5.1.10 Optimization of the SPS β-beam . . . 91
5.1.10.1 Optimal γ for the CERN-Fréjus baseline . . . 92
5.1.10.2 Optimal L for maximum ion acceleration $\gamma = 150$ . . . 93
5.1.11 Determination of θ_{13} and δ . . . 95
5.1.11.1 Setups 1–3 . . . 95
5.1.11.2 Setups 4–6 . . . 97
5.1.12 Determination of sign(Δm^2_{23}) . . . 99
5.1.13 Effect of the Eight-fold Degeneracies . . . 100
5.2 Electron-Capture Beam . . . 102
5.2.1 Neutrino Flux . . . 104
5.2.2 Physics with an EC-beam . . . 105
5.2.3 Considered Setups . . . 106
5.2.3.1 Perspectives for Setup I . . . 106
5.2.3.2 Perspectives for Setup II . . . 107

6 Conclusions . . . 111

Appendix A Software Tools and Design . . . 113

A.1 Numerical Simulations . . . 113
A.2 Implementation . . . 113
A.3 Availability . . . 115

Bibliography . . . 117

Abstract

The discovery of neutrino oscillations confirmed that neutrinos are massive. It also showed that the flavor and mass eigenstates are mixed in a way similar to the one described by the CKM matrix in the quark sector. We have now fully entered an era of precision measurements of the parameters that govern these oscillations.

Past experiments have provided a 3-family oscillation scenario and many parameters have been measured ($\theta_{12(\mathrm{sol})}$, $\theta_{23(\mathrm{atm})}$, $\Delta m^2_{12(\mathrm{sol})}$, $|\Delta m^2_{23(\mathrm{atm})}|$ and upper limits in $\theta_{13(\mathrm{interference})}$). The current and future neutrino experiments aim to complete this scenario: more precise measurements of the known parameters, the measure of $\mathrm{sign}(\Delta m^2_{23})$ which determines the mass hierarchy (normal with ν_1 lighter, or inverted with ν_1 heavier than ν_2 and ν_3) and, most excitingly, the discovery of $\theta_{13} > 0$ and δ which, if different from 0° and 180°, would mean the existence of CP violation in the leptonic sector.

Different accelerator-based long baseline experiments have been proposed. They present different merits, drawbacks and synergies. This sets the stage for this work. We have explored the physics reach of the Neutrino Factory, the ultimate machine in terms of precision. It produces neutrinos from the decay of muons, giving a background-free beam and the suppressed transition $\nu_e \rightsquigarrow \nu_\mu$, where the CP-violation observables are best seen due to the interference of the solar and atmospheric terms. We explore the appearance of correlations and degeneracies which affect the reconstruction, search for their origin and propose different ways to handle them. Related setups have been more recently proposed, and are also affected by these phenomena, although in different ways. We explore the physics potential of super-beams (high-intensity neutrino beams from the decay of pions), β-beams (pure neutrino beams from the β-decay of accelerated radioactive ions) and electron-capture beams (monochromatic neutrino beams from EC-unstable ions). With the goal of maximizing their separate and joint sensitivity to the neutrino oscillation parameters, we optimize their designs.

Acknowledgments

I would like to express my gratitude to those who gave me the possibility to complete this thesis. First of all to Juan José Gómez-Cadenas, for mindlessly embarking me into the world of neutrino physics and trusting in my ability. His ideas have been a major drive for this work, as much as his energy and enthusiasm. Equally my thanks go to Pilar Hernández, who has directed my work as much as Juanjo has. Her sharp insights as to what are the important questions to ask and how to attack them has been invaluable. Their talents have beautifully combined to produce the main results presented in this thesis in which I had the fortune to participate.

During my first contact with high energy physics I enjoyed the company of Arán García-Bellido, fresh and always ready for a laugh, and Graham Hollyman, an outstanding example of what interest and dedication can accomplish no-matter-what, and a very kind person. At that time I also met Christian Hansen, happy and energetic, who has reappeared recently and has helped me with the revisions. I thank them all for their help and the good times we spent together.

I also thank Irene Torres, who I was lucky to meet in my first PhD courses. She helped me to cope with my daily work, survive bureaucracy and sweetened every day with her wonderful character.

The long delay in writing this thesis was more than compensated by the enjoyable time I spent with the bioinformatics group at CIPF. They have been very friendly and also helped by pestering me to finish my thesis for good. That, and many other things, for which I warmly thank Fátima Al-Shahrour, Eva Alloza, Leonardo Arbiza, Emidio Capriotti, Lucía Conde, Hernán Dopazo, Jaime Huerta, David Montaner and the rest of the group.

Thanks to my friends in the neutrino group, old and new, who fight happily with neutrinos one way or another: Anselmo Cervera, Ana Tornero, Pau Novella, Elena Couce, Joan Catalá, Olga Mena, Justo Martín, Laura Monfregola, Francesc Monrabal, Javier Muñoz and Michel Sorel. Hunting for neutrinos would not have been half the fun without them.

To Miguel Nebot, for being always ready to help and indeed helping me multiple times as if it were nothing, and for his good will.

To my parents, who always allowed me to follow my interests and have had to wait long before seeing this thesis done.

To my little sister Elena, nice and cheerful, that had far less doubts than myself that I would finish this thesis someday.

To my friends Manuel Cifrián, Joaquín D'Opazo, Jaume Escobedo, Gaspar Fernández and Jose Manuel Martí, for their help, their support and for making so many moments special.

Last but not least, to Sara, for helping me during all these years in so many different ways, for making this world a better place and for her charming smile. I am really fortunate that we can share this and look forward for our future adventures.

Resumen

Introducción

La física de neutrinos ha proporcionado la primera evidencia de física más allá del Modelo Estándar. Durante los últimos 35 años se han llevado a cabo una serie de experimentos con resultados que no se ajustan a lo esperado según este modelo. Hoy en día estos enigmas se pueden explicar gracias a la existencia de las oscilaciones de neutrinos.

Existen tres tipos ("sabores") de neutrinos (más sus correspondientes antipartículas), relacionados por las corrientes cargadas con el electrón y sus compañeros más masivos el muón y el tau respectivamente, por lo que reciben los nombres de neutrino electrónico, muónico y tauónico (ν_e, ν_μ, ν_τ). En la formulación original del Modelo Estándar ninguno de ellos tiene masa, lo que era compatible con lo observado en los experimentos. Es a través del fenómeno de las oscilaciones de neutrinos como se ha comprobado indirectamente que de hecho son masivos, y su masa es extraordinariamente pequeña: unos 7 órdenes de magnitud menor que la de la siguiente partícula más ligera, el electrón.

Descubrimiento

Los neutrinos son unas de las pocas partículas fundamentales que forman la naturaleza. Son parecidos a un electrón sin carga eléctrica: al igual que éstos sufren la interacción débil y no sienten la interacción fuerte como los quarks, pero tampoco la electromagnética. Su existencia fue primero postulada por Wolfgang Pauli en 1930 para explicar por qué los electrones que resultan de la desintegración β no tienen una energía fija. En la desintegración se produciría también una partícula muy ligera, neutra y de spin $1/2$ para que se conservara la energía, la carga eléctrica y el momento angular. Fermi propuso la primera teoría de la desintegración β con la que se pudo predecir la probabilidad de interacción de los neutrinos con la materia (su "sección eficaz"), que resultó ser extremadamente pequeña.

En 1956 Cowan y Reines detectaron experimentalmente el primer neutrino (en realidad, el primer *anti*neutrino), y ese mismo año Pontecorvo estudió la posibilidad de que el neutrino oscilara en antineutrino, construyendo así la primera teoría de oscilaciones de neutrinos. Seis años después se descubrió la existencia de otro tipo de neutrino, el neutrino muónico ν_μ, y también se encontró que los neutrinos sólo pueden oscilar de un tipo a otro si tienen distintas masas.

Neutrinos solares y atmosféricos

Como consecuencia de las reacciones nucleares que se producen en el interior del Sol se generan neutrinos con distintas energías, y estos se pueden detectar al llegar a la Tierra. El número de neutrinos esperado se puede estimar a partir del Modelo Estándar Solar (SSM), pero desde los primeros resultados en 1968 por Davis, Bahcall y Harmer el número de neutrinos observado es menor que el predicho.

A este problema de detectar menos neutrinos solares que los esperados se añadió otro similar en la década siguiente con los neutrinos muónicos producidos en la interacción de los rayos cósmicos con la atmósfera. La cantidad de neutrinos muónicos respecto a la de neutrinos electrónicos era menor que la esperada.

Finalmente, Super-Kamiokande mostró que aunque la cantidad de neutrinos electrónicos no dependía del ángulo con el que llegaban, la de neutrinos muónicos sí, justo de la forma esperada si los neutrinos muónicos oscilan a otra especie de neutrino no detectada.

Oscilaciones

Los autoestados de sabor de los neutrinos no coinciden con los autoestados de masa, de forma similar a la mezcla de los quarks descrita por la matriz CKM. La matriz equivalente en el sector leptónico, llamada PMNS, depende de cuatro parámetros: tres ángulos de mezcla (θ_{12}, θ_{23}, θ_{13}) y una fase (δ). Las oscilaciones dependen de la forma de esta matriz y de las diferencias de masa al cuadrado entre los distintos neutrinos (Δm^2_{12}, Δm^2_{23}).

Las oscilaciones de neutrinos solares están gobernadas principalmente por θ_{12} y Δm^2_{12}, mientras que la de los atmosféricos lo están por θ_{23} y Δm^2_{23}. Del valor de θ_{13} sólo se sabe que es $\lesssim 10°$, y para conocerlo, así como para encontrar también el valor de δ, existen una serie de experimentos propuestos para realizar en los próximos años.

En esta tesis se discuten estos experimentos, basados en haces de neutrinos provenientes de aceleradores. La señal principal es $\nu_e \leftrightsquigarrow \nu_\mu$ (y $\bar{\nu}_e \leftrightsquigarrow \bar{\nu}_\mu$), donde los observables relacionados con violación CP se ven mejor gracias a la interferencia del término solar y atmosférico. Todos estos experimentos se ven afectados por la existencia de correlaciones y degeneraciones, aunque de forma distinta y con la posibilidad de combinar resultados para resolverlas.

La Neutrino Factory

En una Neutrino Factory los neutrinos se producen por la desintegración de muones ($\mu^- \to e^- \, \bar{\nu}_e \, \nu_\mu$ y $\mu^+ \to e^+ \, \nu_e \, \bar{\nu}_\mu$) circulando en un anillo de almacenamiento. Esto produce un haz con sólo dos especies de neutrinos, sin otra contaminación. Los ν_μ que no oscilan producen en el detector un muón del mismo signo que el original, μ^-, pero si los $\bar{\nu}_e$ del haz oscilan $\bar{\nu}_e \rightsquigarrow \bar{\nu}_\mu$, el $\bar{\nu}_\mu$ producirá un muón de "signo equivocado", un μ^+. Así, con un detector capaz de diferenciar la carga del leptón producido, la señal de muones de signo equivocado es una indicación precisa de que se han producido oscilaciones.

La medida de muones de signo equivocado requiere un detector masivo del orden de 50 kton, con capacidad de identificar muones y medir su carga. El detector considerado aquí es un calorímetro de hierro magnetizado, similar a MINOS. Aplicando cortes fuertes en el momento del muón y su identificación, el background por la desintegración de otras partículas que se identifiquen incorrectamente se puede reducir tanto como un factor 10^6, a la vez que se mantiene una eficiencia de un 40%.

La mayor focalización del haz con la energía de los muones junto al rápido crecimiento de la sección eficaz con la energía de los neutrinos en el régimen fuertemente inelástico hace que sea conveniente ir a distancias más grandes a E/L constante. Sin embargo, a partir de unos pocos miles de kilómetros los efectos de materia reducen fuertemente a la probabilidad de oscilación. El efecto combinado lleva a un diseño en el que la Neutrino Factory trabaja a un E/L mayor que el correspondiente al pico de la oscilación a pequeñas distancias, con una energía del orden de 30 GeV y una distancia de unos 3000 km.

Superbeams

El desarrollo de fuentes de alta intesidad que se requiere para la Neutrino Factory sugirió explorar el potencial de los haces convencionales de neutrinos con alta intensidad que podrían producirse con un proton driver similar. Los haces convencionales provienen de la producción de piones, π^+ o π^- que son seleccionados con un cuerno electromagnético para después desintegrarse en neutrinos $\pi^\pm \rightarrow \mu^\pm\ \nu_\mu(\bar{\nu}_\mu)$. Los experimentos hechos con estos haces están siempre limitados por la presencia en el propio haz de una componenente de $\nu_e(\bar{\nu}_e)$ que proviene de la desintegración de los $\mu^\pm$, que es un background irreducible en la búsqueda de oscilaciones $\nu_\mu \rightsquigarrow \nu_e$. Aún así, la alta intensidad de estos haces junto con el uso de detectores masivos les permiten mejorar sensiblemente nuestro conocimiento de θ_{13}, e incluso tener cierta sensibilidad al valor de la fase de violación CP δ.

Las distancias típicas entre la fuente y el detector en un Superbeam están en el rango $150-300$ km, en el pico de oscilación. La detección de neutrinos de baja energía (comparados con la Neutrino Factory) a esas distancias precisa de un detector masivo con eficiencia alta. Para buscar la aparición de ν_e se requiere poder rechazar fuertemente el background correspondiente a la identificación equivocada de μ y a la producción de π^0 por corrientes neutras. Los detectores Cerenkov de agua son especialmente apropiados para esta tarea.

Los Superbeams son capaces de medir con precisión los parámetros atmosféricos θ_{23} y Δm^2_{23}. Sin embargo la medida de θ_{13} está correlacionada con δ y la mejor forma de medir ambas cantidades es combinando las polaridades con neutrinos y antineutrinos. Como la sección eficaz $\bar{\nu}\ +\ ^{16}O$ es unas seis veces menor que la de $\nu +\ ^{16}O$ a esas energías, para poder compensar la baja estadística de antineutrinos, estos deben correr aproximadamente durante 6 veces más que los neutrinos, reduciendo la sensibilidad del experimento.

Reduciendo incertidumbres

Para producir un haz de neutrinos primero se hace colisionar un haz de protones contra un blanco, con lo que se forman piones entre otras partículas. Los piones pueden utilizarse directamente para producir los neutrinos en su desintegración (método usado en los haces convencionales, incluyendo los Superbeams), o bien muones que a su vez se desintegrarán en neutrinos (como en la Neutrino Factory). Las incertidumbres existentes en la sección eficaz de interacción de los protones con el blanco afecta pues al conocimiento preciso del flujo de neutrinos que se obtiene, y por tanto afecta a la sensitividad última de estos experimentos. También en los experimentos sobre neutrinos atmosféricos, una de las principales fuentes de incertidumbre viene de la sección eficaz de interacción de los rayos cósmicos con la atmósfera.

El experimento HARP se diseñó para estudiar con precisión la producción de hadrones para haces de entre 1.5 y 15 GeV/c y blancos nucleares desde el hidrógeno hasta el plomo. El objetivo múltiple es medir la producción de piones para varias energías y materiales relevantes en el diseño del proton driver de la Neutrino Factory, medir también la producción de piones en blancos de bajo número atómico para mejorar la precisión con la que se conoce el flujo de neutrinos atmosféricos, y finalmente medir la producción de piones y kaones relevantes para el cálculo de los flujos de neutrinos en experimentos como MiniBooNE y K2K.

HARP está compuesto de distintos subdetectores que permiten reconstruir las trayectorias de las partículas producidas gracias principalmente a una TPC y varias cámaras de deriva, e identificarlas gracias a un detector Cerenkov, otro de tiempo de vuelo (ToF) y un calorímetro electromagnético.

Los resultados del experimento se traducen en valores estimados, junto con sus incertidumbres y correlaciones, para los parámetros que aparecen en la parametrización empírica de Sanford-Wang de la sección eficaz de producción hadrónica. Estos valores con sus incertidumbres y correlaciones son posteriormente propagados para estimar la incertidumbre en el flujo de neutrinos.

El primer resultado de HARP midió la producción de π^+ en un blanco de aluminio para un momento del haz de protones de 12.9 GeV/c, que se corresponde con las energías del Proton-Sincroton de KEK y al material usado por el experimento K2K. Los resultados se han incorporado en la simulación Monte Carlo del haz de K2K para estimar el espectro de neutrinos en el detector cercano y en SuperKamiokande, y la dependencia en energía del cociente del flujo lejano de neutrinos respecto al cercano en ausencia de oscilaciones. La incertidumbre en el cociente es de 2-3% por debajo de 1 GeV de energía del neutrino, y de 4-9% por encima.

Otro resultado importante es el que afecta al Booster Neutrino Beam en Fermilab. HARP ha medido la sección eficaz de producción de π^+ para un blanco delgado (5% de longitud de interacción) de berilio a un momento del protón de 8.9 GeV/c, que es el utilizado en el BNB. Los resultados se han añadido también a la simulación Monte Carlo del haz de neutrinos en el experimento MiniBooNE.

Existen también resultados para la sección eficaz de producción de $\pi^\pm$ en la colisión de protones a 12 GeV/c con un blanco delgado de carbono, importantes para un cálculo preciso del flujo de neutrinos atmosféricos y para la predicción del desarrollo de las cascadas hadrónicas. También existen resultados para la producción de $\pi^\pm$ en la colisión de protones con tantalio, en un rango de momentos de importancia particular para el diseño de la Neutrino Factory.

Suprimiendo correlaciones y degeneraciones

La fórmula que da la probabilidad de oscilación acopla los parámetros θ_{12}, θ_{23}, θ_{13}, δ, Δm^2_{12} y Δm^2_{23}. En general, cuando un experimento trata de medir varios parámetros simultaneamente, la incertidumbre en cada parámetro dependerá del valor real (pero conocido sólo hasta cierto punto) de todos los demás. Los parámetros están correlacionados en el sentido de que un experimento es sensible principalmente a cierta combinación de parámetros. Una información más débil en otras combinaciones de parámetros permite típicamente desacoplarlos, pero ciertas correlaciones sobreviven.

Las degeneraciones ocurren cuando dos o más grupos de valores ajustan los mismos datos. La forma en que afectan a la medida de un parámetro concreto puede describirse, por ejemplo, citando las incertidumbres asociadas a cada grupo de parámetros por separado, o tomando el rango completo cubierto por las degeneraciones como la incertidumbre de la medida.

Para un solo experimento se pueden suavizar el efecto de las correlaciones e intentar resolver las degeneraciones aprovechando la dependencia en energía de la señal de oscilación, si en el detector se puede reconstruir la energía del leptón producido con una resolución suficiente.

Si se han medido las probabilidades de oscilación tanto para neutrinos como para antineutrinos, para una distancia fija y una energía de los (anti)neutrinos dada, en general existe una segunda solución con valores de (θ_{13}, δ) distintos de los reales. Se trata de la llamada degeneración intrínseca.

En una Neutrino Factory, si θ_{13} no es muy pequeño (dependiendo de la distancia de base, $\theta_{13} \gtrsim 1°$, el "régimen atmosférico"), la dependencia energética de la señal no es suficientemente fuerte como para resolver la degeneración intrínseca. Para una distancia de 2810 km, la segunda solución aparece aislada si $\delta \simeq 0°, 180°$, y es responsable de unas incertidumbres grandes que abarcan desde la región de la solución real a la falsa si $\delta \simeq 90°, -90°$.

Para distancias de $L = 732$ km y 7332 km la medida de δ no es posible, en el primer caso porque hay una línea contínua de soluciones que lo impide si no se conoce θ_{13} previamente, y en el segundo porque la sensitividad a violación CP se pierde por los efectos de materia y la pérdida en el número de sucesos.

Si $\theta_{13} \lesssim 1°$ (dependiendo también de otros valores, el “régimen solar”), la degeneración intrínseca aparece con el δ falso cercano a 180°, imitando las soluciones que corresponden a $\theta_{13} = 0°$. La sensibilidad a violación CP es mucho peor que en el régimen atmosférico.

Combinaciones

Aparte de la degeneración intrínseca, existen otras soluciones falsas que pueden aparecer debido a la degeneración en el signo de Δm^2_{23} y en el octante de θ_{23} ($\theta_{23} \leftrightarrow \pi/2 - \theta_{23}$). No se espera que estas degeneraciones estén resueltas antes de que entre en funcinoamiento un Superbeam o la Neutrino Factory.

Existen distintas estrategias para eliminar estas degeneraciones. Se pueden combinar datos de distintas distancias, mejorar la medida de la energía del neutrino, detectar los canales suplementarios $\nu_e \rightsquigarrow \nu_\tau$ y utilizar detectores *off-axis* para disponer de medidas a distinta $\langle E \rangle$. Nos centraremos en la más prometedora: la combinación de la Neutrino Factory con un Superbeam.

La localización de la solución falsa correspondiente a la degeneración intrínseca es opuesta en el caso de los Superbeams y la Neutrino Factory a 2810 km, debido a que se encuentran a un E/L distinto. Ésta es la mejor combinación en términos de sensibilidad a las degeneraciones tanto para el régimen atmosférico como para el solar.

La degeneración correspondiente al signo de Δm^2_{23} también se resuelve gracias a que en la Neutrino Factory las distancias son tales que los efectos de materia (que dependen del signo de Δm^2_{23}) son importantes, y no para los Superbeams. Así, para $\theta_{13} > 2°$ (en el régimen atmosférico) no hay soluciones falsas usando tan sólo la Neutrino Factory a 2810 km, y hasta $\theta_{13} > 1°$ la combinación con el Superbeam es capaz de resolver la degeneración. Para $\theta_{13} < 1°$ el signo no se puede determinar, pero la combinación de datos sigue siendo importante para reducir las soluciones que más interfieren con la medida de θ_{13} y δ.

En cuanto a la degeneración debida al octante de θ_{23}, la Neutrino Factory a 2810 km combinada con un Superbeam es capaz de resolverla hasta $\theta_{13} > 2°$. Por otro lado, en el régimen solar, hasta $\theta_{13} > 0.6°$ la combinación es capaz de resolverla en muchos casos, pero no en todos. En general el comportamiento de las soluciones es similar al caso de las soluciones falsas de $\mathrm{sign}(\Delta m^2_{23})$, aunque con el problema añadido de que la solución falsa está más lejos de cumplir $\sin\delta' = \sin\delta$, lo que es potencialmente más dañino para medir la violación de CP.

Otros experimentos

Beta Beam

Una posible fuente de neutrinos son los núcleos de átomos inestables que sufren desintegración β. El β-beam surgió con la idea de acelerar hasta cierta energía de referencia un haz de iones pesados que sean β-inestables, dejándolos desintegrarse luego en un anillo de almacenamiento con secciones rectas apuntando hacia el detector. Así se produce un haz de neutrinos puro, con sólo una especie de neutrino, a diferencia de un haz convencional donde conocer el espectro de las diferentes especies supone un cierto error sistemático, y similar al caso de una Neutrino Factory pero sin necesitar un detector capaz de discriminar la carga del leptón producido.

Los iones que se han identificado como candidatos ideales son el ^{6}He para producir un haz de $\bar{\nu}_e$ y el ^{18}Ne para producir uno de ν_e. El CERN es un buen candidato para este tipo de experimento, pues los iones se podrán producir en grandes cantidades gracias a la nueva instalación de EURISOL, ser posteriormente acelerados en el SPS y finalmente transportados a un anillo de almacenamiento donde se desintegrarían produciendo el haz de neutrinos.

En la sección sobre el β-beam se discuten seis escenarios distintos, tres con distintas energías del haz manteniendo la distancia al detector a E/L fijo en el máximo de la oscilación, y otros tres variando la distancia manteniendo fija la energía al máximo alcanzable en el SPS.

En general, un β-beam con energías tan altas como las máximas alcanzables en el SPS es el mejor candidato ($\gamma_{^6\mathrm{He}} = 150$, $L = 300$ km), teniendo aún mejores resultados si se utiliza una versión mejorada del SPS que permita alcanzar una mayor energía (hasta $\gamma_{^6\mathrm{He}} = 350$, con $L = 730$ km). La razón principal es el aumento del número de sucesos y la capacidad de utilizar información espectral, que permite resolver la degeneración intrínseca.

Para las ambigüedades discretas del signo de Δm^2_{23} y del octante de θ_{23}, las opciones de γ alto son también las mejores opciones, ya que existe una región donde son capaces de resolverlas.

Electron Capture Beam

Otro tipo de haz de neutrinos, que comparte muchas propiedades con el β-beam, es el Electron Capture Beam. En lugar de acelerar iones que sufren desintegración β, en el EC-beam se utilizan átomos pesados no completamente ionizados, que sean capaces de realizar la captura electrónica $e^- \, p \to n \, \nu_e$. En este proceso tan sólo hay dos partículas en el estado final, y por tanto la energía del neutrino está fija: se produce así un haz de neutrinos "monocromático" (monoenergético). El concepto es operacional gracias al reciente descubrimiento de nucleos muy lejanos de la línea de estabilidad, que poseen transiciones spin-isospin superpermitidas. Un candidato ideal es el ^{150}Dy.

En un EC-beam la energía de los neutrinos viene dictada por la elección del ión y el boost con el que se acelera. Se pueden seleccionar distintas energías discretas a las que trabajar para explotar la dependencia de las oscilaciones de neutrinos con la energía.

En el apartado donde se discute el EC-beam se consideran dos escenarios. El primero es de más baja energía, con 5 años corriendo a $\gamma = 90$ y otros 5 a $\gamma = 195$ (el máximo alcanzable en el SPS), con una distancia al detector $L = 130$ km (CERN-Fréjus). El segundo corresponde a 5 años con $\gamma = 195$ y otros 5 a $\gamma = 440$ (el máximo alcanzable en un SPS mejorado), con $L = 650$ km (CERN-Canfranc). En ambos casos se utiliza un detector Cerenkov de agua, ya que al tener una sola especie de neutrino no es necesario reconstruir la carga del muón producido. En el régimen de energías utilizado la mayoría de las interacciones son cuasi-elásticas, con lo que se puede reconstruír la energía. Puesto que sólo hay una energía presente en el haz, la reconstrucción no se usa para sacar información espectral, sino para descartar la inmensa mayoría de sucesos de background, ya que estos tienen una energía reconstruída mucho más baja que la de la señal.

Ambos escenarios presentan, a falta de un estudio detallado de sistemáticos, correlaciones y degeneraciones, unos resultados espectaculares, siendo el segundo el más prometedor en cuanto a sensibilidad, con una capacidad para la medida de θ_{13} y δ que se insinúa comparable con la Neutrino Factory.

Conclusiones

El descubrimiento de las oscilaciones de neutrinos ha mostrado que estas partículas poseen masa, muy difícil de ver de otra forma debido a lo pequeña que es. Más aún, ha mostrado que existe una mezcla entre los autoestados de sabor y masa en el sector leptónico, similar al que ocurre con los quarks y descrito por la matriz CKM. Todo ello ha expandido el Modelo Estándar mínimo para acomodar 7 nuevos parámetros fundamentales: las masas de los tres sabores de neutrinos, tres ángulos de mezcla y una fase de violación CP. Experimentos pasados han sido capaces de medir con cierta precisión las dos diferencias de masa al cuadrado (Δm^2_{12} y Δm^2_{23}) y dos ángulos de mezcla (θ_{12} y θ_{23}), y de encontrar un límite superior al ángulo de mezcla restante (θ_{13}). Sin embargo, todavía no existe una medida directa de $\theta_{13} > 0$ y del valor de la fase δ, y si se tuviera $\delta \neq 0°, 180°$ implicaría la existencia de violación CP en el sector leptónico. Finalmente, quedan por resolver un par de incógnitas entre los parámetros de oscilación: la jerarquía de masa (el signo de Δm^2_{23}) y el octante de θ_{23}.

La generación presente y la próxima de experimentos de neutrinos de base larga se encuentran bien posicionados para encontrar estos parámetros fundamentales todavía desconocidos, así como medir con mejor precisión los que ya se conocen. Existen propuestas excitantes con capacidad para explorar una región amplia del espacio de parámetros, tales como la Neutrino Factory, Superbeams, β-beams y EC-beams. Cada una presenta sus propios méritos y limitaciones.

Tanto los Superbeams como la Neutrino Factory están afectados en su sensibilidad última por la incertidumbre en la sección eficaz de producción hadrónica. En particular, la medida de la sección eficaz del proceso $p + \text{blanco} \rightarrow \pi^{\pm}, K$ proporcionada por HARP será un componente esencial para experimentos actuales como K2K y MiniBooNe, así como para futuros experimentos de base larga con neutrinos provenientes de aceleradores y también los de neutrinos atmosféricos.

Una Neutrino Factory donde los neutrinos son producidos por la desintegración de muones guardados en un anillo de almacenamiento, con energías del muón de unas pocas decenas de GeV, sigue proporcionando la mayor sensitividad a través de la búsqueda de muones "de signo equivocado". Cuando empiece a funcionar un experimento de este tipo, tanto el valor de δ como el de θ_{13} pueden permanecer todavía desconocidos, y entonces deberán ser medidos simultaneamente.

En la determinación de los parámetros desconocidos hay dos efectos que estropean la medida: las correlaciones y las degeneraciones. Para un par de valores de (θ_{13}, δ) la reconstrucción de la verdadera solución viene en general acompañada por otras falsas, que pueden interferir severamente con la medida de violación CP. Una de las soluciones falsas viene de la correlación intrínseca entre δ y $\theta_{!3}$, y las otras vienen de las ambigüedades discretas en $\text{sign}(\Delta m^2_{23})$ y el octante de θ_{23}.

Hay un potencial enorme para resolver estas degeneraciones combinando datos de un Superbeam y una Neutrino Factory. Debido a la importancia de los efectos de materia, las distancias entre fuente y detector que son óptimas para medir violación CP en una Neutrino Factory se encuentran a un L/E bastante menor que el propuesto en los Superbeams. Una Neutrino factory con una base $L = 2810$ km junto a un Superbeam sería capaz de resolver todas las degeneraciones y proveer una medida limpia de θ_{13} y de δ hasta valores de $\theta_{13} \gtrsim 1^\circ$. Incluso para valores de $\theta_{13} > 0.5^\circ$ sólo la ambigüedad asociada con el octante de θ_{23} sería un problema, si θ_{23} fuera lejano a su valor máximo permitido.

Los β-beams y EC-beams pueden proporcionar una sensitividad de un orden similar, pero para poder hacer una comparación justa con los Superbeams y la Neutrino Factory se requiere un estudio completo de cómo son afectados por las incertidumbres sistemáticas y las degeneraciones.

Los Superbeams y la Neutrino Factory son dos pasos sucesivos en el camino hacia el descubrimiento de la violación CP en el sector leptónico, con una perspectiva sólida ofrecida por la combinación de sus resultados.

Chapter 1
Introduction

1.1 Overview

Neutrino physics has provided the first evidence of physics beyond the Standard Model. During the last 35 years a series of neutrino experiments have been carried out with results that didn't fit the commonly accepted picture. Today most of those puzzles are explained thanks to the existence of neutrino oscillations.

A neutrino of a given flavor (ν_e, ν_μ or ν_τ) can transform into a neutrino of a different flavor, and the pattern of this transformation repeats itself in time, that is, the neutrino "oscillates". For these oscillations to happen neutrinos must have mass. Also, eigenstates of the weak interaction must be rotated with respect to the mass eigenstates, which can be described with a mixing matrix similar to the CKM-matrix in the quark sector. This mixing matrix introduces 4 new fundamental parameters: 3 mixing angles and a complex phase. The exciting possibility of leptonic CP violation is thus accessible.

We have now fully entered an era of precision measurements of the parameters that govern these oscillations.

1.2 Historical Context

1.2.1 Discovery of the Neutrino

The neutrino appears for the first time in 1930, as an hypothesis formulated by Wolfgang Pauli [Pau77] to explain why electrons coming from β-decay don't have a fixed energy. In radioactive β decays, a nucleus mutates because a neutron is transformed into a proton, which is slightly lighter, and also emits an electron and a neutrino, $n \rightarrow p\, e^- \,\bar{\nu}_e$.

Without the neutrino, energy conservation requires that the electron and proton share the energy of the neutron in a fixed amount, giving a monochromatic electron peak. This is not what was observed. Experiments indicated conclusively that the electrons were not mono-energetic, but could take a range of energies (see figure 1.1). This energy range corresponded exactly to the different ways the three particles in the final state of a three-body decay can share energy satisfying conservation of energy and momentum, if the third particle was very light. Pauli required his hypothetical particle to be neutral and have spin 1/2, to ensure conservation of electric charge and angular momentum respectively.

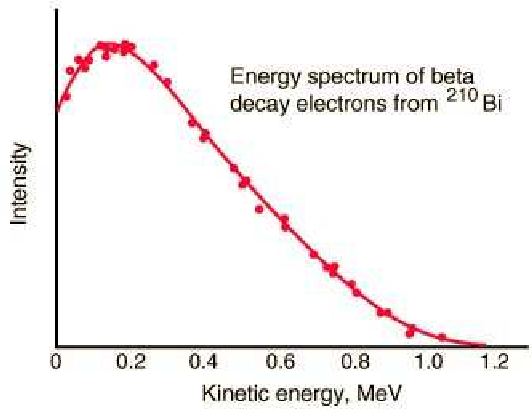

Figure 1.1. The wide energy spectrum of the outgoing electron in the beta decay $n \rightarrow p\, e^-\ \bar{\nu}_e$ is in contradiction with the mono-energetic electron expected from a two body decay, and thus points to the existence of a third particle, which we know today to be the *electron antineutrino*, $\bar{\nu}_e$.

Learning of Pauli's idea, Fermi proposed in 1934 his theory of β decay, based on which Bethe & Peierls predicted in the same year the cross section for the interaction of the neutrino with matter to be extremely small.

In 1956, Cowan and Reines discovered the electron antineutrino through the reaction $\bar{\nu}_e\, p \rightarrow e^+\, n$ using an experimental setup that they had proposed themselves three years earlier [RC53]. For this discovery they got the Nobel Prize 39 years later.

That same year Pontecorvo, influenced by the recent study of Gell-Mann and Pais about the existence of neutral kaons, considered the possibility of a quantum mixture in the neutrino. In his work [Pon57] he proposed that an antineutrino produced in a nuclear reactor could oscillate into a neutrino and that this one could be detected. That is how the theory of neutrino oscillation was born.

In 1962 Danby et al. observed the existence of different types of neutrinos, and the same year Maki, Nakagawa and Sakata introduced a key concept in the theory of oscillations: two different types of neutrinos can only oscillate from one to another if they have different masses [MNS62].

1.2.2 The Solar Neutrino Problem

Solar neutrinos are electron neutrinos produced in the thermonuclear reactions that take place in the Sun. These reactions occur via two main chains, the proton-proton chain ("PP chain") and the CNO cycle, shown in fig. 1.2. The proton-proton chain is more important in stars the size of the Sun or less. There are five reactions which produce ν_e in the proton-proton chain, and three in the CNO cycle. Both chains result in the overall fusion of protons into ^{4}He:

$$4p \rightarrow {}^4\mathrm{He} + 2e^+ + 2\nu_e + \gamma \tag{1.1}$$

where the energy released in the reaction, $Q = 4m_p - m_{^4He} - 2m_e \simeq 26$ MeV, is mostly radiated through the photons, and only a small fraction is carried by the neutrinos, $\langle E_{2\nu_e}\rangle = 0.59$ MeV.

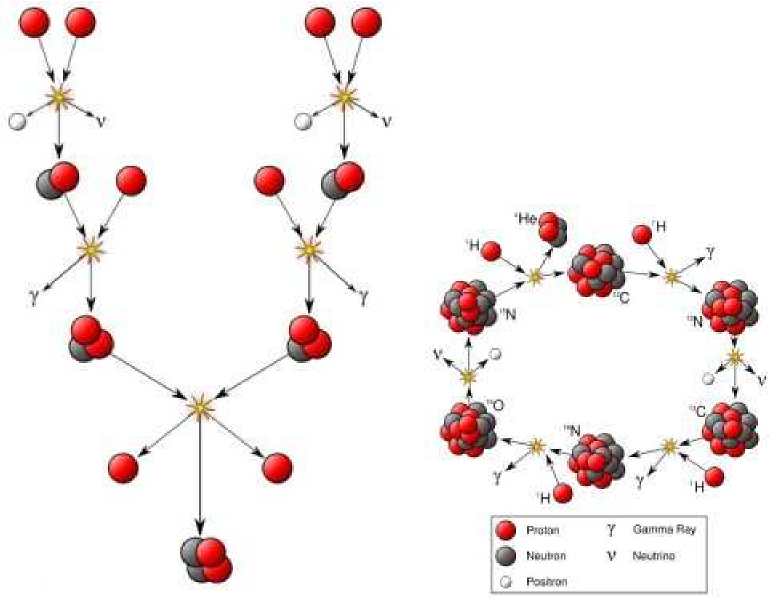

Figure 1.2. Left: The proton-proton chain, Sun's main source of energy, produces electron neutrinos. Right: CNO cycle in the Sun, which also produces electron neutrinos.

Solar Models [BKS98] describe the properties of the Sun and its evolution after entering the main sequence. The models are based on a set of observational parameters: surface luminosity, age, radius and mass, and on several basic assumptions: spherical symmetry, hydrostatic and thermal equilibrium, equation of state of an ideal gas and present surface abundances of elements similar to the primordial composition. With such models it is possible to predict the neutrino fluxes from the Sun, as well as their energy spectrum.

Raymond Davis Jr., John Bahcall and Don Harmer proposed in 1964 an experiment to search for solar neutrinos from ^8B using a tank full of chlorine. Soon after, Davis started his historical experiment at the Homestake mine (South Dakota, USA) [DHH68].

Four years later, Davis and his collaborators informed of a deficit in the flux of solar neutrinos when the obtained data were compared with the predictions of the Standard Solar Model (SSM) defined by Bahcall *et al.* [BKS98].

The disagreement was called the "solar neutrino anomaly", the "solar neutrino problem" and even the "mystery of the missing neutrinos"; it was thought that something was wrong either with the experiment or the SSM. However, Gribov and Pontecorvo interpreted this deficit as a clear evidence of neutrino oscillation.

Over the next twenty years many different possibilities were examined, but both the SSM and the experiment appeared to be correct. The solar models have been steadily refined as the result of increased observational and experimental information about the input parameters (such as nuclear reaction rates and the surface abundances of different elements), more accurate calculations of constituent quantities (such as radiative opacity and equation of state), the inclusion of new physical effects (such as element diffusion) and the development of faster computers and more precise stellar evolution codes.

Davis' experiment has been operating since, and five other experiments have joined in, GALLEX (in Gran Sasso, Italy) [GALLEX99], SAGE (Baksan, Rusia) [SAGE99], Kamiokande and Super-Kamiokande (Kamioka, Japan) [Super-Kamiokande99] and more recently Sudbury Neutrino Observatory (SNO) (Sudbury, Canada) [SNO01]. Each experiment is different from each other in that it observes a specific part of the solar neutrino spectrum (fig. 1.3). All of them have found fewer ν_e than predicted by the Standard Solar Model (fig. 1.4).

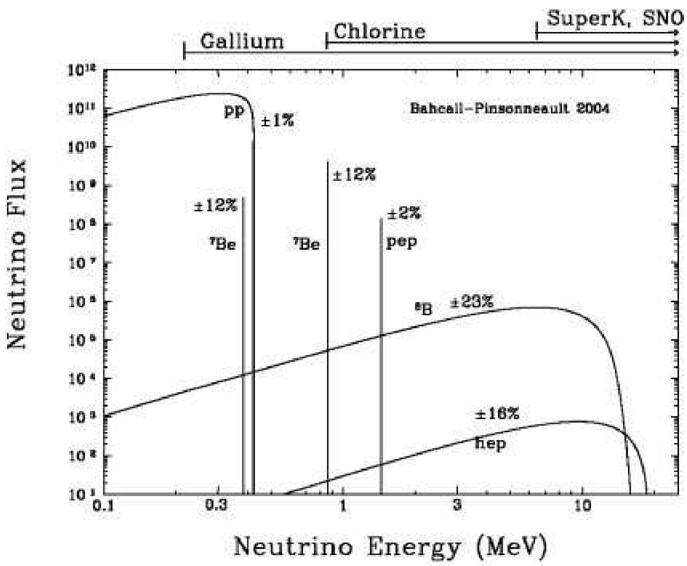

Figure 1.3. Sensitivities of the different kind of solar neutrino experiments to the energy of the electron neutrinos produced in different reactions in the Sun.

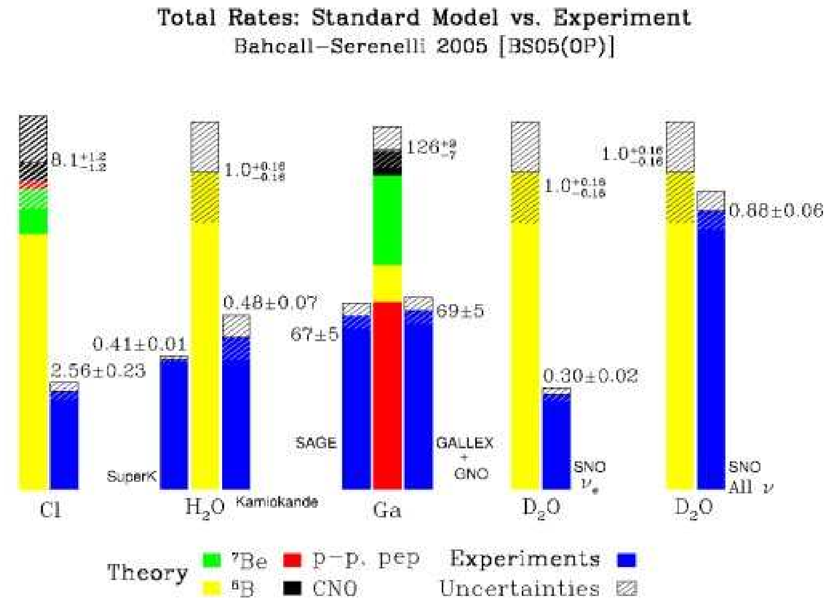

Figure 1.4. Predictions of the Standard Solar Model with the total observed rates in the six solar neutrino experiments: Davis' chlorine, Super-Kamiokande, Kamiokande, GALLEX, SAGE, and SNO. The model predictions are color coded with different colors for the different predicted neutrino components. For both the experimental values and the predictions, the 1σ uncertainties are indicated by cross hatching.

Before the neutral current measurements at SNO all experiments observed a flux that was smaller than the SSM predictions, $\Phi^{obs}/\Phi^{SSM} \sim 0.3 - 0.6$. Also, the deficit is not the same for the various experiments, which may indicate that the effect is energy dependent. Those are the results that constitute what is called the "Solar Neutrino Problem".

1.2.3 The Atmospheric Neutrino Problem

Atmospheric neutrinos are the neutrinos produced in cascades initiated by collisions of cosmic rays with the Earth's atmosphere (see fig. 1.5). Some of the mesons produced in these cascades, mostly pions and some kaons, decay into electron and muon neutrinos and antineutrinos:

$$
\begin{aligned}
\pi^{\pm} &\rightarrow \mu^{\pm}\,\nu_{\mu}\,(\bar{\nu}_{\mu}) \\
\mu^{\pm} &\rightarrow e^{\pm}\,\nu_{e}\,\bar{\nu}_{\mu}\,(\bar{\nu}_{e}\,\nu_{\mu})
\end{aligned}
$$

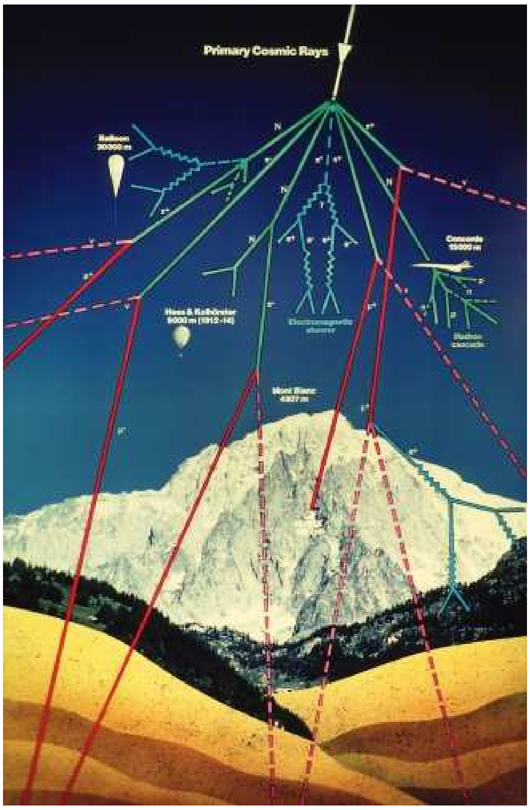

Figure 1.5. A high-energy particle coming from space, a cosmic ray, interacts with an atom in the Earth's atmosphere and develops a cascade of particles. Some of the final particles are neutrinos.

The expected flux of atmospheric neutrinos depends on three main factors: the spectrum and composition of the cosmic rays, Earth's geomagnetic field and the neutrino production cross-sections in the hadronic interactions that take place in the atmosphere. The fluxes are uncertain at the 20% level, but the ratios of neutrinos of different flavor are expected to be accurate to better than 5%. That's why the experiments with atmospheric neutrinos typically present their results as a double quotient of the experimental values and the Monte Carlo predictions:

$$R = \left(\frac{N_\mu}{N_e}\right)_{exp} \Big/ \left(\frac{N_\mu}{N_e}\right)_{MC} \tag{1.2}$$

Atmospheric neutrinos were first detected in the 1960's by the underground experiments in South Africa and the Kolar Gold Field experiment in India. These experiments measured the flux of horizontal muons (they could not discriminate between downgoing and upgoing directions) and although the observed total rate was not in full agreement with theoretical predictions, the effect was not statistically significant.

In the 1970s, with the appearance of the Grand Unification Theories (GUTs) and of the symmetries between leptons and quarks, it was suggested that the proton might be unstable. This originated the development of several underground detectors (to minimize the contamination originated by the products of the cosmic rays) big enough to contain enough protons and to detect the Cerenkov radiation emitted by the products of the proton decay. Two different detection techniques were employed. In water Cerenkov detectors the target is a large volume of water surrounded by photomultipliers which detect the Cerenkov ring produced by the charged leptons (see fig. 1.6). The event is classified as an electron-like or muon-like if the ring is respectively diffuse or sharp. In iron calorimeters, the detector is composed of a set of alternating layers of iron which act as target and some tracking elements, such as plastic drift tubes, which allow the reconstruction of the shower produced by the electrons or the tracks produced by muons. Both types of detectors allow for flavor classification of the events.

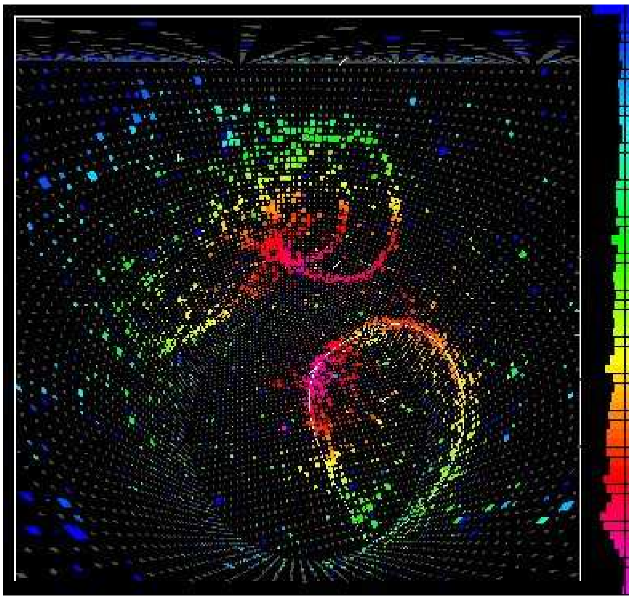

Figure 1.6. Cerenkov rings produced by neutrino interactions in water.

The two oldest iron calorimeter experiments, Fréjus and NUSEX, found atmospheric neutrino fluxes in agreement with the theoretical predictions. On the other hand, two water Cerenkov detectors, IMB and Kamiokande, detected a ratio of ν_μ-induced events to ν_e-induced events smaller than the expected one by a factor of about 0.6. This was the original formulation of the atmospheric neutrino anomaly, or the "atmospheric neutrino problem".

Whether the ratio $R_{\mu/e}/R^{\rm MC}_{\mu/e}$ is small because there is ν_μ disappearance or ν_e appearance or a combination of both could not be determined. Furthermore, the fact that the anomaly appeared only in water Cerenkov and not in iron calorimeters could point to a systematic problem as the origin of the effect.

Kamiokande also presented the zenith angular dependence of the deficit for the multi-GeV neutrinos. The results seemed to indicate that the deficit was mainly due to the neutrinos coming from below the horizon. Atmospheric neutrinos are produced isotropically at a distance of about 15 km above the surface of the Earth. Therefore neutrinos coming from the top of the detector have traveled approximately those 15 km before interacting while those coming from the bottom of the detector have traversed the full diameter of the Earth, $\simeq 10^4$ km, before reaching the detector. The Kamiokande distribution suggested that the deficit increases with the distance between the neutrino production and interaction points.

The results of Kamiokande were later strongly confirmed by its successor, Super-Kamiokande. The data from Super-Kamiokande show that the angular and energy dependence of the ν_e spectrum corresponds to the expected one (with no oscillations). On the other hand, the ν_μ spectrum showed a strong dependency in the azimuthal angle. This is a clear evidence of ν_μ disappearance due to their oscillation to other neutrino flavor not detected.

1.3 Theoretical Framework

1.3.1 Neutrino Flavors

In the Standard Model, the strong, weak and electromagnetic interactions are related to, respectively, the $SU(3)$, $SU(2)$ and $U(1)$ gauge groups. Many features of the various interactions are then explained by the symmetry to which they are related. In particular, the way that the various fermions are affected by the different types of interactions is determined by their representations under the corresponding symmetry groups.

Neutrinos are fermions that have neither strong nor electromagnetic interactions. In group theory language, they are singlets of $SU(3)_C \times U(1)_{EM}$.

The Standard Model has three neutrinos. They reside in lepton doublets:

$$L_\ell = \begin{pmatrix} \nu_{L\ell} \\ \ell_L^- \end{pmatrix}, \qquad \ell = e, \mu, \tau. \tag{1.3}$$

where e, μ and τ are the charged lepton mass eigenstates. The three neutrino interaction eigenstates, the electron (ν_e), muon (ν_μ) and tau (ν_τ) neutrino, are defined as the states that form the charged currents with their lepton partners, that is, they are the $SU(2)_L$ partners of the charged lepton mass eigenstates (see eq. (1.4)).

The states ν_e, ν_μ and ν_τ are called flavor states, in contrast with the quarks, where flavors are identified with states with a definite mass.

The Lagrangian of the interaction of neutrinos with other particles is given by the Charged Current (CC) and the Neutral Current (NC) Lagrangians:

$$\begin{aligned} \mathcal{L}_I^{CC} &= -\frac{g}{2\sqrt{2}} j_\alpha^{CC} W^\alpha + h.c. \\ \mathcal{L}_I^{NC} &= -\frac{g}{\cos\theta_W} j_\alpha^{NC} Z^\alpha \end{aligned} \tag{1.4}$$

where g is the electroweak interaction constant, θ_W is the weak angle, W^α and Z^α are the vectorial bosonic fields $W^\pm$ and Z^0, and j_α^{CC}, j_α^{NC} are the charged and neutral currents of the leptons respectively:

$$\begin{aligned} j_\alpha^{CC} &= \sum_{\ell=e,\mu,\tau} \bar{\nu}_\ell \gamma_\alpha (1-\gamma_5) \ell \\ j_\alpha^{NC} &= \sum_{\ell=e,\mu,\tau} \bar{\nu}_\ell \gamma_\alpha (1-\gamma_5) \nu_\ell \end{aligned} \tag{1.5}$$

1.3.1.1 Why Three?

The three flavors of neutrinos seem to be intimately related to the three flavors of leptons and quarks. Nature seems to repeat itself three times with different masses. The reason is not known, but might be a consequence of a symmetry of a higher theory.

There might be other types of neutrinos, but either they don't have any interaction at all (*sterile neutrinos*) or they are very massive. We know that because the number of light (that is, $m_\nu \lesssim m_Z/2$) neutrino flavors have been measured by LEP based on a fit to the Z invisible width. The $Z \to \nu\,\bar{\nu}$ channel contributes to the invisible width of the Z decay: $\Gamma_{\rm inv} = \Gamma_{\rm tot} - \Gamma_l - \Gamma_h$, where $\Gamma_{\rm tot}$, Γ_l, Γ_h are the total, leptonic (charged) and hadronic widths respectively. The effective number of neutrino species is defined as $N_\nu = \Gamma_{\rm inv}/\Gamma_\nu$, where Γ_ν is the width due to the decay to a neutrino in the Standard Model. The fit (fig. 1.7) gives $N_\nu = 2.987 \pm 0.012$, consistent with the expected 3.

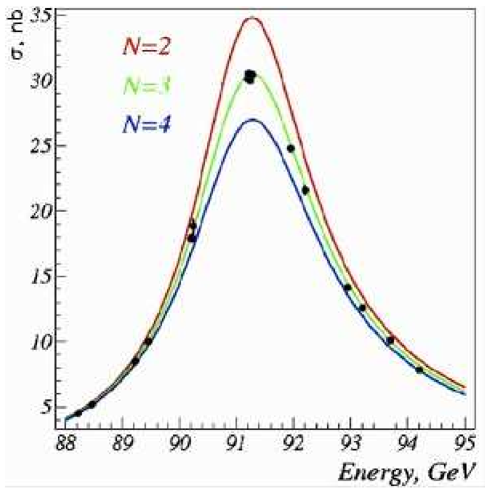

Figure 1.7. ALEPH 1993: Hadronic cross section as function of c.m. energy. Expectations for 2, 3 and 4 neutrinos are superimposed.

1.3.2 Dirac and Majorana

It was Dirac's equation that first led to the concept of particles and antiparticles, the positive electron being the earliest candidate for an antiparticle. While positive electrons are clearly distinct from negative electrons by their electromagnetic properties, it is not obvious in what way neutral particles should differ from their antiparticles. The neutral pion, for example, was found to be identical to its antiparticle. The neutral kaon, on the other hand, is clearly different from its antiparticle. However, the pion and kaon, both bosons, are not elementary particles, as they are composed of two charged fermions, the quarks and the antiquarks.

The concept of a particle that is identical to its antiparticle was formally introduced by Majorana in 1937. Thus, such particles are normally referred as Majorana particles. In contrast, those which are not, are called Dirac particles.

1.3.3 Neutrino Mass

There was never any good reason for neutrinos not to have mass, because there is not an exact gauge symmetry that forbids them to have it. For photons and gluons, it is the exact symmetries $U(1)$ and $SU(3)$ of the Standard Model that make them have null mass. There is not a gauge boson of null mass corresponding to the leptonic number, and so it was expected to find a non-zero mass for neutrinos.

There are many models of neutrino mass based on GUTs, flavor theories with an additional symmetry $U(1)$ of generation, and recently extra-dimension models. In that sense, neutrino masses allow to foresee physics at a higher scale, possibly further away from the capacity of the experiments with colliders, providing us with an insight at GUTs, flavor physics, and maybe even quantum gravity.

The electroweak Standard Model has only a left neutrino for each generation. That is why the neutrino in this model cannot have a Dirac mass term, as this requires the two helicity states for each particle. However, there is an alternative mass term, called the Majorana mass term, that does not have this problem. This term requires a single state of helicity for the particle and the opposite helicity state for the antiparticle. But it violates the total lepton number in two units and the Standard Model preserves the leptonic number for each generation. Because of that, none of the possible mass terms can appear to any order in a perturbative theory or in presence of non-perturbative effects. As a consequence, in this context there is no neutrino mass, nor neutrino magnetic moment. Detection of neutrino masses is a sign of physics beyond the Standard Model.

1.3.4 Mixing

The main idea in the theory of neutrino oscillations is the fact that neutrinos produced in weak interactions, which are weak interaction eigenstates, are not eigenstates of the mass matrix, which determines how the quantum state of a neutrino evolves in time. Similarly, in the detection process, the neutrino is a weak eigenstate. So, when a neutrino of a given flavor is produced with a definite momentum the different mass states will propagate through space at different velocities. After a while the mass eigenstates will become out of phase with each other, so that the mixture they form will change with time. Hence, what started as a pure neutrino becomes a time-varying superposition of all three neutrinos.

1.3.4.1 2-Family Mixing

To illustrate the dynamics of neutrino oscillation, let's consider a 2-flavor neutrino mixing. The flavor eigenstates, ν_e and ν_μ, which are orthogonal, can be written as a linear combination of the mass eigenstates (also orthogonal), ν_1 and ν_2:

$$\begin{pmatrix} \nu_e \\ \nu_\mu \end{pmatrix} = \begin{pmatrix} \cos\theta & \sin\theta \\ -\sin\theta & \cos\theta \end{pmatrix} \begin{pmatrix} \nu_1 \\ \nu_2 \end{pmatrix} \tag{1.6}$$

that is, using the notation $|\nu\rangle$ to represent the state vector of the neutrino,

$$\begin{aligned} |\nu_e\rangle &= \cos\theta\,|\nu_1\rangle + \sin\theta\,|\nu_2\rangle \\ |\nu_\mu\rangle &= -\sin\theta\,|\nu_1\rangle + \cos\theta\,|\nu_2\rangle \end{aligned} \tag{1.7}$$

The mass eigenstates evolve in a very simple way in time, because they are eigenstates of the Hamiltonian:

$$
\begin{aligned}
|\nu_1(t)\rangle &= e^{-iE_1 t}|\nu_1\rangle = e^{-i\sqrt{m_1^2+p^2}\,t}|\nu_1\rangle \\
&\simeq e^{-i(p+\frac{m_1^2}{2p})t}|\nu_1\rangle \\
|\nu_2(t)\rangle &\simeq e^{-i(p+\frac{m_2^2}{2p})t}|\nu_2\rangle
\end{aligned}
\tag{1.8}
$$

the approximation being valid for $p \gg m$.

If at $t=0$ a ν_e is created, its state vector will be $|\Psi(0)\rangle = |\nu_e\rangle$, and

$$
\begin{aligned}
|\Psi(t)\rangle &= c\,|\nu_1(t)\rangle + s\,|\nu_2(t)\rangle \\
&\simeq e^{-ip}\left(c\,e^{-i\frac{m_1^2}{2p}t}\,|\nu_1\rangle + s\,e^{-i\frac{m_2^2}{2p}t}\,|\nu_2\rangle\right)
\end{aligned}
\tag{1.9}
$$

where $c \equiv \cos\theta$ and $s \equiv \sin\theta$ to simplify the notation.

The probability that the original $|\nu_e\rangle$, now $|\Psi(t)\rangle$, has oscillated to a $|\nu_\mu\rangle$ after a time t is

$$
\begin{aligned}
P_{\nu_e \rightsquigarrow \nu_\mu}(t) &= |\langle\nu_\mu|\Psi(t)\rangle|^2 \\
&\simeq \left|(-s\,\langle\nu_1| + c\,\langle\nu_2|)\left(ce^{-i\frac{m_1^2}{2p}t}|\nu_1\rangle + se^{-i\frac{m_2^2}{2p}t}|\nu_2\rangle\right)\right|^2 \\
&= \left|-s\,ce^{-i\frac{m_1^2}{2p}t} + c\,se^{-i\frac{m_2^2}{2p}t}\right|^2 \\
&= 2\,s^2\,c^2\left(1-\cos\left(\frac{m_2^2-m_1^2}{2p}t\right)\right) \\
&= \sin^2(2\,\theta)\,\sin^2\!\left(\frac{\Delta m^2}{4\,p}\,t\right) \\
&\simeq \sin^2(2\,\theta)\,\sin^2\!\left(\frac{\Delta m^2}{4\,E}\,L\right)
\end{aligned}
\tag{1.10}
$$

where $\Delta m^2 \equiv m_2^2 - m_1^2$ and we have used $\cos^2(x)\sin^2(x) = \frac{1}{4}\sin^2(2\,x)$, $1-\cos(2\,x) = 2\sin^2 x$ and, in natural units, $p \simeq E$, $t \simeq L$, where L is the distance that the neutrino has traveled before its detection.

The oscillation probability is a periodic function of the distance. As can be seen in eq. (1.10), the maximum oscillation happens for $\theta = \pi/4$, that is, maximum mixing between flavor and mass eigenstates, and the period of the oscillation is $2\,\pi\,\frac{2\,E}{\Delta m^2}$.

1.3.4.2 3-Family Mixing

The current atmospheric and solar neutrino data can be easily accommodated in a three-family mixing scenario. If we write the weak eigenstates as a function of the mass eigenstates (see fig. 1.8) we get the leptonic equivalent of the Cabibbo-Kobayashi-Maskawa matrix, the Pontecorvo-Maki-Nakagawa-Sakata (PMNS) matrix:

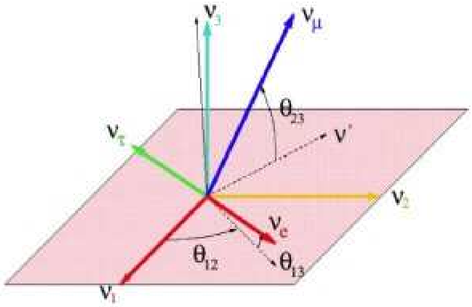

Figure 1.8. Mixing of the three flavor eigenstates with the three mass eigenstates.

$$\begin{pmatrix} \nu_e \\ \nu_\mu \\ \nu_\tau \end{pmatrix} = U \begin{pmatrix} \nu_1 \\ \nu_2 \\ \nu_3 \end{pmatrix}$$

$$\begin{aligned} U &\equiv U_{23}\,U_{13}\,U_{12} \\ &\equiv \begin{pmatrix} 1 & 0 & 0 \\ 0 & c_{23} & s_{23} \\ 0 & -s_{23} & c_{23} \end{pmatrix} \begin{pmatrix} c_{13} & 0 & s_{13}\,e^{i\delta} \\ 0 & 1 & 0 \\ -s_{13}\,e^{-i\delta} & 0 & c_{13} \end{pmatrix} \begin{pmatrix} c_{12} & s_{12} & 0 \\ -s_{12} & c_{12} & 0 \\ 0 & 0 & 1 \end{pmatrix} \end{aligned} \tag{1.11}$$

with $c_{ij} \equiv \cos\theta_{ij}$ and $s_{ij} \equiv \sin\theta_{ij}$. There are three mixing angles θ_{ij} and one phase δ, that, if different from zero, would be responsible for CP violation.

This decomposition parametrizes the 3D rotation matrix as the product of three independent rotations, one in the plane 23 (which will be responsible for the atmospheric transitions), another in the plane 12 (solar transitions) and a third one that connects both.

Without loss of generality we can choose the convention in which all Euler angles lie in the first quadrant, $0 \leq \theta_{ij} \leq \pi/2$, while the phase is unrestricted, $0 \leq \delta < 2\pi$.

With the currently known $\Delta m^2_{12} \ll \Delta m^2_{23}$ and $\sin^2 2\theta_{13} \ll 1$, it is possible to derive approximate expressions that can help to understand the behavior of the probability. They will be presented in the next chapters. The main remark here is that the oscillation probabilities in three neutrino families are described by two mass differences (Δm^2_{12} and Δm^2_{23}) and 4 parameters from the PMNS matrix: three mixing angles (θ_{12}, θ_{23}, θ_{13}) and a phase (δ). The presence of this phase in the mixing matrix makes it possible to study CP violation, and is commonly called the *CP-violating phase*.

1.3.5 Matter Effects

Interactions modify the effective mass that a particle exhibits while traveling through a medium. A well-known example is that of the photon, which is massless in the vacuum but develops an effective mass in a medium. As a result, electromagnetic waves do not travel with speed c through a medium. The effective masses of neutrinos are similarly modified in a medium by their interactions.

Wolfenstein pointed out that the patterns of neutrino oscillation might be significantly affected if the neutrinos travel through a material medium rather than through the vacuum. Normal matter contains electrons but no muons or taus at all. Thus, if a ν_e beam goes through matter, it suffers both charged and neutral current interactions with the electrons. However, ν_μ or ν_τ interact with an electron only via the neutral current, so their interactions are different in magnitude to that of the ν_e. This way, the modulation of the ν_e component is different from the same modulation inside the vacuum. This leads to changes in the oscillation probabilities.

We show an example in a simplified case with only ν_e and ν_μ, and assume that the density of the background matter is uniform, with n_e, n_p and n_n denoting the number of electrons, protons and neutrons per unit volume. Elastic scattering of these particles change the effective masses of the neutrinos.

Elastic scattering through charged current interactions can only happen between ν_e and e. The effective lagrangian for such an interaction is:

$$\frac{4\,G_F}{\sqrt{2}}\left(\bar{e}\,(p_1)\,\gamma_\lambda\,P_L\,\nu_e(p_2)\right)\left(\nu_e(p_3)\,\gamma^\lambda\,P_L\,e(p_4)\right)$$
$$\frac{4\,G_F}{\sqrt{2}}\left(\bar{\nu}_e(p_3)\,\gamma_\lambda\,P_L\,\nu_e(p_2)\right)\left(\bar{e}\,(p_1)\,\gamma^\lambda\,P_L\,e(p_4)\right)$$

where the second form is obtained via a Fierz transformation. For forward scattering where $p_2 = p_3 = p$, this gives the following contribution that affects the propagation of the ν_e:

$$\sqrt{2}\,G_F\bar{\nu}_{eL}(p)\,\gamma_\lambda\,\nu_{eL}(p)\,\langle\bar{e}\,\gamma^\lambda\,(1-\gamma_5)\,e\rangle \tag{1.12}$$

averaging the electron field bilinear over the background. It is possible to calculate that average, using that the axial current reduces to spin in the non-relativistic approximation, which is negligible for a non-relativistic collection of electrons. The spatial components of the vector current give the average velocity, which is negligible as well. So the only non-trivial average is

$$\langle\bar{e}\,\gamma^0\,e\rangle = \langle e^\dagger e\rangle = n_e \tag{1.13}$$

which gives a contribution to the effective lagrangian

$$\sqrt{2}\,G_F n_e\,\bar{\nu}_{eL}\,\gamma_0\,\nu_{eL} \tag{1.14}$$

This effectively adds an amount $\sqrt{2}\,G_F n_e$ to the energy of the particle.

For neutral currents, we can find in the same way the following contributions to effective energies of both ν_e and ν_μ:

$$\sqrt{2}\,G_F \sum_f n_f \left(I_{3L}^{(f)} - 2\sin^2\theta_W Q^{(f)}\right) \tag{1.15}$$

where f stands for the electron, the proton or the neutron, $Q^{(f)}$ is the charge of f and $I_{3L}^{(f)}$ is the third component of weak isospin of the left-chiral projection of f. Thus, for the proton, $Q = 1$ and $I_{3L} = 1/2$, whereas for the electron, $Q = -1$ and $I_{3L} = -1/2$. Also, for normal neutral matter, $n_e = n_p$, to guarantee charge neutrality. Therefore the contributions of the electron and the proton cancel each other and we are left with the neutron contribution, which is

$$-\sqrt{2}\,G_F n_n/2 \tag{1.16}$$

This neutral current is *the same for all flavors of neutrinos*, while the charged current contribution affects ν_e only. Thus, in the evolution equation of neutrino beams:

$$\frac{d}{dt}\begin{pmatrix} \nu_e \\ \nu_\mu \end{pmatrix} = H'\begin{pmatrix} \nu_e \\ \nu_\mu \end{pmatrix} \tag{1.17}$$

where $H' = UHU^\dagger$, H' is replaced by

$$H'' = H' - \frac{1}{\sqrt{2}} G_F n_n + \begin{pmatrix} \sqrt{2}\,G_F n_e & 0 \\ 0 & 0 \end{pmatrix} \tag{1.18}$$

The effective mixing angle in matter, $\tilde{\theta}$, would accordingly be given by

$$\tan 2\,\tilde{\theta} = \frac{2\,H'_{12}}{H'_{22} - H'_{11}} = \frac{(m_2^2 - m_1^2)\sin 2\,\theta}{(m_2^2 - m_1^2)\cos 2\,\theta - A} \tag{1.19}$$

where $A = 2\sqrt{2}\,G_F n_e E$.

The effective mixing angle thus changes inside matter. The change is most dramatic if $A = (m_2^2 - m_1^2)\cos 2\theta$, that is, if the electron number density is given by:

$$n_e = \frac{(m_2^2 - m_1^2)\cos 2\,\theta}{2\sqrt{2}\,G_F E} \tag{1.20}$$

Then, even if the vacuum mixing angle θ is small, we have $\tilde{\theta} = \pi/4$, which is to say that ν_e and ν_μ mix maximally. This phenomenon is known as *resonance*.

Chapter 2
The Neutrino Factory

2.1 Origin of the Idea

In a Neutrino Factory, neutrinos are produced by the decays of muons circulating in a storage ring. Most of what is known of muon storage rings is due to the pioneering work of the Muon Collider Collaboration [Kos]. They were able to formulate and, to a large extent, simulate the basic concepts of a Muon Collider. The concept of a Neutrino Factory was born from the realization that the beams of neutrinos emitted by the decaying muons along the accelerator chain or in the storage rings could be valuable physics tools [Gee98], the potential of which was emphasized in the ECFA prospective study. The Neutrino Factory design is presently being pursued in the United States, in Europe and in Japan.

2.2 Characteristics

The main advantage of neutrino factories over conventional beams is the purity of the beam. In a conventional beam an intense proton beam hits a target, and the produced hadrons are focused and finally let decay in a long tunnel, thus producing an almost pure ν_μ or $\bar{\nu}_\mu$ beam. However, the small background is what makes oscillation experiments difficult. There is about 1% of ν_e and antineutrinos of both flavors, produced by the three-body decays $K^+ \to e^+ \pi^0 \nu_e$ and $K_L \to e^\pm \pi^\mp \nu_e(\bar{\nu}_e)$, and tertiary muons that decay before they can be absorbed, $\mu^\pm \to e^\pm \nu_e(\bar{\nu}_e) \bar{\nu}_\mu(\nu_\mu)$.

If one is trying to measure large effects this contamination would not be a big problem, but the next step in neutrino oscillation physics will be to look for an effect which has already been determined by experiment to be less than about 5%. Precisely knowing this intrinsic background and subtracting it from a potential signal will be the only way to make the measurement. Also, to most massive detectors, neutral current events, in which there is no final state muon, can fake the ν_e charged current events.

On the other hand, the beam produced by a neutrino factory with, for instance, μ^+ in the storage ring, $\mu^+ \to e^+ \nu_e\, \bar{\nu}_\mu$, gives a mixture of ν_e's and $\bar{\nu}_\mu$'s, but absolutely no other flavors. The $\bar{\nu}_\mu$'s that do not oscillate will give μ^+'s at the detector (allowing to count for the disappearance of $\bar{\nu}_\mu$'s), but the ν_e's can oscillate to a ν_μ and then give a μ^- at the detector, that is, a "wrong sign muon". As there are no ν_μ's in the beam, then, in the absence of detector backgrounds (which are much smaller than in the conventional case) any observation of μ^-'s signals the existence of a $\nu_e \rightsquigarrow \nu_\mu$ transition.

An additional advantage of muon-induced neutrino beams is that they are very well understood from the theoretical point of view.

The next generation of Superbeams will improve the precision of Δm^2_{23} and θ_{23}. Nevertheless, with all the conventional neutrino beams there will not be any significant improvement in the knowledge of:

- The angle θ_{13}, which is the key between the atmospheric and solar neutrino realms, for which the present CHOOZ bound is $\theta_{13} < 13°$.
- The sign of Δm^2_{23}, which determines whether the three-family neutrino spectrum is of the "direct" or "inverted" type (i.e. only one heavy state and two almost degenerate light ones, or the reverse).
- Leptonic CP-violation.
- The precise study of matter effects in the ν propagation through the Earth: a model-independent experimental confirmation of the MSW effect will not be available.

The main fact to note about the Neutrino Factory is that simply by measuring both $\nu_e \rightsquigarrow \nu_\mu$ and $\bar{\nu}_e \rightsquigarrow \bar{\nu}_\mu$ one can access all of the interesting parameters which describe the neutrino mixing [DGH99]. So, although neutrino factories in principle allow the measurement of all possible transitions between one flavor neutrino to another, one can extract all the interesting physics precisely, by simply building a massive detector that can measure the charge and energy of muons, a well understood detector technology.

2.3 General Design

The design includes a very high-power proton driver, delivering on target typically 4 MW of beam power of protons with energy in excess of a few GeV. A super-conducting linac at 2.2 GeV has been studied at CERN, while the US design calls for a rapid cycling proton synchrotron at 16-24 GeV, and an upgrade of JHF is considered in Japan. Designing a target that can withstand the thermal shock and heat load naturally leads to a liquid jet target design, although rotating high temperature solids are also being considered. Pions produced are collected as efficiently as possible by a magnetic channel, which involves a 20 T solenoid or powerful magnetic horns. Pions quickly decay into muons with a similar energy spectrum. At this point the beam is $0.6\,m$ in diameter and has an energy spread of more than 100%.

A momentum interval near the largest particle density, typically $250 \pm 100\,\text{MeV}$, is monochromatized to within a few MeV by means of phase rotation, using a strong variable electric field to slow down the fastest particles and accelerate the slower ones. This requires low-frequency ($\sim 50 - 100$ MHz) RF cavities or an induction linac. To reduce the transverse emittance, cooling is necessary, and is provided by ionization cooling. This involves energy loss of muons through a low-Z material, like liquid hydrogen, in a strongly focusing magnetic field (solenoids of 5-10 T), which reduces momentum in all three dimensions, followed by accelerating RF cavities, which restore the longitudinal momentum. The net effect is a reduction of emittance, leading to a transverse beam size of a few centimeters.

This leads to a linear configuration, as shown in fig. 2.1, for the initial muon beam preparation section, or *muon front-end*. In this concept, each beam element is used only once. It could be interesting, to save hardware, to be able to perform phase rotation and/or transverse cooling in a recirculating configuration. Indeed, a system of large aperture FFAG accelerators with low frequency RF (around 1.5 MHz) is the key to the Japanese Neutrino Factory design. Also, much progress has recently been made on 'ring coolers', which allow both transverse and longitudinal cooling in a circular configuration.

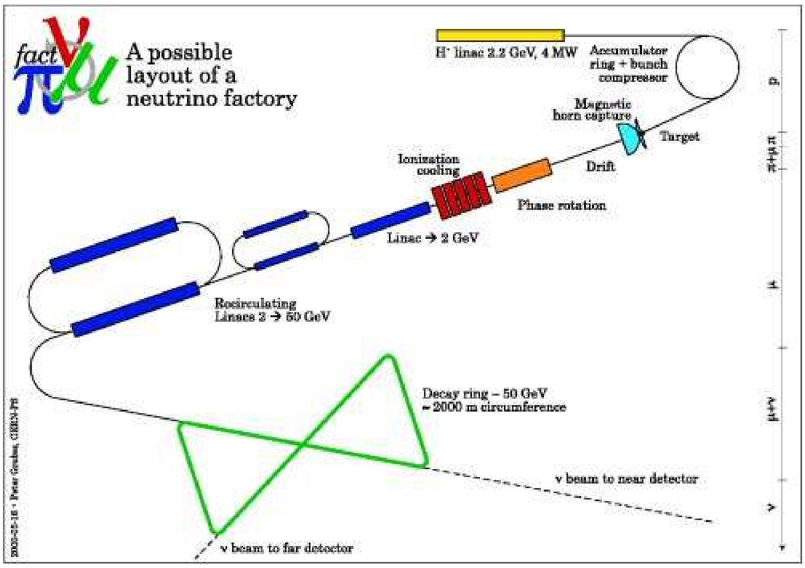

Figure 2.1. Schematic layout of the CERN scenario for a Neutrino Factory.

Assuming that the delicate questions of optics can be solved, these 'ring' options share the difficulty of injecting or extracting from a ring the very large emittance beam of muons available at the end of the decay channel. The possibility of very large aperture and very fast kickers is the major unknown and will be a key issue for these potentially cost-saving developments.

Finally, a linac followed by recirculating linacs —or FFAG accelerators— provides the fast acceleration of muons to an energy of 20 to 50 GeV. Around 10^{21} muons per year (of 10^7 seconds uptime) could then be stored in a ring, where they would circulate for a few hundred times during their lifetime. The storage ring can take the shape of a racetrack, triangle or bow-tie. These latter two configurations allow several beams of decay neutrinos to be produced in the direction of short and long-baseline experiments. Optics have been designed for muon storage rings of either triangular or bow-tie geometry, pointing for instance at distances of 730 km (which would correspond to the CERN-Gran Sasso beam line), and 2800 km (which would correspond to a more distant site in the Canary Islands or the Nordic countries).

Neutrino Factory design involves many new components and extrapolations beyond state-of-the-art technology. The first design studies have come to the conclusion that, with the present designs and technology, such a machine could indeed be built and reach the desired performance, but that various work is needed to bring the cost down. Assuming adequate funding, it is considered that about five years of research and development will be necessary to reach a point where a specific, cost-evaluated machine can be proposed.

2.4 Muon Beams, Fluxes and Rates

In the muon rest-frame, the distribution of $\bar{\nu}_\mu(\nu_\mu)$ and $\nu_e(\bar{\nu}_e)$ in the decay $\mu^\pm \rightarrow e^\pm \nu_e(\bar{\nu}_e)\bar{\nu}_\mu(\nu_\mu)$ is

$$\frac{d^2N}{d\,x\,d\Omega} = \frac{1}{4\,\pi}\,(f_0(x) \mp \mathcal{P}_\mu f_1(x) \cos\theta) \tag{2.1}$$

where $x = 2E_\nu/m_\mu$, $\mathcal{P}_\mu$ is the average muon polarization along the beam direction and θ is the angle between the neutrino momentum vector and the muon spin direction. The functions f_0 and f_1 are given in Table 2.1.

	$f_0(x)$	$f_1(x)$
ν_μ, e	$2\,x^2\,(3-2x)$	$2\,x^2\,(1-2\,x)$
ν_e	$12\,x^2\,(1-x)$	$12\,x^2\,(1-x)$

Table 2.1. Flux functions in the muon rest-frame as in [Gai00].

In the laboratory frame, the neutrino fluxes, boosted along the muon momentum vector, are given by

$$\begin{aligned}
\frac{d^2N_{\bar{\nu}_\mu,\nu_\mu}}{dy\,dS} &= \frac{4\,n_\mu}{\pi\,L^2\,m_\mu^6}\,E_\mu^4\,y^2\,(1-\beta\cos\phi)\Big\{\big(3\,m_\mu^2-4\,E_\mu^2\,y\,(1-\beta\cos\phi)\big) \\
&\mp\ \mathcal{P}_\mu\big(m_\mu^2-4\,E_\mu^2\,y\,(1-\beta\cos\phi)\big)\Big\} \\
\frac{d^2N_{\nu_e,\bar{\nu}_e}}{dy\,dS} &= \frac{24\,n_\mu}{\pi\,L^2\,m_\mu^6}\,E_\mu^4\,y^2\,(1-\beta\cos\phi)\Big\{\big(m_\mu^2-2\,E_\mu^2\,y\,(1-\beta\cos\phi)\big) \\
&\mp\ \mathcal{P}_\mu\big(m_\mu^2-2\,E_\mu^2\,y\,(1-\beta\cos\phi)\big)\Big\}
\end{aligned}\qquad(2.2)$$

where $\beta=\sqrt{1-m_\mu^2/E_\mu^2}$, E_μ is the parent muon energy, $y=E_\nu/E_\mu$, n_μ is the number of useful muons per year obtained from the storage ring and L is the distance to the detector. ϕ is the angle between the beam axis and the direction pointing towards the detector, assumed to be located in the forward direction of the muon beam. As an example, in fig. 2.2 the neutrino spectra are shown for a parent π^+ of 50 GeV.

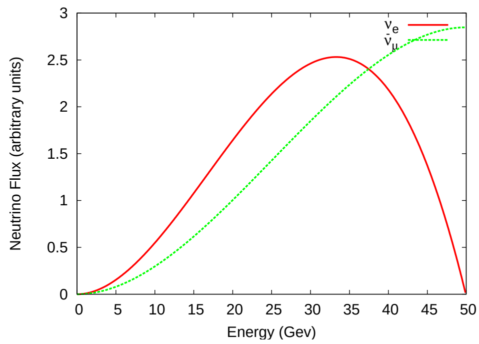

Figure 2.2. Energy distribution of a neutrino beam from the decay $\mu^+\to e^+\nu_e\bar{\nu}_\mu$.

Unlike traditional neutrino beams obtained from π and K decays, the fluxes in eq. (2.1), in the forward direction, present a leading quadratic dependence on E_ν. This comes from the shrinking of the angular opening of the neutrino beam due to the Lorentz boost. Moreover, since the deep-inelastic scattering cross section rises approximately linearly with neutrino energy, and the spectral shape only depends on x, the total number of events observed in a far detector will grow as E_μ^3. Geometrical solid-angle considerations suggest that, always assuming negligible detector size with respect to the baseline, the flux goes like $1/L^2$. Neglecting matter effects, the oscillation probabilities will depend on L/E_ν, so keeping the same oscillation probability and maximizing the number of events would ideally require very long baselines and large muon energies. The limitation to this, apart from the physical size of the Earth's diameter, comes from the matter effect, that depresses oscillation probabilities for baselines above 4,000 km (see fig. 2.3).

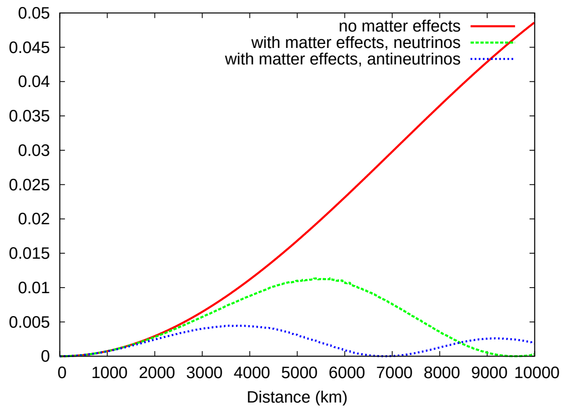

Figure 2.3. Oscillation probability $\nu_\mu \rightsquigarrow \nu_e$ versus distance, for a neutrino of 30 GeV, without matter effects (red, higher curve) and with matter effects (green for neutrinos and blue for antineutrinos).

2.5 Wrong Sign Muons

One of the main characteristics of the Neutrino Factory is that it delivers a well-defined beam free of intrinsic background. For instance, negative muons circulating in the ring will produce ν_μ, that in turn will again produce negative muons in the interaction with the detector. Positive muons are in principle only produced from the oscillation of the $\bar{\nu}_e$ component of the beam. The reverse argument applies for positive muons in the ring. In general, the so-called right-sign muons are $\mu^\pm \to \bar{\nu}_\mu(\nu_\mu) \rightsquigarrow \bar{\nu}_\mu(\nu_\mu) \to \mu^\pm$, the original type of muons coming from the beam, and wrong-sign muons $\mu^\pm \to \nu_e(\bar{\nu}_e) \rightsquigarrow \nu_\mu(\bar{\nu}_\mu) \to \mu^\mp$, the muons with a sign originally not present in the beam.

The first exploratory studies of the use of a Neutrino Factory were done in the context of two-family mixing. In this approximation, the wrong-sign muon signal in the atmospheric range is absent, since the atmospheric oscillation is $\nu_\mu \leftrightsquigarrow \nu_\tau$. The enormous physics reach of such signals in the context of three-family neutrino mixing was only recently realized. The CP-violating phase δ could be at reach. Using muon disappearance measurements, the precision in the knowledge of the atmospheric parameters θ_{23} and $|\Delta m^2_{23}|$ can reach the percent level at a Neutrino Factory. Furthermore, the sign of Δm^2_{23} can also be determined at long baselines, through sizable matter effects.

In practice, other processes can make contributions to the wrong sign muon sample. They are quite rare, but they can become important for low values of θ_{13}. The main backgrounds for a beam produced by μ^- decays are:

- $\bar{\nu}_\mu$ CC events where the right sign muon is lost, and a wrong sign muon is produced by the decay of a π, K or D. The most energetic muons are produced by D decays.

- ν_e CC events where the primary electron is not identified. In this case, D decays are not a major problem since, due to the neutrino helicity, they would produce right sign muons. However, wrong sign muons can come from π and K decays.

- $\bar{\nu}_\mu$ and ν_e NC events where charm production is suppressed with respect to charged currents, and therefore also the main contributions are given by π and K decays.

These backgrounds can be rejected using the facts that muons coming directly from neutrino interactions are higher in energy and more separated from the hadronic jets than those produced in secondary decays. A cut on momentum and on the transverse momentum, Q_t, of the muon with respect to the jet can reduce the background to wrong sign muons by several orders of magnitude.

2.6 Detection

The measurement of wrong sign muons calls for a massive detector weighing ~ 50 kton, with the capability of muon identification and the measurement of their charge. There are several technologies that could fulfill that. One of the most promising of such detectors is the Large Magnetized Calorimeter.

2.6.1 A Large Magnetized Calorimeter

The proposed apparatus, shown in fig. 2.4, is a large cylinder of 10 m radius and 20 m length, made of 6 cm thick iron rods interspersed with 2 cm thick scintillator rods built of 2 m long segments. The light read-out on both ends allows the determination of the spatial coordinate along the scintillator rod. The detector mass is 40 kton, and a superconducting coil generates a solenoidal magnetic field of 1 T inside the iron. A neutrino traveling through the detector sees a sandwich of iron and scintillator, with the $x-y$ coordinates being measured from the location of the scintillator rods, and the z coordinate from their longitudinal segmentation.

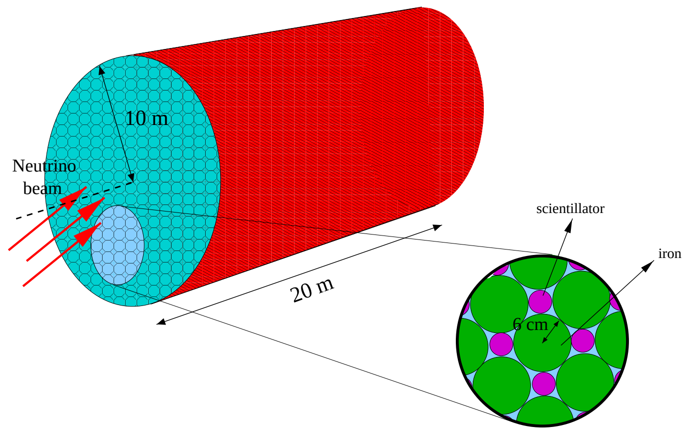

Figure 2.4. Sketch for the Large Calorimeter for the Neutrino Factory.

The performance of this detector would be similar to that of MINOS. The main difference lies in the mass, which is an order of magnitude larger, and in the smaller surface-to-volume ratio which together seem to make it superior for the detection of ν_μ and $\bar{\nu}_\mu$ events.

The discrimination of physical backgrounds from the signal is based on the fact that the μ^- produced in a ν_μ CC signal event is harder and more isolated from the hadron shower axis than in background events ($\bar{\nu}_\mu$ CC, ν_e CC, $\bar{\nu}_\mu$ NC and ν_e NC).

2.7 Oscillation Physics at the Neutrino Factory

As was commented before, in principle simply by measuring both $\nu_e \rightsquigarrow \nu_\mu$ and $\bar{\nu}_e \rightsquigarrow \bar{\nu}_\mu$, one can access all of the interesting parameters which describe the neutrino mixing, and so extract all the interesting physics precisely, by simply building a massive detector that can measure the charge and energy of muons.

2.7.1 Oscillation Probabilities in Matter

The exact oscillation probabilities in matter when no mass difference is neglected have been derived analytically by Zaglauer and Schwarzer [ZS88]. However, the physical implications of their formulas are not easily derived. A convenient and precise approximation is obtained by expanding to second order in the following small parameters: θ_{13}, Δ_{13}/Δ_{23}, Δ_{12}/A and $\Delta_{12}L$:

$$
\begin{aligned}
P_{\nu_e\nu_\mu(\bar{\nu}_e\bar{\nu}_\mu)} &= s_{23}^2 \sin^2(2\theta_{13}) \left(\frac{\Delta_{13}}{B_\mp}\right)^2 \sin^2\!\left(\frac{B_\mp L}{2}\right) \\
&+ c_{23}^2 \sin^2(2\,\theta_{12}) \left(\frac{\Delta_{12}}{A}\right)^2 \sin^2\!\left(\frac{A\,L}{2}\right) \\
&+ J\,\frac{\Delta_{12}}{A}\frac{\Delta_{13}}{B_\mp} \sin\!\left(\frac{A\,L}{2}\right) \sin\left(\frac{B_\mp L}{2}\right) \cos\left(\pm\,\delta - \frac{\Delta_{13}L}{2}\right)
\end{aligned}
\tag{2.3}
$$

where $\Delta_{ij} = \frac{\Delta m_{ij}^2}{2E_\nu}$, $A = \sqrt{2}G_F n_e$ is the matter parameter, $B_{\mp} = |A \mp \Delta_{13}|$ and

$$J \equiv \cos\theta_{13} \sin 2\,\theta_{13} \sin 2\,\theta_{23} \sin 2\,\theta_{12} \tag{2.4}$$

In the limit $A \rightarrow 0$, this expression reduces to the simple formula in vacuum

$$\begin{aligned} P_{\nu_e\nu_\mu(\bar{\nu}_e\bar{\nu}_\mu)} &= s_{23}^2 \sin^2 2\theta_{13} \sin^2\left(\frac{\Delta_{13}\,L}{2}\right) \\ &+ c_{23}^2 \sin^2 2\theta_{12} \sin^2\left(\frac{\Delta_{12}\,L}{2}\right) \\ &+ J\cos\left(\pm\,\delta - \frac{\Delta_{13}\,L}{2}\right)\frac{\Delta_{12}L}{2}\sin\left(\frac{\Delta_{13}\,L}{2}\right) \end{aligned} \tag{2.5}$$

Matter effects induce an asymmetry between neutrinos and antineutrinos oscillation probabilities even for vanishing δ. For this reason, a CP-odd asymmetry would not be the most transparent observable.

In the standard decomposition of the PMNS matrix, it is the second rotation matrix the one that contains the angle θ_{13}, which acts as a link between the atmospheric and solar realms. It also contains the CP-violation phase δ. We know from experimental data that θ_{13} is small, and we know from solar and atmospheric experiments that there exists a strong mass hierarchy in the neutrino sector ($\Delta m_{23}^2 \gg \Delta m_{12}^2$). The consequence is that solar and atmospheric oscillations approximately decouple in two 2-by-2 mixing phenomena which results in the second matrix in the parametrization of the PMNS matrix becoming the identity matrix. Most experiments until now have been sensitive either to the atmospheric or the solar parameters. What makes the neutrino factory unique is precisely its ability to measure or set very stringent limits on these parameters, θ_{13} and δ.

2.7.2 Precision Measurement of Known Oscillations

The parameters governing the leading atmospheric oscillation $\nu_\mu \rightsquigarrow \nu_\tau$, θ_{23} and Δm_{23}^2, can be measured to an unprecedented precision with the Neutrino Factory. These parameters are mainly determined from the disappearance of muon neutrinos in the beam, observed using right sign muon events. The maximum of the oscillation probability will produce a dip in the visible spectrum. The energy position of this dip will be correlated to the value of Δm_{23}^2, and the depth to θ_{23}. It is therefore favorable to choose an energy and baseline such that the maximum of the oscillation probability lies comfortably inside the detectable spectrum.

The precision on the measurement of the oscillation parameters has been addressed by several groups, and is normally performed by a fit on the energy spectra of the event classes. The expected precisions for the Neutrino Factory are of 1% for Δm_{23}^2 and of 10% for $\sin^2\theta_{23}$.

2.7.3 Sensitivity to θ_{13}

So far, the most accurate information on θ_{13} is the CHOOZ limit $\sin^2 2\theta_{13} < 0.11$. In a favorable case, a non-zero value of this parameter could be discovered before the Neutrino Factory by experiments running in first-generation neutrino beams, such as ICARUS and MINOS. Much larger sensitivity will however be achieved by Superbeams, for instance T2K. But experiments performed with conventional beams from pion decays will always be limited by the presence of a ν_e component in the beam itself, representing an irreducible background to the search for $\nu_\mu \rightsquigarrow \nu_e$ oscillations.

On the other hand, the Neutrino Factory would have a significantly improved sensitivity to θ_{13} thanks to the wrong sign muon signal, that measures the oscillation $\nu_e \rightsquigarrow \nu_\mu$, where the oscillated muon neutrinos are easily separated from the beam component of opposite sign by measuring the charge of the produced muon.

Applying strong cuts on muon momentum and isolation, the background from the decays of charmed particles, kaons and pions, can be reduced by as much as a factor 10^6, keeping an efficiency of about 40%.

The parameter θ_{13} is extracted from a fit to the energy distribution of the wrong sign muons. Moreover, from the formula of the oscillation probability we see that the value of θ_{13} has a limited influence on the spectral shape, and even factorizes out from the energy dependence in the approximation $\Delta m^2_{12} = 0$, so most of the information actually comes from just counting wrong sign muon events.

The background level is the ultimate limiting factor for this measurement, and the sensitivity would be of the order of $\sin^2\theta_{13} \sim 5 \times 10^{-5}$ (see fig. 2.5).

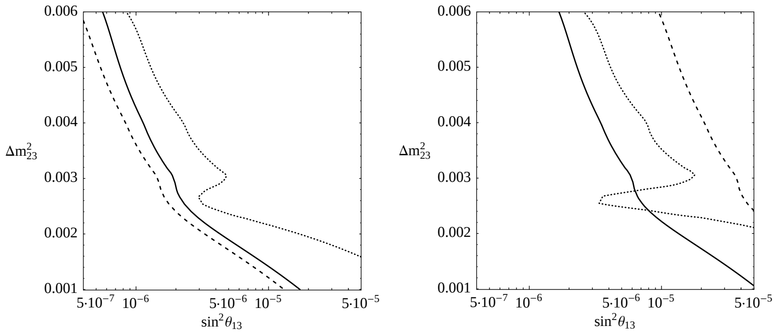

Figure 2.5. Sensitivity to $\sin^2\theta_{13}$ for a magnetized iron detector, without (left) and with (right) realistic backgrounds. The three lines correspond to baselines of 730 (dashed), 3500 (solid) and 7300 km (dotted).

2.7.4 Sensitivity to CP violation

Detecting the presence of a complex phase in the leptonic mixing matrix is one of the most ambitious goals of neutrino physics, and would justify the effort of building a Neutrino Factory.

In eq. (2.3) it is seen that the term with δ is only suppressed in the parameters Δm_{12}^2 and θ_{13}. Since the CP-even parts of the probabilities are always larger than the CP-odd parts, they dominate the number of events and thus the error on the measured asymmetry.

Due to the small energy dependence induced by CP violation, the use of spectral information to have a simultaneous measurement of δ and θ_{13} is not very effective, and only helps under some conditions. The simultaneous fits in θ_{13} and δ reveal for most of the cases a strong correlation between the two parameters (see fig. 2.6).

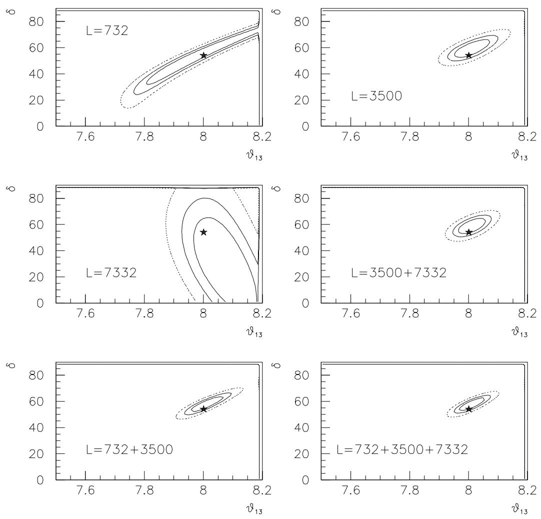

Figure 2.6. Contour plots resulting from a χ^2 fit of θ_{13} and δ, at 1, 2 and 3 σ. The parameters used to generate the data are depicted by a star, and the baseline which is used for the fit indicated in each plot.

Chapter 3
Reducing Uncertainties

3.1 HARP's Measure of Hadronic Cross-Sections

The HARP experiment [C+] was designed to perform a systematic and precise study of hadron production (pions and kaons in particular) for beam momenta between 1.5 and 15 GeV/c and target nuclei ranging from hydrogen to lead. The detector was located at CERN, in the PS beam. The DAQ recorded 420 million events during the years 2001 and 2002.

The physics program of HARP includes: a) the measurement of pion yields for a variety of energies and targets relevant for the design of the proton driver of a future Neutrino Factory [GCH02]; b) the measurement of pion yields on low Z targets as well as on cryogenic oxygen and helium targets, useful to improve the precision of atmospheric neutrino flux calculations [BGL+04]; and c) the measurement of pion and kaon yields, relevant for the calculation of the neutrino fluxes of experiments such as MiniBooNE [BooNe] and K2K [K2K].

HARP (fig. 3.1) is a large acceptance spectrometer, with two distinct regions. In the forward part of the apparatus (up to polar angles of about 250 mrad), the main tracking devices are a set of large drift chambers. Magnetic analysis is provided by a 0.4 T dipole magnet and particle identification relies on the combination of a threshold Cerenkov detector (CHE), a time-of-flight wall (TOFW) and an electromagnetic calorimeter (ECAL). In the rest of the solid angle the main tracking device is a TPC, which is complemented by a set of RPC detectors for time-of-flight measurements. The target is located inside the TPC. In addition, sophisticated beam instrumentation (including three timing detectors and threshold Cerenkov detectors) provides identification of the incoming particle and allows the interaction time at the target to be measured.

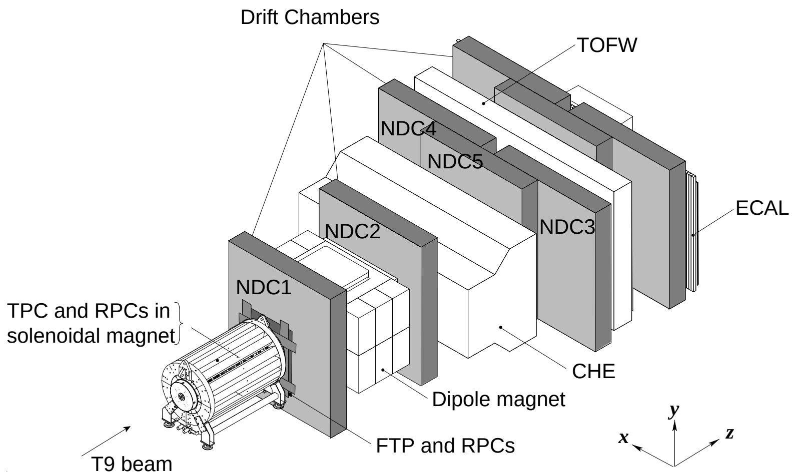

Figure 3.1. The HARP detector.

Given the immediate interest of the MiniBooNE and K2K experiments in a measurement of the production cross sections for pions and kaons at the energies and targets relevant for their beam setups, the HARP collaboration has given priority to the analysis of those particular data sets.

3.2 Forward Tracking and Particle Identification

3.2.1 Tracking

Tracking of forward-going particles is done by a set of large drift chambers (NDC) placed upstream and downstream of the dipole magnet. The chambers were recuperated from the NOMAD experiment and their properties are described in [A+02]. Each NDC module is made of four chambers, and each chamber of three planes of wires with tilted angles $-5°$, $0°$ and $5°$. The single-wire efficiency is of the order of 80%, and the spatial resolution approximately $340\,\mu m$.

The reconstruction builds 2D and 3D track segments in each NDC module (12 hits maximum), which are fitted to a straight line model via a Kalman Filter fit [FW].

Next, the algorithm attempts all possible combinations (which include at least a 3D segment) to connect tracking objects in the modules downstream of the dipole magnet. Combinations such as 3D + 2D or even 3D + hits-not-associated are valid ways to build longer, 3D segments.

To measure the momentum it is necessary to connect a (3D) segment downstream of the dipole with at least one space point upstream of the dipole. Since one can impose the constraint that all tracks emanate from the event vertex this point is always known and therefore the necessary and sufficient condition for a particle emanating from the target to have its momentum measured is that a 3D segment can be measured by the combination of downstream NDC chambers.

3.2.2 Particle Identification

Particle identification (PID) in the forward region of the spectrometer combines the information provided by beam detectors and three systems located downstream the dipole magnet. Namely, the threshold Cerenkov detector, the time-of-flight wall, and the electromagnetic calorimeter. These subsystems have been described in [Cer04]. Their combined information results in good PID over the whole range of relevant momenta, as well as redundancy due to overlaps. Pion/proton separation is provided by TOFW up to 4.5 GeV/c, and by the CHE above 3 GeV/c. Electron/pion separation is covered by the CHE below 3 GeV/c and by the ECAL above 2 GeV/c. Finally the kaon contamination can be estimated with the CHE above 3 GeV/c and with the TOFW below this energy.

3.3 Implications for Neutrino Physics

The dominant uncertainty in neutrino flux predictions for conventional neutrino beams is due to the pion production uncertainty in the hadronic interactions of primary beam protons with the nuclear target material.

3.3.1 MiniBooNE and SciBooNE

HARP provides cross section data to the Booster Neutrino Beam (BNB) at Fermilab. The BNB originates from protons accelerated to 8.9 GeV/c by the booster and then collided against a beryllium target. A fundamental input for the calculation of BNB's resulting ν_μ flux is HARP's measurement of the π^+ cross-sections from a thin 5% nuclear interaction length (λ_I) beryllium target at 8.9 GeV/c proton momentum, which is presented in [C+07].

The absolutely normalized double-differential cross-section for the process $p\,\mathrm{Be} \rightarrow \pi^+ X$ can be expressed in bins of pion kinematic variables in the laboratory frame, (p_π, θ_π), as

$$\frac{d^2\sigma^{\pi^+}}{dp\,d\Omega}(p_\pi,\theta_\pi) = \frac{A}{N_A\,\rho\,t}\,\frac{1}{\Delta p\,\Delta\Omega}\,\frac{1}{N_{\mathrm{pot}}}\,N^{\pi^+}(p_\pi,\theta_\pi) \tag{3.1}$$

where

- $\frac{d^2\sigma^{\pi^+}}{dp\,d\Omega}$ is the cross-section in cm^2/(GeV/c)/srad for each (p_π, θ_π) bin covered in the analysis.

- $\frac{A}{N_A\,\rho}$ is the reciprocal of the number density of target nuclei for Be (1.2349×10^{23} per cm^3).
- t is the thickness of the beryllium target along the beam direction. The thickness is measured to be 2.046 cm with a maximum variation of 0.002 cm.
- $\Delta p = p_{\max} - p_{\min}$ and $\Delta\Omega = 2\,\pi\,(\cos(\theta_{\min}) - \cos(\theta_{\max}))$ are the bin sizes in momentum and solid angle.
- $N_{\rm pot}$ is the number of protons on target after event selection cuts.
- $N^{\pi^+}(p_\pi,\ \theta_\pi)$ is the yield of positive pions in bins of true momentum and angle in the laboratory frame.

Equation 3.1 can be generalized to give the inclusive cross-section for a particle of type α:

$$\frac{d^2\sigma^\alpha}{dp\,d\Omega}(p,\theta) = \frac{A}{N_A\,\rho\,t}\,\frac{1}{\Delta p\,\Delta\Omega}\,\frac{1}{N_{\rm pot}}\,M^{-1}_{p\theta\alpha p'\theta'\alpha'}\,N^{\alpha}(p,\theta) \tag{3.2}$$

where reconstructed quantities are marked with a prime and $M^{-1}_{p\theta\alpha p'\theta'\alpha'}$ is the inverse of a matrix which fully describes the migrations between bins of true and reconstructed quantities, namely: lab frame momentum, p, lab frame angle, θ, and particle type, α.

There is a background associated with beam protons interacting in materials other than the nuclear target (parts of the detector, air, etc.). These events are subtracted by using data collected without the nuclear target in place where the sets have been normalized to the same number of protons on target. This procedure is referred to as the "empty target subtraction":

$$N^{\alpha'}(p',\theta') \rightarrow [N^{\alpha'}_{\rm target}(p',\theta') - N^{\alpha'}_{\rm empty}(p',\theta')] \tag{3.3}$$

The event selection is performed in the following way: a good event is required to have a single, well reconstructed and identified beam particle impinging on the nuclear target. A downstream trigger in the forward trigger plane (FTP) is also required to record the event, necessitating an additional set of unbiased, pre-scaled triggers for absolute normalization of the cross-section. These pre-scale triggers (1/64 for the 8.9 GeV/c Be data set) are subject to exactly the same selection criteria for a 'good' beam particle as the event triggers allowing the efficiencies of the selection to cancel, thus adding no additional systematic uncertainty to the absolute normalization of the result. Secondary track selection criteria have been optimized to ensure the quality of the momentum reconstruction as well as a clean time-of-flight measurement while maintaining high reconstruction and particle identification efficiencies.

The double-differential inelastic cross-section for the production of positive pions from col- lisions of 8.9 GeV/c protons with beryllium have been measured in the kinematic range from 0.75 GeV/$c \leqslant p_\pi \leqslant$ 6.5 GeV/c and 0.030 rad $\leqslant \theta_\pi \leqslant$ 0.210 rad, subdivided into 13 momentum and 6 angular bins. Systematic errors have been estimated. A full $(13 \times 6)^2 = 6048$ element covariance matrix has been generated to describe the correlation among bins. The data are presented graphically as a function of momentum in 30 mrad bins in figure 3.2. To characterize the uncertainties on this measurement the diagonal elements of the covariance matrix are plotted on the data points in the figure. A typical total uncertainty of 9.8% on the double-differential cross-section values and a 4.9% uncertainty on the total integrated cross-section are obtained.

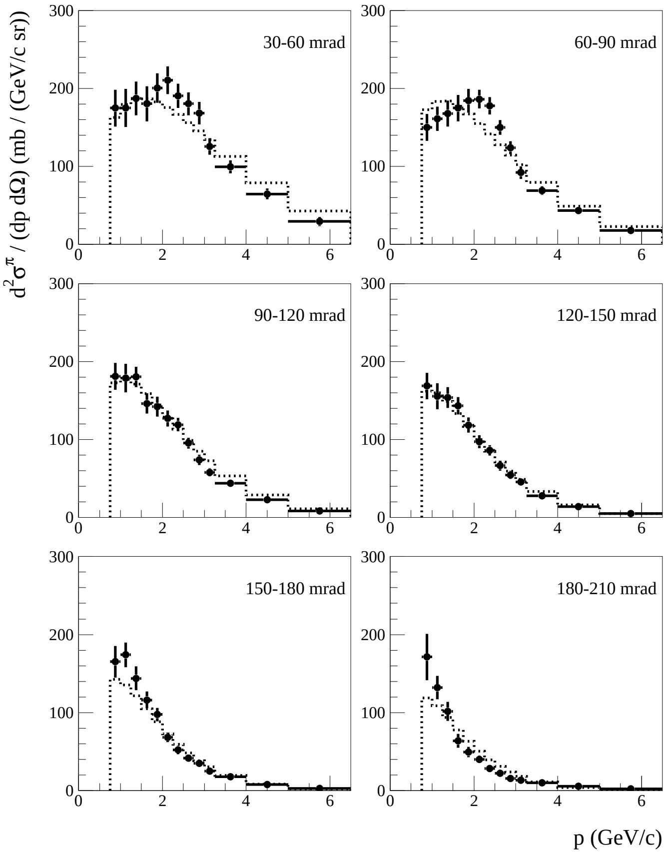

Figure 3.2. HARP measurements of the double-differential production cross-section of positive pions, $d^2\sigma^{\pi^+}/dp\, d\Omega$, from 8.9 GeV/$c$ protons on 5% λ_I beryllium target as a function of pion momentum, p, in bins of pion angle, θ, in the laboratory frame. The error bars shown include statistical errors and all (diagonal) systematic errors. The dotted histograms show the Sanford-Wang parametrization that best fits the HARP data.

Sanford and Wang have developed an empirical parametrization for describing the production cross-sections of mesons in proton-nucleus interactions [Wan73]. This parametrization has the functional form:

$$\frac{d^2\sigma(pA\to\pi^+ X)}{dp\,d\Omega}(p,\theta) = \exp\left[c_1 - c_3\frac{p^{c_4}}{p_{\text{beam}}^{c_5}} - c_6\,\theta\,(p - c_7\,p_{\text{beam}}\cos^{c_8}\theta)\right]\times p^{c_2}\,(1-\frac{p}{p_{\text{beam}}})$$

where X denotes any system of other particles in the final state, p_{beam} is the proton beam momentum in GeV/c, p and θ are the π^+ momentum and angle in units of GeV/c and radians respectively, $d^2\sigma/dp\ d\Omega$ is expressed in units of mb/ (GeV/c sr), $d\Omega = 2\,\pi\,d(\cos\theta)$, and the parameters $c_1, ..., c_8$ are obtained from fits to meson production data.

The MiniBooNE neutrino beam is produced from the decay of π and K mesons which are produced in collisions of 8.9 GeV/c protons from the Fermilab Booster on a 71 cm beryllium target. The neutrino flux prediction is generated using a Monte Carlo simulation. In this simulation the primary meson production rates are taken from a fit of existing data with a Sanford-Wang empirical parametrization in the relevant region. The results from HARP, being for protons at exactly the booster beam energy, are then a critical addition to these global fits.

3.3.2 K2K

The first HARP physics publication [HARP06] reported measurements of the π^+ production cross-section from an aluminum target at 12.9 GeV/c proton momentum, which corresponds to the energies of the KEK PS and the target material used by the K2K experiment. The results are incorporated into the K2K beam Monte Carlo simulation to estimate the neutrino spectra at the Near Detector (ND) and SuperKamiokande (SK) and the energy dependence of the far-to-near (F/N) flux ratio in the absence of neutrino oscillations. The relatively-normalized fluxes at ND and SK predicted by HARP, Φ^{ND} and Φ^{SK}, are shown in fig. 3.3, together with the associated total systematic uncertainties, by the empty circles with error bars.

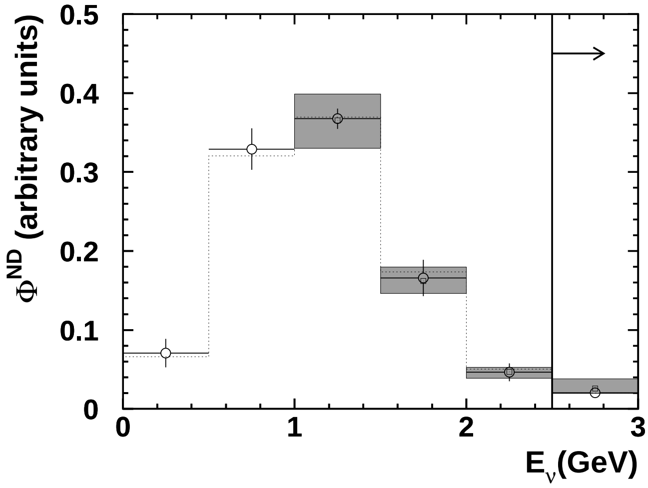

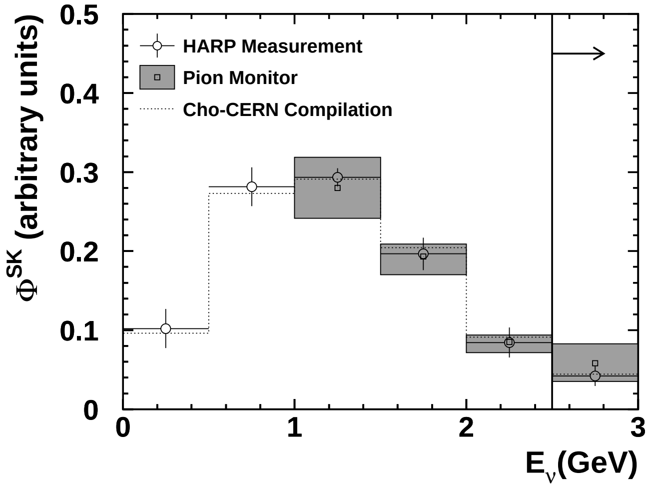

Figure 3.3. Relatively-normalized muon neutrino flux predictions at the near (top) and far (bottom) detectors. The empty circles with error bars show the central values and shape-only errors based on the HARP π^+ production measurement, the empty squares with shaded error boxes show the central values and errors from the pion monitor (PIMON) measurement, and the dotted histograms show the central values from the Cho-CERN compilation of older (non-HARP) π^+ production data. The PIMON predictions are normalized such that the integrated fluxes above 1 GeV neutrino energy match the HARP ones, at both the near and far detectors.

The HARP π^+ Sanford-Wang parameters uncertainties and correlations are propagated into flux uncertainties using standard error matrix propagation methods: the flux variation in each energy bin is estimated by varying a given Sanford-Wang parameter by a unit standard deviation in the beam MC simulation. Other systematic errors that are taken into account [K2K06] include:

- Proton-aluminum hadronic interaction length.
- Overall charged and neutral kaon production normalization.
- Imperfect knowledge of secondary hadronic interactions (such as π^+ absorption in the targets and horns).
- Knowledge of the magnetic field in the horn.
- Beam optics.

The F/N flux ratio, Φ^{SK}/Φ^{ND}, predicted by the HARP π^+ production measurement for primary hadronic interactions with the systematic errors mentioned above, in the absence of neutrino oscillations, is shown in figure 3.4 as a function of neutrino energy.

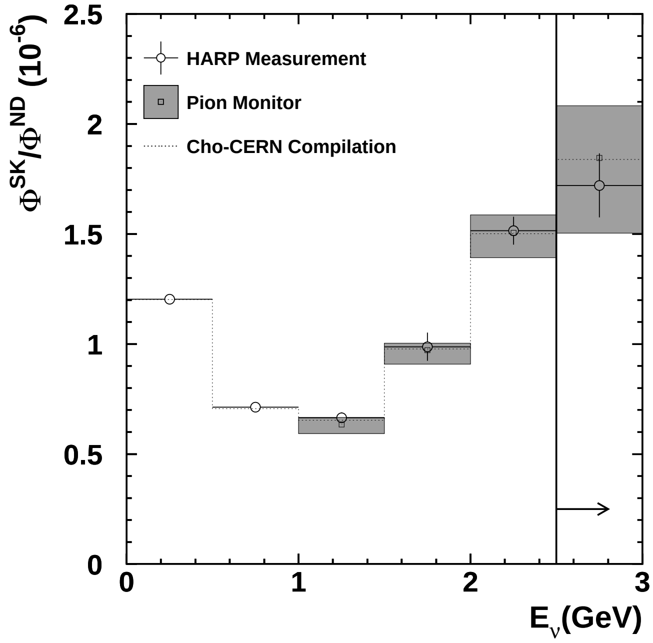

Figure 3.4. Prediction for the K2K muon neutrino F/N flux ratio in absence of oscillations. The empty circles with error bars show the central values and systematic errors on the muon neutrino flux predictions from the HARP π^+ production measurement, the empty squares with shaded error boxes show the central values and errors from the pion monitor measurement, and the dotted histograms show the central values from the Cho-CERN compilation of older (non-HARP) π^+ production data.

The flux ratio uncertainty is at the 2-3% level below 1 GeV neutrino energy, and of the order of 4-9% above 1 GeV. The dominant contribution to the uncertainty in the flux ratio comes from the HARP π^+ measurement itself. In particular, the uncertainty in the flux ratio predicted integrated over all neutrino energies is 2.0%, where the contribution of the HARP π^+ production uncertainty is 1.4%.

Even so, the HARP π^+ measurement provides a significant reduction of the dominant systematic error associated with the calculation of the far-to-near ratio and thus an increased K2K sensitivity to the oscillation signal.

3.3.3 Atmospheric Neutrinos

A similar analysis has been performed using the HARP forward spectrometer for the measurement of the double-differential production cross-section of $\pi^\pm$ in the collision of 12 GeV/c protons with a 5% λ_I carbon target. The results are shown in figure 3.5. These measurements are important for a precise calculation of the atmospheric neutrino flux and for a prediction of the development of extended air showers.

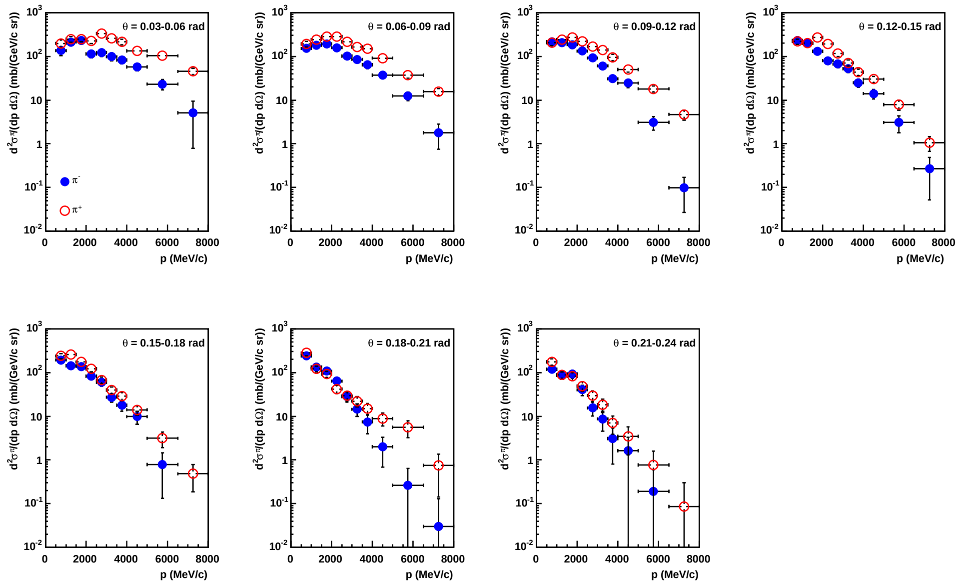

Figure 3.5. Measurements of the double-differential production cross-sections of π^+ (open circles) and π^- (closed circles) from 12 GeV/c protons on 5% λ_I carbon target as a function of pion momentum, p, in bins of pion angle, θ, in the laboratory frame. The error bars shown include statistical errors and all (diagonal) systematic errors.

3.3.4 Neutrino Factory

Also, there are results on the measurements of the double-differential cross-section for the production of charged pions in proton-tantalum collisions emitted at large angles from the incoming beam direction [HARP07]. The pions were produced by proton beams in a momentum range from $3\,\mathrm{GeV}/c$ to $12\,\mathrm{GeV}/c$ hitting a tantalum target with a thickness of 5% λ_I. The angular and momentum range covered by the experiment ($100\,\mathrm{MeV}/c \leqslant p < 800\,\mathrm{MeV}/c$ and $0.35\,\mathrm{rad} \leqslant \theta < 2.15\,\mathrm{rad}$) is of particular importance for the design of a Neutrino Factory. Track recognition, momentum determination and particle identification were all performed based on the measurements made with the TPC. Results for the double-differential cross-sections $d^2\sigma/dp\,d\theta$ at four incident proton beam momenta (3, 5, 8 and 12 GeV/c) are shown in figure 3.6.

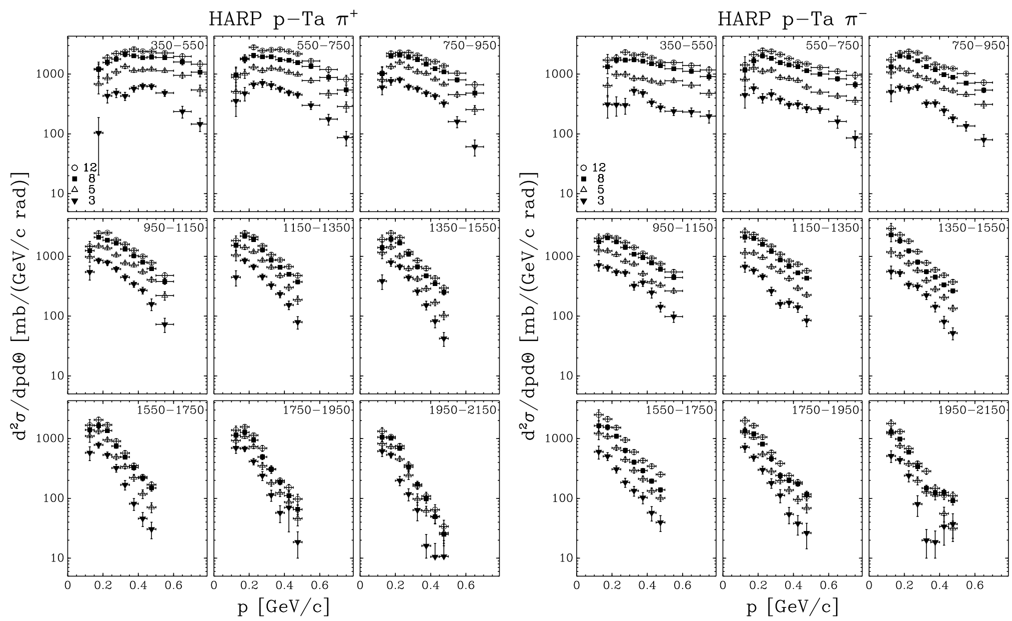

Figure 3.6. Double-differential cross-sections for π^+ (left) and π^- (right) production in $p-$Ta interactions as a function of momentum displayed in different angular bins (shown in mrad in the panels). The results are given for all incident beam momenta (filled triangles: 3 GeV/c; open triangles: 5 GeV/c; filled rectangles: 8 GeV/c; open circles: 12 GeV/c). The error bars take into account the correlations of the systematic uncertainties.

Similar analyses are being performed for the Be, C, Cu, Sn and Pb targets using the same detector, which will allow a study of A-dependence of the pion yields with a reduced systematic uncertainty to be performed.

Chapter 4

Suppressing Correlations and Degeneracies

4.1 Superbeams as an Intermediate Step

The notion of "super beams" was introduced by Richter [Ric00], who suggested that a conventional neutrino beam of very high intensity could be competitive with the pure two-flavor neutrino beams produced by the Neutrino Factory. Thanks to the fact that the solution to the solar anomaly has been confirmed to be in the LMA region, a Superbeam could largely improve our knowledge of Δm^2_{23}, θ_{23} and θ_{13}, as well as provide some sensitivity to the CP violating phase δ. On the other hand, the ultimate sensitivity to these parameters, in particular to δ, will still require the pure and intense beams of a Neutrino Factory.

4.1.1 Rationale

The signal to noise ratio in an experiment looking for the appearance of a type of neutrino not initially present in the beam, in a two-neutrino model, is:

$$\frac{P(\nu_1 \rightsquigarrow \nu_2)}{P(\nu_1 \rightsquigarrow \nu_1)} = \frac{A^2 \sin^2(\Delta m^2 L/4E)}{1 - A^2 \sin^2(\Delta m^2 L/4E)} \tag{4.1}$$

where A is the mixing amplitude, Δm^2 is the difference of the squares of the masses, L is the distance from the source to the detector, and E is the beam energy. The optimum signal to noise ratio comes when the sine term is equal to one: $\Delta m^2 L/4E = (2n+1)\pi/2$. However, all of the muon storage ring designs have high energy, making this factor small with the known mass differences. On the other hand, a conventional low-energy beam can be tuned to make it maximum.

Neutrino cross sections increase approximately linear with the energy, and the flux of neutrinos increases with the square of the energy of the parent particle. This gives an overall factor E^3 that makes going to high energy very appealing. However, in an experiment looking for the appearance of a neutrino species different from the primary species (as is the golden channel in a Neutrino Factory), the probability is proportional to E^{-2}, so there is only an overall E factor in the improvement of Neutrino Factories versus conventional beams.

These considerations and the big cost of a Neutrino Factory spurred the interest in a thorough study of Superbeams as alternatives to the Neutrino Factory.

4.1.2 Neutrino Generation in a Superbeam

A conventional neutrino beam is produced by hitting a nuclear target with an intense hadron beam, then sign-selecting and letting decay the resulting hadrons through a beam decay tunnel. At the end of the tunnel there is an absorber, where the copiously produced muons, a byproduct of pion and kaon decay, are ranged out before most of them can decay.

The resulting neutrino beam is mostly made of ν_μ (assuming that π^+ were selected). Nevertheless, kaon and muon decays result in small but sizable contamination of ν_e and $\bar{\nu}_e$. Opposite sign pion feed-through yields also some contamination of $\bar{\nu}_\mu$. Fig. 4.1 shows a typical composition for these kind of neutrino beams.

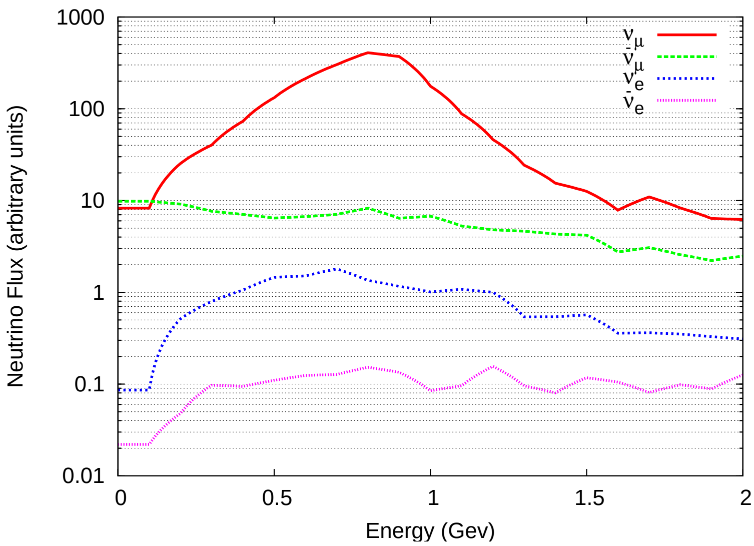

Figure 4.1. Fluxes of T2K. The beam is mostly made of ν_μ but there is a significant contamination of $\bar{\nu}_\mu$, ν_e and $\bar{\nu}_e$.

The contamination of other neutrino species is a handicap for the neutrino oscillation appearance experiments, in which one searches for a flavor not originally in the beam. Indeed this is the key advantage of Neutrino Factory beams, over conventional beams.

A Superbeam is just a conventional beam ($\pi^\pm \to \mu^\pm \, \nu_\mu(\bar{\nu}_\mu)$) of very high intensity. Thus, for π^+ selected in the horn, its basic composition is ν_μ with small admixtures of ν_e, $\bar{\nu}_e$ and $\bar{\nu}_\mu$. To gain some appreciation of the relative sensitivity of a conventional neutrino beam and a Neutrino Factory beam, it is useful to estimate the sensitivity to a $\nu_\mu \rightsquigarrow \nu_e$ oscillation search in the appearance mode, assuming a perfect detector. In a Neutrino Factory we will be able to see the probability $P_{\nu_\mu\nu_e}$ as soon as the expected appearance events $N_\mu^{\text{app}} = N_0 \; P_{\nu_e\nu_\mu} \sim 1$. The minimum $P_{\nu_e\nu_\mu}$ to which we are sensitive is then

$$P_{\nu_e\nu_\mu} \sim \frac{1}{N_0} \tag{4.2}$$

This is because there is no beam contamination. On the other hand, in the case of a conventional beam, we are sensitive as soon as $N_0 \, P_{\nu_\mu\nu_e} \sim \text{background} \simeq \sqrt{N_e}$, so the sensitivity to $P_{\nu_\mu\nu_e}$ goes as

$$P_{\nu_\mu\nu_e} \sim \frac{\sqrt{N_e}}{N_0} \tag{4.3}$$

so if the ν_e contamination is a fraction f of the primary ν_μ beam, $N_e = f \, N_0$, we have a sensitivity

$$P_{\nu_\mu\nu_e} \sim \frac{\sqrt{f}}{\sqrt{N_0}} \tag{4.4}$$

Although $\sqrt{f}$ is a small quantity, the key difference between conventional and muon-induced beams is clear comparing equations (4.2) and (4.4). In the first case the sensitivity improves "linearly" while in the second improves only with the square root of the total collected statistics.

Another issue concerns systematics in beam composition. While the neutrino spectra from muon decay can be computed to a great precision, the convoluted spectra in a conventional beam is affected by a number of uncertainties, the most important of which is the initial π/K ratio in the hadron beam, which affects the composition of the beam. Typically, these and other uncertainties translate into a systematic error at the level of few per cent in the conventional neutrino fluxes, to be compared with a few per mil in the case of a Neutrino Factory.

Other important aspects to be considered when designing a conventional beam are whether one prefers a wide or narrow band beam and the energy regime. Beam energies range typically from few hundred MeV to few hundred GeV, depending on the colliding hadron beam and beam optics. High energy yields more interactions, but sufficiently low energy yields a better control over backgrounds and less beam uncertainties.

4.1.3 Detection

Typical Superbeam source-detector distances are in the range of 150 – 300 km, in the peak of the neutrino oscillation. The detection of low energy neutrinos at those distances requires a massive target with high efficiency. Moreover, a search for ν_e appearance demands excellent rejection of physics backgrounds, namely μ misidentification and neutral current π^0 production, which should be controlled to a lower level than the irreducible beam-induced background.

Two technologies that have demonstrated excellent performance in the low energy regime while being able to provide massive targets are water Cerenkov detectors and diluted liquid scintillator detectors.

In spite of the fact that liquid scintillator detectors provide, a priori, more handles to reject backgrounds than their water Cerenkov counterparts, the only truly massive detectors built so far are of the latest type.

4.1.4 Water Cerenkov Detectors

An example of this kind of detectors is Super-Kamiokande, with its 40 kton of fiducial mass. The response of the detector to the neutrino beams was studied with the NUANCE neutrino physics generator [Cas02] and reconstruction algorithms developed for the Super-Kamiokande atmospheric neutrino analysis.

In the absence of neutrino oscillations, the dominant reaction induced by the beam is ν_μ quasielastic scattering, leading to a single observed muon ring. Recoiling protons are well below Cerenkov threshold at the energies of the generated neutrinos, and hence produce no rings. To unambiguously identify a potentially small ν_e appearance signal, it is essential to avoid confusion of muons with electrons. Thanks to the low energy of the neutrino beam, the Cerenkov threshold itself helps to separate muons and electrons, since a muon produced near the peak of the spectrum ($\sim$ 300 MeV) cannot be confused with an electron of comparable momentum; instead it will appear to be a much lower energy ($\sim$ 100 MeV) electron.

Particle identification exploits the difference in the Cerenkov patterns produced by the showering ("e-like") and non-showering ("μ-like") particles. Besides, for the energies of interest in this beam, the difference in Cerenkov opening angle between an electron and a muon can also be exploited. Furthermore, muons which stop and decay produce a detectable delayed electron signature which can be used as an additional handle for background rejection.

Production of π^0 through neutral current resonance-mediated and coherent processes is another major source of background, which is, however, suppressed by the low energy of the beam and the relatively small boost of the resulting π^0. This results in events where the two rings are easily found by a standard π^0 search algorithm.

4.1.5 Sensitivity

To illustrate the sensitivity of a Superbeam we will use a 40 kton water or liquid oil detector located at 130 km from the source. Actually, the last designs for Superbeams that are under consideration include much bigger detectors, UNO-style, of about 400 kton.

4.1.5.1 Sensitivity to the Atmospheric Parameters

A 40 kton detector has excellent opportunities of precision measurements of $\sin^2\theta_{23}$ and Δm^2_{23} with a ν_μ disappearance experiment. Given the mean beam energy of the ν_μ beam, $(1.27L/E)^{-1} = 1.6 \times 10^{-3}\,\mathrm{eV}^2$, and $P_{\nu_\mu\nu_\mu}$ is just at its minimum.

To illustrate the precision in measuring Δm^2_{23} and θ_{23} in case of positive signal, fig. 4.2 shows the result of 5 years exposure in case the oscillation occurs with $\sin^2 2\theta_{23} = 0.98$ and $\Delta m^2_{23} = 3.8, 3.2$ or $2.5 \times 10^{-3}\,\mathrm{eV}^2$. To make the reconstruction it is not possible to bin much in energy, due to the smearing caused by the Fermi motion.

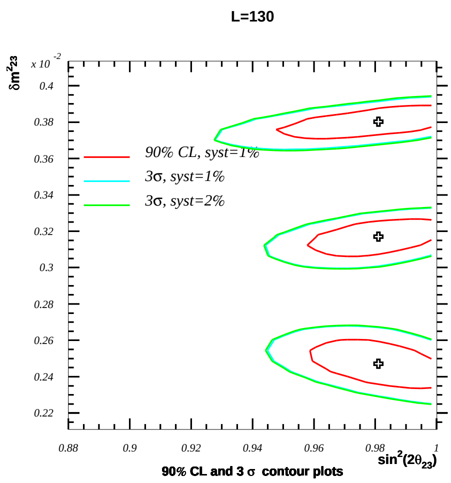

Figure 4.2. Fits in the Δm^2_{23}, $\sin^2 2\theta_{23}$ plane after 5 years of run, for a systematic uncertainty of 2%. The crosses sign the initial points.

4.1.5.2 Sensitivity to CP violation

Unfortunately for a water Cerenkov detector, the $\bar{\nu}$ + ^{16}O cross-section is approximately six times less than that for $\nu + {}^{16}O$ at these energies, diminishing the experiment's sensitivity to CP violation.

Because of the big correlations between θ_{13} and δ, a simultaneous fit of both parameters is convenient. Fig. 4.3 shows the confidence level contours for a simulation fit of θ_{13} and δ, corresponding to the three values of $\theta_{13} = 5°, 8°, 10°$ and a maximal CP violation phase of $\delta = \pm\, 90°$. Since the sensitivity is dominated by the low antineutrino statistics, this is done for a 10 year run with focused π^- and a 2 year run with π^+.

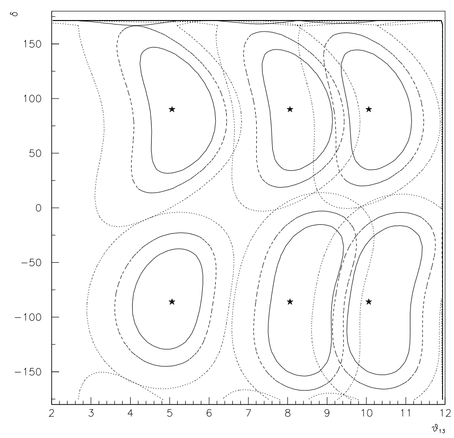

Figure 4.3. 1, 2 and 3 σ confidence level intervals resulting from a simultaneous fit to the θ_{13} and δ parameters. The generated values are $\theta_{13} = 5°, 8°, 10°$ and $\delta = \pm\, 90°$. The detector mass is 40 kton.

From the same figure it is possible to see that the sensitivity to δ does not worsen very much when θ_{13} becomes (moderately) smaller. Also, at 90% confidence level, a maximally violating CP phase $\delta = \pm\, 90°$ would be just distinguishable from a non CP violating phase $\delta = 0°$. So this experiment would offer a chance to observe CP violation only on a very lucky scenario.

Fig. 4.4 shows the result of the same fit for a very large water detector, such as the proposed UNO water Cerenkov, with a fiducial mass of 400 kton. Clearly, the prospects to observe CP violation are much improved.

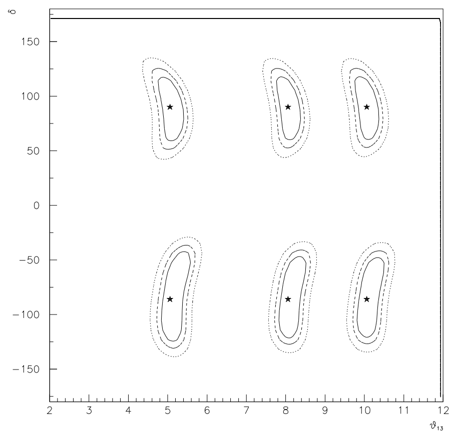

Figure 4.4. 1, 2 and 3 σ confidence level intervals resulting from a simultaneous fit to the θ_{13} and δ parameters. The generated values are $\theta_{13} = 5°$, $8°$, $10°$ and $\delta = \pm\, 90°$. The detector mass is 400 kton.

4.2 Correlations

The oscillation probability formulas couple the set of parameters θ_{12}, θ_{23}, θ_{13}, δ, Δm^2_{12} and Δm^2_{23}. In general, when one experiment tries to measure several parameters simultaneously, the uncertainty in each measured parameter will depend on the real (but only measured up to a certain degree) value of all the others. The parameters are correlated in the sense that an experiment is dominantly sensitive to a certain parameter combination. Weaker information on other parameter combinations allows typically to disentangle the parameters, but some correlations survive.

As an example, the measurement of a sum $a + b$ does not determine the individual values of a and b. Some more small information on other combinations of a and b produce potato-shaped regions aligned along $a + b = \text{const.}$

The value of a parameter and its uncertainty is merely the projection of the allowed region on the axis of that parameter, which will be bigger in general than the allowed region for the rest of the parameters equal to their central values (see fig. 4.5).

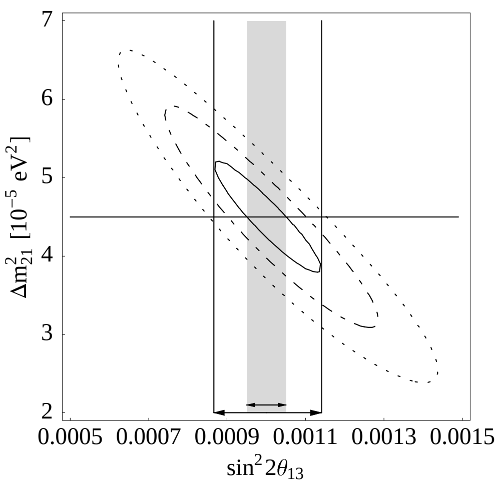

Figure 4.5. 1σ, 2σ and 3σ contours of the χ^2-function for a fit in $(\Delta m^2_{23}, \sin^2 2\theta_{13})$. The vertical lines indicate the 'extra' overall uncertainty in $\sin^2 2\theta_{13}$ coming from the correlation with Δm^2_{12} [HLW02].

4.3 Degeneracies

Degeneracies occur when two or more separated sets fit the same data (see for example fig. 4.6). Dealing with degeneracies, one might, for example, either quote separate uncertainties for completely separated parameter sets, or take the whole range covered by the degeneracies as the measurement uncertainty.

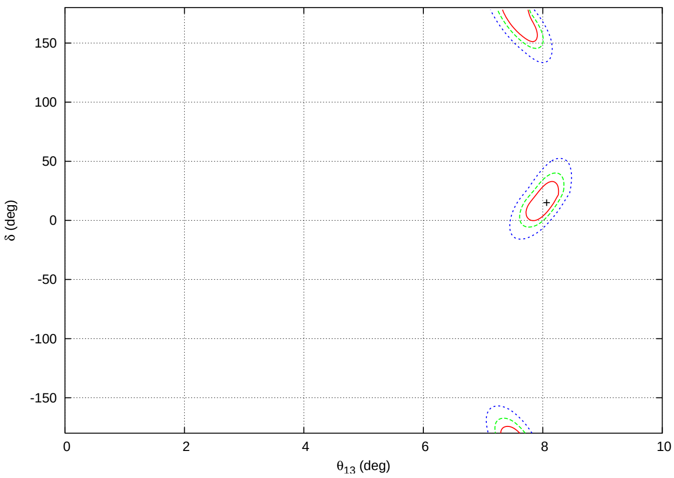

Figure 4.6. 1, 2 and 3 σ contours of the χ^2-function for a fit in (θ_{13}, δ). For the central values $\theta_{13} = 8°$ and $\delta = 15°$, a second solution appears, affecting our knowledge of δ.

4.4 Status at the Neutrino Factory

The best way to measure δ and θ_{13} is through the sub-leading transitions $\nu_e \leftrightsquigarrow \nu_\mu$ and $\bar{\nu}_e \leftrightsquigarrow \bar{\nu}_\mu$. They can be measured, for instance, at a Neutrino Factory by searching for wrong-sign muons while running in both polarities of the beam, i.e. μ^+ and μ^-.

The exact oscillation probabilities in matter when no mass difference is neglected can be approximated expanding the exact formulas to second order in the small parameters θ_{13}, Δ_{12}/Δ_{23}, Δ_{12}/A and $\Delta_{12} L$ (where $\Delta_{ij} \equiv \frac{\Delta m^2_{ij}}{2E}$):

$$\begin{aligned} P_{\nu_e \nu_\mu (\bar{\nu}_e \bar{\nu}_\mu)} &= s^2_{23} \sin^2 2\theta_{13} \left(\frac{\Delta_{13}}{B_\mp} \right)^2 \sin^2 \left(\frac{B_\mp L}{2} \right) \\ &+ c^2_{23} \sin^2 2\theta_{12} \left(\frac{\Delta_{12}}{A} \right)^2 \sin^2 \left(\frac{A L}{2} \right) \\ &+ J \frac{\Delta_{12}}{A} \frac{\Delta_{13}}{B_\mp} \sin \left(\frac{A L}{2} \right) \sin \left(\frac{B_\mp L}{2} \right) \cos \left(\pm \delta - \frac{\Delta_{13} L}{2} \right) \end{aligned} \tag{4.5}$$

where L is the baseline, $B_\mp \equiv |A \mp \Delta_{13}|$ and the matter parameter, A, is given in terms of the average electron number density, $n_e(L)$, as $A \equiv \sqrt{2}G_F n_e(L)$. J is defined as

$$J \equiv \cos\theta_{13}\sin 2\theta_{13}\sin 2\theta_{23}\sin 2\theta_{12} \tag{4.6}$$

In the limit $A \to 0$, this expression reduces to the simple formulas in vacuum

$$\begin{aligned} P_{\nu_e\nu_\mu(\bar{\nu}_e\bar{\nu}_\mu)} &= s_{23}^2\sin^2 2\theta_{13}\sin^2\left(\frac{\Delta_{13}L}{2}\right) \\ &+ c_{23}^2\sin^2 2\theta_{12}\sin^2\left(\frac{\Delta_{12}L}{2}\right) \\ &+ J\cos\left(\pm\delta - \frac{\Delta_{13}L}{2}\right)\frac{\Delta_{12}L}{2}\sin\left(\frac{\Delta_{13}L}{2}\right) \end{aligned} \tag{4.7}$$

The three terms in eq. (4.5) will be called the atmospheric, $P^{\rm atm}_{\nu(\bar{\nu})}$, solar, $P^{\rm sol}$, and interference term, $P^{\rm inter}_{\nu(\bar{\nu})}$.

An immediate result is

$$|P^{\rm inter}_{\nu(\bar{\nu})}| \leq P^{\rm atm}_{\nu(\bar{\nu})} + P^{\rm sol} \tag{4.8}$$

implying two very different regimes. When θ_{13} is relatively large or Δm_{12}^2 small, the probability is dominated by the atmospheric term, since $P^{\rm atm}_{\nu(\bar{\nu})} \gg P^{\rm sol}$. This situation is referred as the atmospheric regime. Conversely, when θ_{13} is very small or Δm_{12}^2 large, the solar term dominates $P^{\rm sol} \gg P^{\rm atm}_{\nu(\bar{\nu})}$. This is the solar regime. Fig. 4.7 illustrates the separation between the two regimes on the plane $(\Delta m_{12}^2, \theta_{13})$ for neutrinos and antineutrinos, as derived from eq. (4.5). The area to the right (left) of the curves corresponds to the atmospheric (solar) regime.

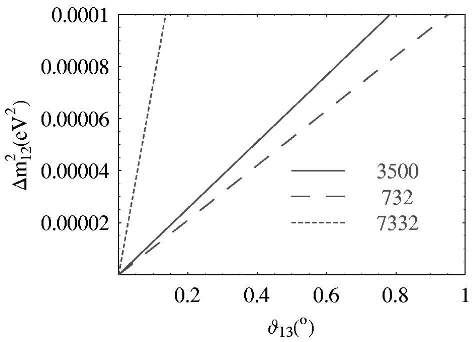

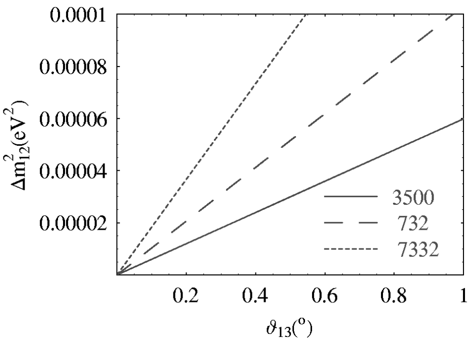

Figure 4.7. Contours $P^{\rm atm}_{\nu} = P^{\rm sol}$ (left) and $P^{\rm atm}_{\bar{\nu}} = P^{\rm sol}$ (right) on the plane (θ_{13}, δ), for three reference baselines.

4.4.1 Correlation Between δ and θ_{13}

The oscillation probabilities of eq. (4.5), whose measurement δ could be extracted from, depend as well on θ_{23}, Δm_{23}^2, θ_{12}, Δm_{12}^2, A and θ_{13}. Uncertainties in the latter quantities can then hide the effect of CP violation. Although the first five of these parameters are expected to be well known at the time of the neutrino factory with a good accuracy, θ_{13} might well remain unknown. It is essential then to understand whether the correlation between θ_{13} and δ can be resolved in such a way that CP violation is measurable.

For a single beam polarity and a fixed neutrino energy and baseline, the expansion of eq. (4.5) to second order in θ_{13} leads to

$$P_{\nu_e\nu_\mu(\bar{\nu}_e\bar{\nu}_\mu)} = X_\pm\,\theta_{13}^2 + Y_\pm\,\theta_{13}\cos\left(\pm\,\delta - \frac{\Delta_{13}\,L}{2}\right) + P^{\mathrm{sol}} \tag{4.9}$$

with obvious assignations for the coefficients X and Y, which are independent of θ_{13} and δ. Note that the solar term P^{sol} is the same for neutrinos and antineutrinos.

As eq. (4.9) is a function of 2 parameters, θ_{13} and δ, there is a continuum of pairs of values (θ_{13}, δ) that give the same probability as the real values $(\bar{\theta}_{13}, \bar{\delta}\,)$.

This requirement can be solved for θ_{13} as a function of δ:

$$\begin{aligned}\theta_{13} &= -\frac{Y_+}{2\,X_+}\cos\left(\delta - \frac{\Delta_{13}\,L}{2}\right)\\ &\pm \sqrt{\left(\frac{Y_+}{2\,X_+}\cos\left(\delta - \frac{\Delta_{13}\,L}{2}\right)\right)^2 + \frac{1}{X^+}\left(P_{\nu_e\nu_\mu}(\bar{\theta}_{13}, \bar{\delta}\,) - P^{\mathrm{sol}}\right)}\end{aligned} \tag{4.10}$$

Eq. (4.10) is a curve of equal probability on the plane (θ_{13}, δ), which for most of the parameter space spans the whole range of δ. It follows that, at any baseline, it is not possible to determine δ with the measurement of wrong-sign muons at a fixed neutrino energy with a single beam polarity.

The analogous case for antineutrinos results in a different equal probability curve, with the following substitutions in eq. (4.10): $\delta \to -\,\delta, X_+(Y_+) \to X_-(Y_-)$.

When finite uncertainties are taken into account, the shapes of the χ^2-allowed regions are two broad bands with close paths. The intersection of these two regions will result in one region where θ_{13} and δ are correlated.

4.4.2 Intrinsic Degeneracies

If both the neutrino and antineutrino oscillation probabilities have been measured, for a fixed (anti)neutrino energy and baseline, the two equal-probability curves may intersect at values of (θ_{13}, δ) different from $(\bar{\theta}_{13}, \bar{\delta}\,)$. This condition implies equating eq. (4.10) to the corresponding one for antineutrinos and solving for δ, for small $\theta_{13} > 0$. The resulting equation is rather complicated, but simplifies considerably in the atmospheric and extreme solar regimes.

4.4.2.1 Atmospheric Regime

In this regime it is safe to keep terms only up to first order in $Y_+/X_+(Y_-/X_-)$ in eq. (4.10). As a result only the solution of eq. (4.10) with $+$ sign in front of the square root is acceptable since $\theta_{13} > 0$. Eq. (4.10) simplifies to

$$\theta_{13} = \bar{\theta}_{13} - \frac{Y_+}{2\,X_+}\left[\cos\left(\delta - \frac{\Delta_{13}\,L}{2}\right) - \cos\left(\bar{\delta} - \frac{\Delta_{13}\,L}{2}\right)\right] \tag{4.11}$$

The equation for δ is then obtained from equating eq. (4.11) for neutrinos to that for antineutrinos. The problem amounts to finding the roots of a function of δ which is continuous and periodic. Since it must have at least one root at $\delta = \bar{\delta}$, by periodicity there must be at least a second root in the range $-180° < \delta < 180°$.

The second solution for δ in this approximation is:

$$\begin{aligned} \sin\delta - \sin\bar{\delta} &= -2\,\frac{\sin\bar{\delta} - z\cos\bar{\delta}}{1+z^2} \\ \cos\delta - \cos\bar{\delta} &= 2\,z\,\frac{\sin\bar{\delta} - z\cos\bar{\delta}}{1+z^2} \end{aligned} \tag{4.12}$$

where $z \equiv \frac{C_+}{C_-}\tan\frac{\Delta_{13}L}{2}$ and $C_\pm \equiv \frac{1}{2}\left(\frac{Y_+}{X_+} \pm \frac{Y_-}{X_-}\right)$. The corresponding value of θ_{13} is:

$$\theta_{13} = \bar{\theta}_{13} - \frac{1}{2}\,\frac{\sin\bar{\delta} - z\cos\bar{\delta}}{1+z^2}\,\frac{C_+^2 - C_-^2}{C_-}\sin\frac{\Delta_{13}L}{2} \tag{4.13}$$

Only for the value of $\bar{\delta}$ satisfying

$$\tan\bar{\delta} = z \tag{4.14}$$

do the two solutions degenerate into one. Except for this particular point, there are two degenerate solutions with the penalty that, in an unfortunate value of $\bar{\delta}$, one solution may correspond to CP-conservation and its image not.

In vacuum this is not the case. Eq. (4.12) in the vacuum limit: $C_- \to 0$ or $z \to \infty$, gives $\delta = \pi - \bar{\delta}$ so that only for $\bar{\delta} = \pm\pi/2$ there is no degeneracy. Then the two solutions either break or conserve CP.

In fig. 4.8 it is shown the value of δ as a function of $\bar{\delta}$ for $\theta_{13} = 8°$ and for three reference baselines together with the vacuum result. The difference between δ and $\bar{\delta}$ is maximal close to $\bar{\delta} = 0°, 180°$.

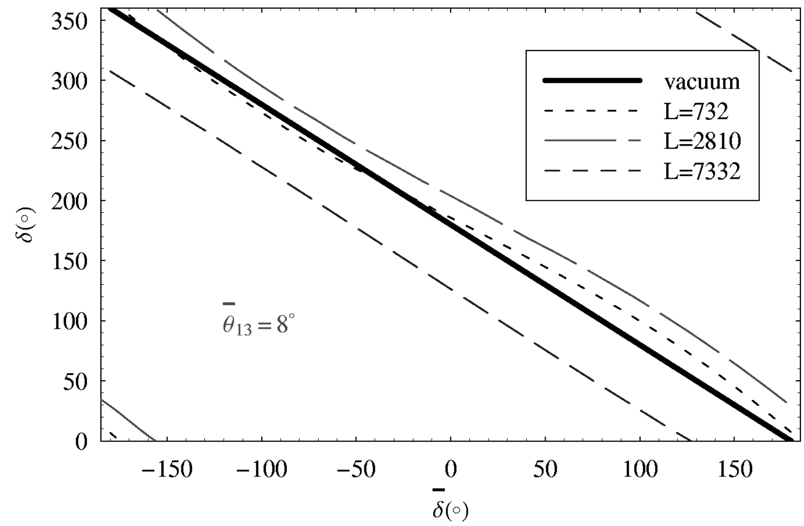

Figure 4.8. Degenerate value of δ as a function of true value $\bar{\delta}$, for $\bar{\theta}_{13} = 8°$ and three different baselines. The vacuum result $\delta = \pi - \bar{\delta}$ is also shown.

It is interesting to consider the different impact of these degenerate solutions at different baselines. At short baselines, the oscillation probabilities for neutrinos and antineutrinos are approximately the same for two reasons: 1) the relative size of the $\sin\delta$ versus $\cos\delta$ term in eq. (4.5) is $\tan(\Delta_{13}L/2) \ll 1$, 2) matter effects are irrelevant with the solutions approaching the vacuum case. Indeed, the expansion of eq. (4.11) for $\Delta_{13}L/2 \ll 1$ simplifies to

$$\theta_{13} \simeq \bar{\theta}_{13} - \frac{Y_+}{2X_+}(\cos\delta - \cos\bar{\delta}\,) \tag{4.15}$$

The same equation holds for antineutrinos, since $X_+(Y_+) = X_-(Y_-)$ in this approximation. The two equations have collapsed into one, and consequently one expects to find a continuum curve of solutions (θ_{13}, δ) of the approximate form given by eq. (4.15). As the baseline increases the probabilities for neutrino and antineutrino oscillations start to differ, not only due to the term in $\sin\delta$, but also because of the matter effects. A shift in δ cannot in general be then compensated in the neutrino and antineutrino probabilities by a common shift of θ_{13}, and only the two-fold degeneracy discussed above survives.

4.4.2.2 Solar Regime

In this regime the second term in eq. (4.5) dominates, although the first term cannot be neglected in the analysis of degenerate solutions even for very small values of $\bar{\theta}_{13}$. The reason is that it exists, at fixed neutrino energy and baseline, a pair of values (θ_{13}, δ) at which the first and third terms in eq. (4.5) exactly compensate both for neutrinos and antineutrinos, in such a way that they are indistinguishable from the situation with $\bar{\theta}_{13} = 0$ and any $\bar{\delta}$. It is easy to find these values by setting $\bar{\theta}_{13} = 0$ in eq. (4.10) and in the equivalent equation for antineutrinos. δ is the solution of:

$$\tan\delta = -\frac{1}{z} \tag{4.16}$$

and the corresponding θ_{13} is:

$$\theta_{13} = -\frac{Y_+}{X_+}\cos\left(\delta - \frac{\Delta_{13}L}{2}\right) \tag{4.17}$$

Taking as an example $\Delta m^2_{23} = 3 \times 10^{-3}$ eV^2, $L = 2810$ km and $E_\nu = 0.3\,E_\mu$, $E_\mu = 50$ GeV, this point is:

$$\theta_{13} \sim 1.5^\circ, \quad \delta \sim -165^\circ \tag{4.18}$$

Alike to the pattern in the atmospheric regime, this degeneracy occurs only at fixed neutrino energy and baseline.

In summary, even with the information from both beam polarities, there are in general two equally probable solutions, at fixed neutrinos energy and baseline, for the parameters θ_{13} and δ.

4.4.3 Simultaneous Determination of δ and θ_{13}

The observables used to determine δ and θ_{13} simultaneously are the number of wrong-sign muons in five bins of energy for both beam polarities:

$$N_{i,\pm} \tag{4.19}$$

where i labels the energy bin, and $\pm$ the sign of the decaying muons. These numbers are given by:

$$N_{i,\pm} = \int_{E_i}^{E_i+\Delta E} \Phi_{\nu(\bar{\nu})}(E_\nu, L)\sigma_{\nu(\bar{\nu})}(E_\nu)P_{\nu(\bar{\nu})}(E_\nu, L, \theta_{13}, \delta, \alpha) \tag{4.20}$$

where α is the set of remaining oscillation parameters: $\theta_{23}, \theta_{12}, \Delta m^2_{23}, \Delta m^2_{12}$ and the matter parameter A, which are taken as known. $\Phi_{\nu(\bar{\nu})}$ denote the neutrino fluxes and $\sigma_{\nu(\bar{\nu})}$ the deep inelastic scattering cross sections.

With these observables, the χ^2 fits of the parameters δ and θ_{13} are obtained from:

$$\chi^2 = \sum_{i,j} \sum_{p,p'} (n_{i,p} - N_{i,p}) C^{-1}_{i,p;j,p'} (n_{j,p'} - N_{j,p'}) \tag{4.21}$$

where C is the $2N_{bin} \times 2N_{bin}$ covariance matrix. $n_{i,j}$ are the simulated "data" obtained from a Gaussian or Poisson smearing including backgrounds and efficiencies. For a correct analysis that takes the correlations into account, the form of the matrix C is:

$$C_{i,p;j,p'} \equiv \delta_{ij} \delta_{pp'} (\delta n_{i,p})^2 + \sum_\alpha \frac{\partial N_{i,p}}{\partial \alpha} \frac{\partial N_{j,p'}}{\partial \alpha} \sigma^2(\alpha) \tag{4.22}$$

where $\sigma(\alpha)$ is the 1σ uncertainty on the parameter α.

4.4.3.1 Atmospheric Regime

In figs. 4.9 we can see the results of the fits including efficiencies and backgrounds for $L = 2810$ km for central values of $\bar{\delta} = -90°, 0°, 90°, 180°$ and for $\bar{\theta}_{13} = 2°$ (left) and $\bar{\theta}_{13} = 8°$ (right). The energy dependence of the signals is not significant enough (with this setup) to resolve the expected two-fold degeneracy. The second solution is clearly seen for the central value of $\bar{\delta} = 0°$ as an isolated island. For the central values of $\bar{\delta} = -90°$ and $\bar{\delta} = 90°$, the degeneracy is responsible for the rather large contours which encompass the two solutions. As $\bar{\theta}_{13}$ diminishes the fake solution for $\bar{\delta} = 90°$ moves towards $\delta = 180°$, as expected because, in the solar regime, the vacuum fake image lies at $\delta = 180°$.

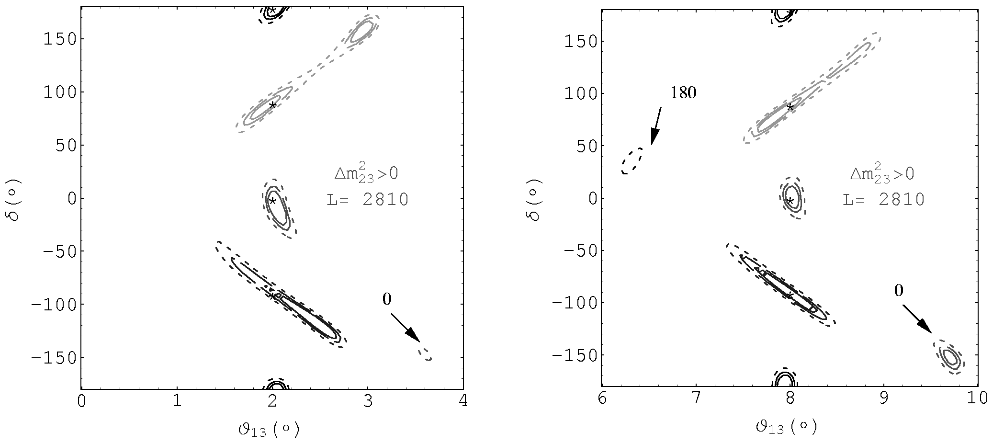

Figure 4.9. Simultaneous fits of δ and θ_{13} at $L = 2810$ km for different central values (indicated by the stars) of $\bar{\delta} = -90°, 0°, 90°, 180°$ and $\bar{\theta}_{13} = 2°$ (left), $8°$ (right). The value of $\bar{\delta}$ for the degenerate solutions is also indicated.

Figs. 4.10 show the fits for $\bar{\theta}_{13} = 8°$ at $L = 732$ km and 7332 km. In the former, the expected continuous line of solutions of the form given by eq. (4.15) is clearly seen. The measurement of δ is thus impossible at this baseline if θ_{13} is unknown. In the longer baseline, the sensitivity to δ is similarly lost but for a different reason: the CP-signal is fading away (indeed the underlying degenerate solutions become much closer in θ_{13}) and statistics is diminishing.

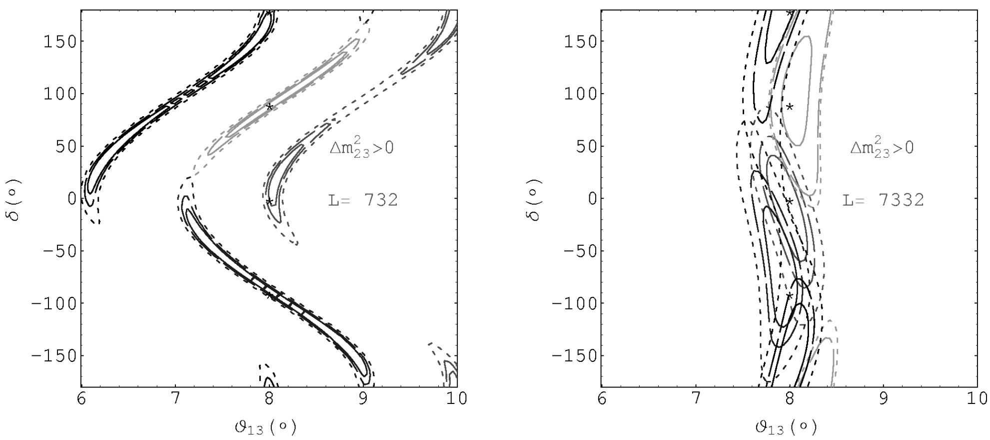

Figure 4.10. Simultaneous fits of δ and θ_{13} at $L = 732$ km (left) and $L = 7332$ km (right) for different central values of $\bar{\delta} = -90°$, $0°$, $90°$, $180°$ and $\bar{\theta}_{13} = 8°$.

4.4.3.2 Solar Regime

In fig. 4.11 are shown the fits including efficiencies and backgrounds for $L = 2810$ km for central values of $\bar{\delta} = -90°$, $0°$, $90°$, $180°$ and $\bar{\theta}_{13} = 0.3°$ (left) and $\bar{\theta}_{13} = 0.6°$ (right). On the left, the images of the four points chosen appear grouped at the right/lower side of the figure. These are the solutions that mimic $\theta_{13} = 0$ as predicted from (4.17). The comparison of these figures with fig. 4.9 illustrates the expected decrease of the sensitivity to CP violation for very small θ_{13}.

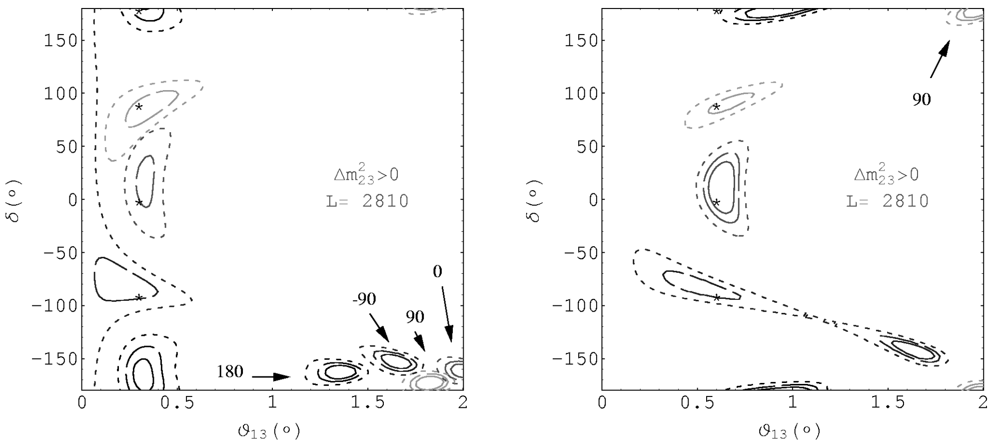

Figure 4.11. Simultaneous fits of δ and θ_{13} at $L = 2810$ km for different central values of $\bar{\delta} = -90°$, $0°$, $90°$, $180°$ and $\bar{\theta}_{13} = 0.3°$ (left), $0.6°$ (right). The value of $\bar{\delta}$ for the degenerate solutions is indicated.

4.5 Combinations

As explained in section 4.4.2, there exists generically, at a given (anti)neutrino energy and fixed baseline, a second value of the set (θ_{13}, δ) that gives the same oscillation probabilities for neutrinos and antineutrinos as the true value that appears in nature. That's what we call *intrinsic degeneracies*.

It has also been pointed out [BMW02a] that other fake solutions might appear from unresolved degeneracies in two other oscillation parameters:

- the sign of Δm^2_{23}
- θ_{23}, upon the exchange $\theta_{23} \leftrightarrow \pi/2 - \theta_{23}$ for $\theta_{23} \neq \pi/4$

It is not expected that these degeneracies will be resolved before the time of the Superbeam or Neutrino Factory operation. However, the subleading transitions $\nu_e \leftrightsquigarrow \nu_\mu$, from which the parameters θ_{13} and δ can be measured, are sensitive to these discrete ambiguities. A complete analysis of the sensitivity to the set (θ_{13}, δ) should therefore assume that sign(Δm^2_{23}) can be either positive or negative, and that θ_{23} is either bigger or smaller than $\pi/4$. If a wrong choice of these possibilities cannot fit the data, the ambiguities will be resolved, else they will generically give rise to new fake solutions for the parameters θ_{13} and δ.

There are different strategies to eliminate some of the fake solutions. It is possible to make a combination of different baselines [BCGGC+01], an improved experimental technique allowing the measurement of the neutrino energy with good precision [FHL01], the supplementary detection of $\nu_e \rightsquigarrow \nu_\tau$ channels [DMM02] and a cluster of detectors at a superbeam facility located at different off-axis angles, so as to have different $\langle E \rangle$ [BMW02b].

All the strategies are based in the inclusion of new information into the analysis, combining the 'standard Neutrino Factory dataset' with some other dataset, be it different baselines, energy resolution, new channels or modifications of the flux. We will present what is one of the most promising combinations: a Neutrino Factory with a Superbeam.

4.5.1 Neutrino Factory with Superbeam

The development of a Neutrino Factory requires, by design, the essentials of a Superbeam facility as an intermediate step. Although the ultimate precision and discovery goals in neutrino oscillation physics may only be attained with a neutrino factory from muon storage rings, those "for free" superbeam results can already lead to significant progress in central physics issues, as is the case of the degeneracies.

Superbeams and the Neutrino Factory are not alternative options, but successive steps. In this perspective, the analysis strategy is to contemplate the combination of their expected physics results, which would improve the measurements of the Neutrino Factory and may resolve the problem of degeneracies.

For concreteness, the results of the next sections will consider the following experimental setup: 1) A Neutrino Factory with a parent $\mu^\pm$ energy of 50 GeV and two reference baselines at 732 and 2810 km, and 2) A Superbeam with the proposed CERN SPL accelerator, with an average energy of $\langle E \rangle = 0.25$ GeV and a baseline of 130 km (CERN-Fréjus).

4.5.2 Resolution of Intrinsic Degeneracies

At a fixed neutrino energy and baseline, there are degenerate solutions in the (θ_{13}, δ) plane for fixed values of the oscillation probabilities $\nu_e(\bar{\nu}_e) \rightsquigarrow \nu_\mu(\bar{\nu}_\mu)$. If ($\theta_{13}$, δ) are the values chosen by nature, the conditions

$$\begin{aligned} P_{\nu_e\nu_\mu}(\theta'_{13}, \delta') &= P_{\nu_e\nu_\mu}(\theta_{13}, \delta) \\ P_{\bar{\nu}_e\bar{\nu}_\mu}(\theta'_{13}, \delta') &= P_{\bar{\nu}_e\bar{\nu}_\mu}(\theta_{13}, \delta) \end{aligned} \tag{4.23}$$

can be generically satisfied by another set (θ'_{13}, δ'). Using the approximate formulas of eq. (4.7), it is easy to find the expression for these *intrinsic* degeneracies deep in the atmospheric and solar regimes, as shown in section 4.4.2.

For θ_{13} sufficiently large and in the vacuum approximation, apart from the true solution, $\delta' = \delta$ and $\theta'_{13} = \theta_{13}$, there is a fake one at

$$\begin{aligned} \delta' &\simeq \pi - \delta \\ \theta'_{13} &\simeq \theta_{13} + \cos\delta \sin 2\,\theta_{12} \frac{\Delta m^2_{12}\,L}{4\,E} \cot\theta_{23} \cot\frac{\Delta m^2_{23}\,L}{4\,E} \end{aligned} \tag{4.24}$$

Note that for values $\delta = -\,90°, 90°$, the two solutions degenerate into one. Typically $\cot\frac{\Delta m^2_{23}\,L}{4\,E}$ has on average opposite signs for the proposed superbeam and Neutrino Factory setups, for $\Delta m^2_{23} = 3\times 10^{-3}\mathrm{eV}^2$:

	$\langle E\rangle$(GeV)	L(km)	$\cot\frac{\Delta m^2_{23}\,L}{4\,E}$
SPL	0.25	130	$-\,0.43$
T2K off-axis	0.7	295	$-\,0.03$
NuFact@732	30	732	$+\,10.7$
NuFact@2810	30	2810	$+\,2.68$
β-beam	0.35	130	$+\,0.17$

When $\theta_{13} \to 0$ and in the vacuum approximation, the intrinsic degeneracy is independent of δ:

$$\begin{cases} \text{if } \cot\left(\dfrac{\Delta m^2_{23}\,L}{4\,E}\right) > 0 \text{ then } \delta' \simeq \pi \\ \text{if } \cot\left(\dfrac{\Delta m^2_{23}\,L}{4\,E}\right) < 0 \text{ then } \delta' \simeq 0 \end{cases}$$

$$\theta'_{13} \simeq \sin 2\theta_{12} \frac{\Delta m^2_{12}\,L}{4\,E} \left|\cot\theta_{23} \cot\left(\frac{\Delta m^2_{23} L}{4E}\right)\right| \tag{4.25}$$

This solution is named $\theta_{13} = 0$-mimicking solution and occurs because there is a value of θ'_{13} for which there is an exact cancellation of the atmospheric and interference terms in both the neutrino and antineutrino probabilities simultaneously, with $\sin\delta' = 0$.

Figure 4.12 shows the results of measuring $(\theta_{13},\ \delta)$ at the SPL-superbeam facility, for $\theta_{13} = 8°$ and the central values of $\delta = -\ 180°,\ -\ 90°,\ 90°,\ 180°$. The intrinsic degeneracies clearly appear and are well described by eqs. (4.24).

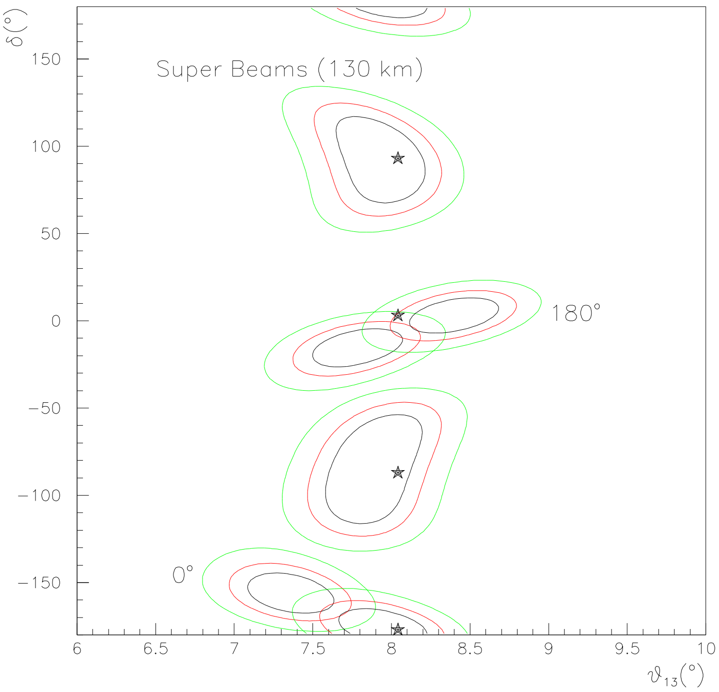

Figure 4.12. Fits to the given true solutions and their intrinsic degenerate solutions at a Superbeam facility. The 68.5%, 90% and 99% contours are depicted, for four central values of $\delta = -90°, 0°, 90°, 180°$ and $\theta_{13} = 8°$.

The analysis is based on the total number of electron/positron events, so it is not assumed that the neutrino energy can be reconstructed.

A comparison of the Neutrino Factory and SPL-superbeam fits shows that the displacement of the fake solution with respect to the true one is opposite for the two facilities.

In order to understand the intermediate region between the solar and atmospheric regimes, as well as the influence of matter effects, the possible physical solutions to eqs. (4.23) can be computed numerically, using the approximate formulas for the probabilities including matter effects. In what follows, L and E are fixed to the average values for the different facilities. The results for the shift $\theta'_{13} - \theta_{13}$ and δ' are shown in fig. 4.13 as a function of θ_{13}, for two values of $\delta = 0°$, $90°$ and for the different experimental setups. In the whole range of parameters there are two solutions, as expected by periodicity in δ, since one solution is warranted: the true one.

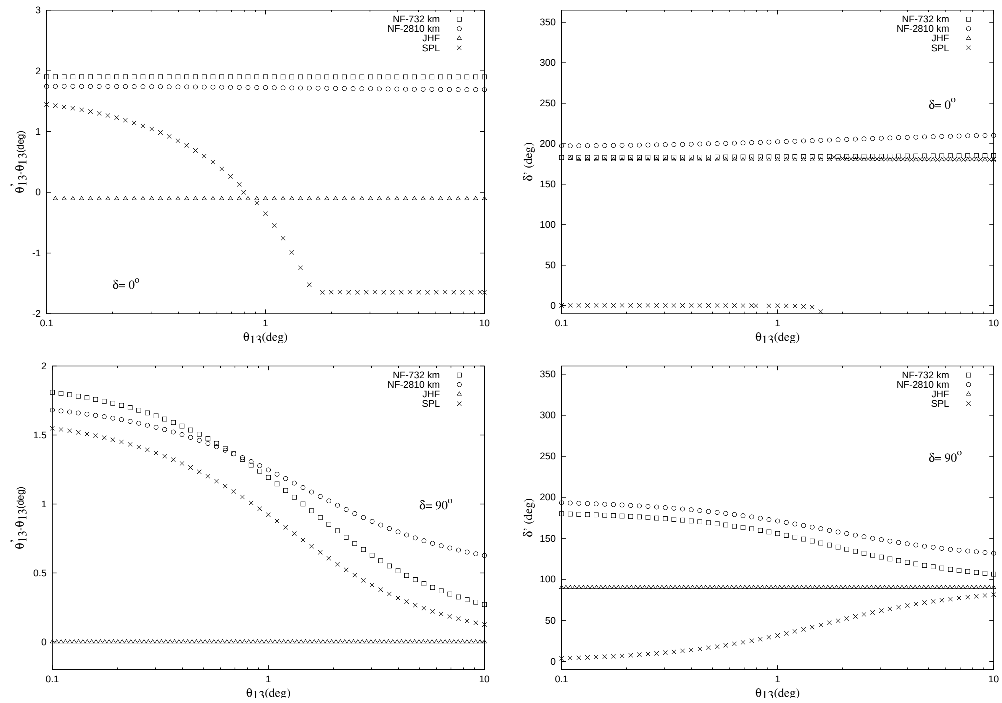

Figure 4.13. $\theta'_{13} - \theta_{13}$ (left) an δ' (right) versus θ_{13}, for the intrinsic fake solution, for fixed values of $\delta = 0°$ (up) and $\delta = 90°$ (down).

The most important point to note in eqs. (4.24) and (4.25) and in figs. 4.13 is that the position (measured in $\theta'_{13} - \theta_{13}$ or δ') of the degenerate solution is very different in the neutrino factory, the SPL-superbeam and JHF setups. As a result, it is expected that any combination of the results of two of these three facilities could in principle exclude the fake solutions. The $\theta'_{13} - \theta_{13}$ of the fake solution depends strongly on the baseline and the neutrino energy through the ratio L/E, so the combination of the results of two experiments with a different value for this ratio should be able to resolve these degeneracies, within their range of sensitivity. Even more important is that, for small θ_{13}, δ' may differ by 180° if the two facilities have opposite sign for cot $\frac{\Delta m^2_{23}\, L}{4\, E}$. For the Neutrino Factory setups, this sign is clearly positive, since the measurement of CP violation requires, because of the large matter effects, a baseline considerably shorter than that corresponding to the maximum of the atmospheric oscillation (in vacuum), where the cotangent changes sign. In the superbeams scenario, on the other hand, because of the smaller $\langle E \rangle$, matter effects are small at the maximum of the atmospheric oscillation, which then becomes the optimal baseline for CP violation studies. It is then not very difficult to ensure that cot $\frac{\Delta m^2_{23} L}{4E}$ is dominantly negative in this case, which results in an optimal complementarity of the two facilities in resolving degeneracies.

4.5.2.1 Effect of Δm^2_{23}

Clearly the position of the fake solution is very sensitive to the atmospheric $|\Delta m^2_{23}|$. In matter we expect a milder dependence. especially if matter effects become dominant. In fig. 4.14 one can see the separation in θ_{13} of the intrinsic degenerate solution at $\delta = 0°$ in the atmospheric regime as a function of $|\Delta m^2_{23}|$. Although in general the separation becomes smaller for smaller $|\Delta m^2_{23}|$, it is sizable in the whole allowed range. The relative difference between the results for the neutrino factory and the SPL superbeam option is always largest, although the differences between the two superbeams and that between the neutrino factory and JHF are also very large. Note also that the sign of $\theta'_{13} - \theta_{13}$, which is related to that of cot $\frac{\Delta m^2_{23} L}{4E}$, is positive in all the domain for the neutrino factory baselines and negative in most of the domain for SPL-superbeam scenario, which implies that the difference in δ' between the two facilities is 180° for small θ_{13}. For JHF, it is negative only for $|\Delta m^2_{23}| \geq 3 \times 10^{-3}\mathrm{eV}^2$.

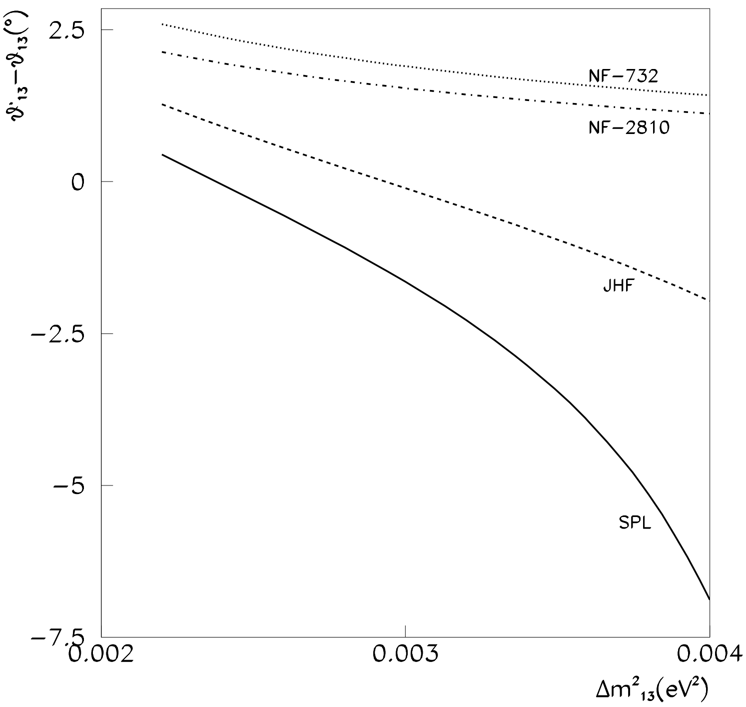

Figure 4.14. $\theta'_{13} - \theta_{13}$ versus $|\Delta m^2_{23}|$ for the intrinsic fake solution in the atmospheric regime and $\delta = 0°$.

Concerning the dependence on the solar parameters, it enters only through the combination $\sin^2 2\,\theta_{12}\,\frac{\Delta m^2_{12} L}{4\,E}$. In general $\theta'_{13} - \theta_{13}$ is linear in this quantity, so degenerate solutions become closer with smaller Δm^2_{12} and also closer to the true solution. Note however that δ' in the solar regime does not depend on the solar parameters and that it differs by 180° in the two facilities, and this separation will remain when Δm^2_{12} is lowered.

4.5.2.2 Effect of Δm^2_{12}

Turning to the variation of the solar parameters while in the atmospheric regime, we will see that, if the two facilities that are combined have opposite sign(cot $\frac{\Delta m^2_{23} L}{4\,E}$), the effect of lowering Δm^2_{12} is not dramatic either in the resolution of degeneracies. The statistical error on the measurement of θ_{13} and δ is mainly independent of the solar parameters (it is dominated by the atmospheric term), which means that at some point when Δm^2_{12} is lowered, the degenerate solutions of the two facilities will merge, since the error remains constant while the separation of the solutions gets smaller. However, because of the opposite sign of $\theta'_{13} - \theta_{13}$, the solutions of the two facilities will merge only when they merge with the true solution in θ_{13}. If this happens, it would therefore not bias the measurement of θ_{13} and δ.

The combination of a Neutrino Factory with the SPL-superbeam facility, for the optimal Neutrino Factory baseline $L = 2810$ km, is sufficient to get rid of all the fake solutions, as shown in the result of a complete numerical analysis in figs. 4.15 (left). It is to note that indeed the disappearance of the fake solutions takes place even in the solar regime.

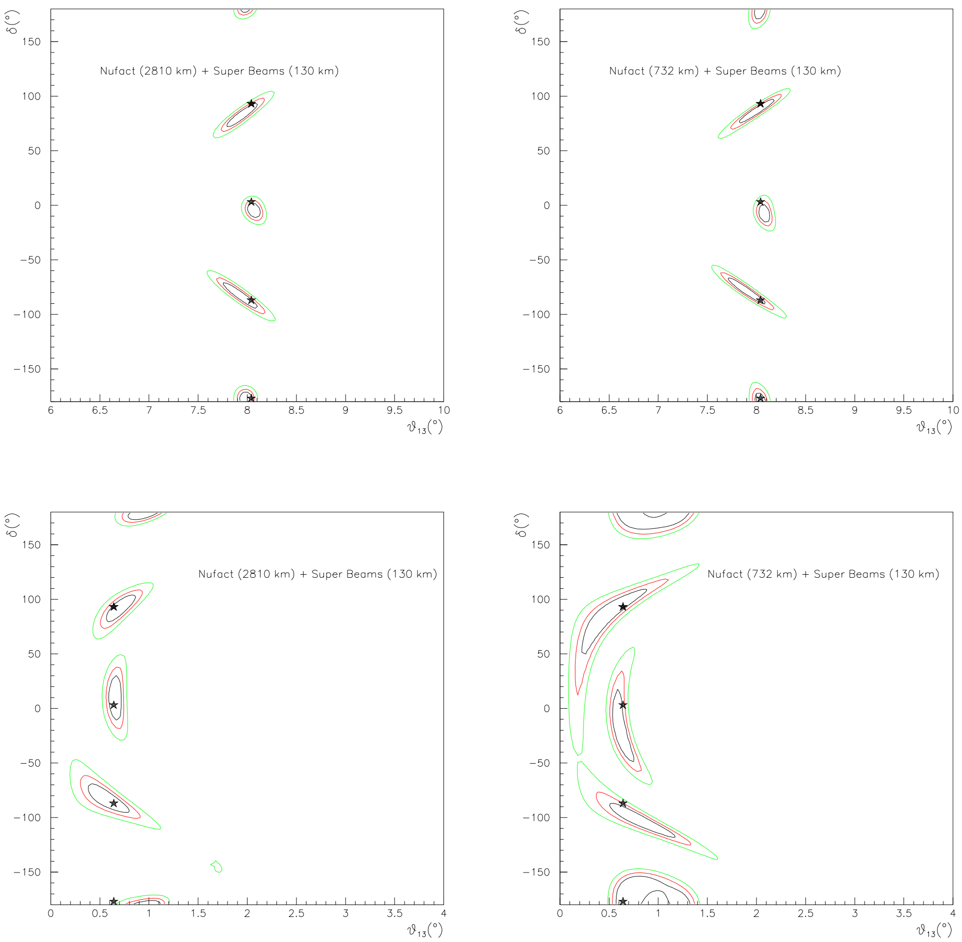

Figure 4.15. Fits combining the results from the SPL-Superbeam facility and a Neutrino Factory baseline at $L = 2810$ km (left) or $L = 732$ km (right). The true values illustrated correspond to $\delta = -90°, 0°, 90°, 180°$ and $\theta_{13} = 8°$ (top) or $\theta_{13} = 0.6°$ (bottom). The fake intrinsic solutions completely disappear in the combinations.

There are some differences when the combination of the SPL-Superbeam is done with a shorter Neutrino Factory baseline of $L = 732$ km. The degenerate solution is not so relevant to this neutrino factory baseline when considered alone, because there the sensitivity to CP violation is so poor that there exists a continuum of almost degenerate solutions, which makes the determination of δ impossible with the wrong-sign muon signals. The combination of the results from this neutrino factory baseline with those from the SPL-superbeam facility is summarized in figs. 4.15 (right). Not only do the fake solutions corresponding to the intrinsic degeneracies in the superbeam disappear, but the accuracy in the determination of the true solution becomes competitive with that obtained in the combination with the optimal baseline for large values of θ_{13}. At small values of θ_{13} the latter still gives better results, as expected.

4.5.3 sign(Δm^2_{23}) Degeneracy

To see the effect of sign(Δm^2_{23}) one can try to perform the analysis assuming its value is the opposite of the real one. The oscillation probability with the sign of Δm^2_{23} reversed will be called $P'_{\nu_e\nu_\mu(\bar{\nu}_e\bar{\nu}_\mu)}(\theta_{13},\delta)$. New fake solutions (θ'_{13},δ'), at fixed E_ν and L, will appear if the equations

$$\begin{aligned} P'_{\nu_e\nu_\mu}(\theta'_{13},\delta') &= P_{\nu_e\nu_\mu}(\theta_{13},\delta) \\ P'_{\bar{\nu}_e\bar{\nu}_\mu}(\theta'_{13},\delta') &= P_{\bar{\nu}_e\bar{\nu}_\mu}(\theta_{13},\delta) \end{aligned} \tag{4.26}$$

have solutions in the allowed physical range.

It turns out that there are generically two fake solutions to eqs. (4.26). It is very easy to find them in the vacuum approximation, as the mirror of the two solutions (true and fake) obtained in the analysis of the intrinsic degeneracies. It can be seen in eq. (4.7) that a change in the sign of Δm^2_{23} can be traded in vacuum by the substitution $\delta \to \pi - \delta$, implying then for eqs. (4.26)

$$P'_{\nu_e\nu_\mu(\bar{\nu}_e\bar{\nu}_\mu)}(\theta'_{13},\delta') \simeq P_{\nu_e\nu_\mu(\bar{\nu}_e\bar{\nu}_\mu)}(\theta'_{13},\pi-\delta') \tag{4.27}$$

in the vacuum approximation. Consequently, the solutions in vacuum can be obtained from those present for the intrinsic case, upon the substitution $\delta' \to \pi - \delta'$. One of them mirrors the true (nature) solution and will be called below solution I, given in vacuum by

$$\begin{aligned} \delta' &\simeq \pi - \delta \\ \theta'_{13} &\simeq \theta_{13} \end{aligned}$$

The fact that it is approximately E and L-independent suggests that it will be hard to eliminate it by exploiting the L, E dependence of different facilities, as indeed is confirmed by the fits below. Fortunately, this fake solution does not interfere significantly with the determination of θ_{13} or CP-violation (i. e. $\sin\delta$).

The second fake sign solution, which will be called solution II, can be read in vacuum from eqs. (4.24) and (4.25), upon the mentioned $\delta' \to \pi - \delta'$ exchange. It is strongly L- and E- dependent. Both solutions I and II can be seen in the numerical analysis for the SPL superbeam in fig. 4.16 (left), for $\theta_{13} = 8°$ and positive $\mathrm{sign}(\Delta m^2_{23})$.

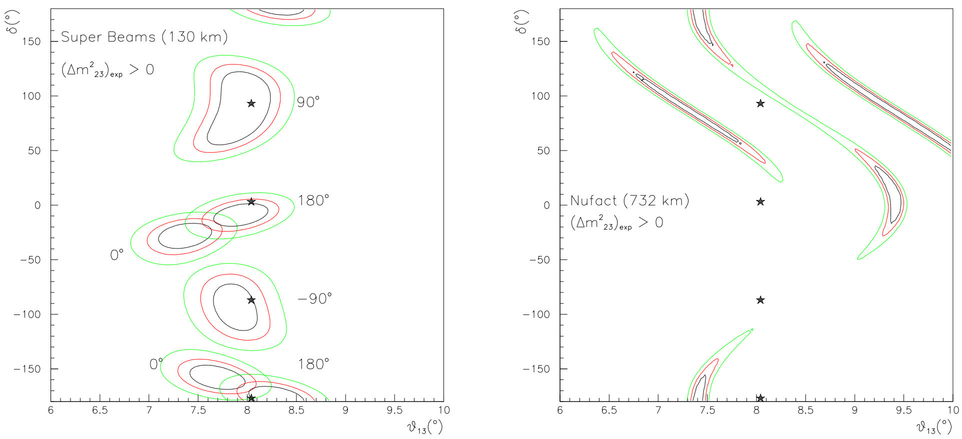

Figure 4.16. Fits for central values $\theta_{13} = 8°$ and $\delta = -90°, 0°, 90°, 180°$ for the SPL-Superbeam (left) and Neutrino Factory at $L = 732$ km (right). The real sign for Δm^2_{23} is assumed to be positive, while the fits are performed with the opposite sign. All fake solutions disappear when the two sets of data are combined.

Matter effects are obviously very important in resolving fake sign solutions: the task should thus be easier at large θ_{13} and large enough Neutrino Factory baselines, where matter effects are largest. In fact it is easy to prove that no solutions can remain for large enough θ_{13}. This can be seen in figs. 4.17, which show the fake sign solutions as they result from solving numerically eqs. (4.26) (using the approximate probabilities with matter effects included) for the different experiments. For small θ_{13} the two solutions I and II exist in all cases, while for large θ_{13} they degenerate and disappear because of matter effects. Nevertheless even if no fake solution exists, there might be approximate ones that will show up in a measurement with finite errors.

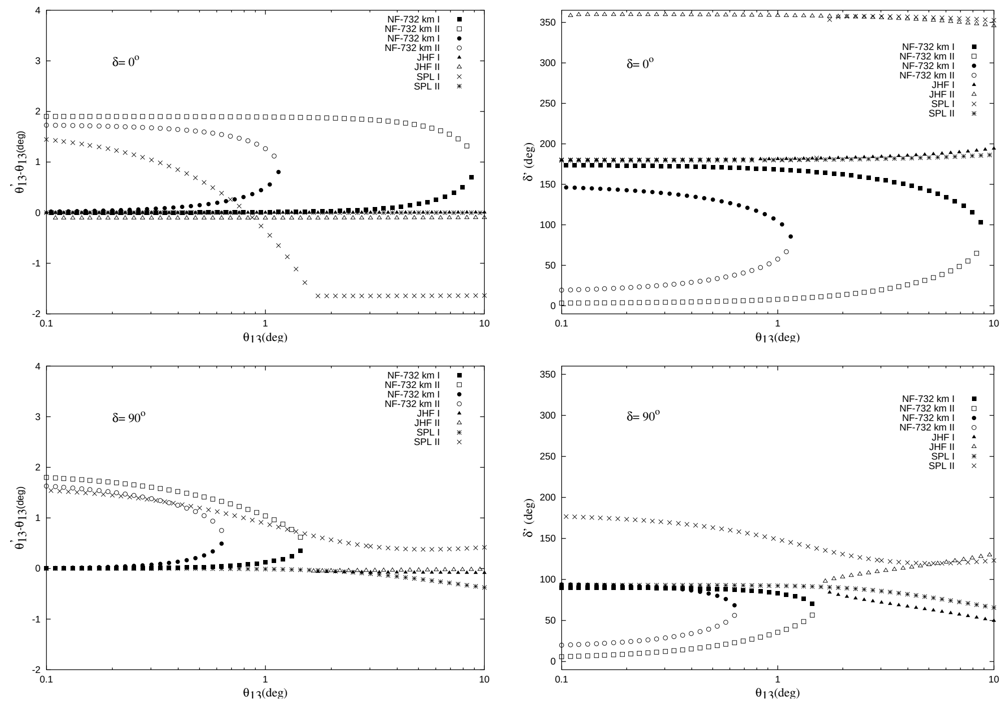

Figure 4.17. $\theta'_{13} - \theta_{13}$ (left) and δ' (right) for the sign degeneracies as functions of θ_{13} for fixed values of $\delta = 0°$ (up) and $\delta = 90°$ (down).

A numerical analysis with fits including realistic background errors and efficiencies confirms the above expectations, at each given facility. There are no fake sign solutions for values of $\theta_{13} > 2°$, when considering just one neutrino factory baseline of $L = 2810$ km (or longer), while for $2° > \theta_{13} > 1°$ they do appear but get eliminated when the data are combined with those from the SPL Superbeam. At $L =$

732 km some fake sign solutions remain close to the present experimental limit for θ_{13}, as shown in figs. 4.16 (right). Once again, in the combination of these latter data with those from the SPL superbeam facility, all fake sign solutions disappear for large $\theta_{13} \geq 4°$, and the sign of Δm^2_{23} could thus be determined from it.

Figures 4.17 also illustrate that solution I is more facility-independent than solution II, as argued above. The solutions that survive in the combinations for small θ_{13} are indeed of type I, as shown in figs. 4.18.

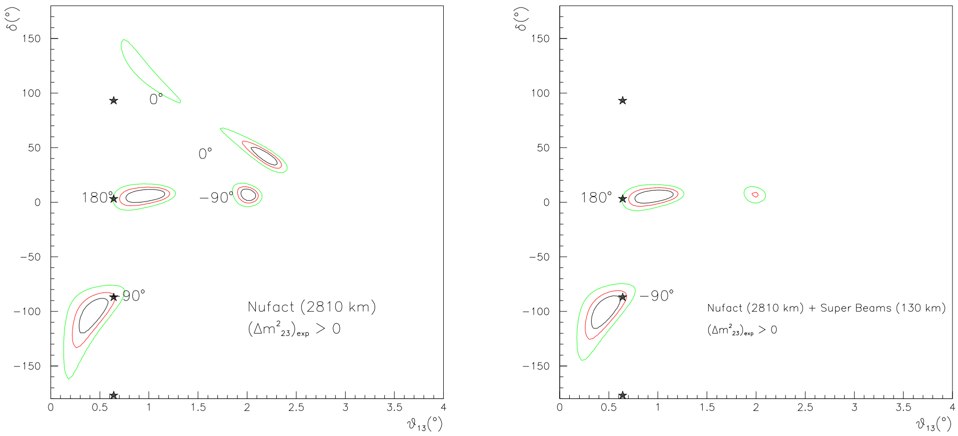

Figure 4.18. Fits resulting in fake sign solutions, for central values $\theta_{13} = 0.6°$ and $\delta = -90°$, $0°$, $90°$, $180°$. The real sign for Δm^2_{23} is positive, while the fits are performed with the opposite sign. The results from a Neutrino Factory baseline at $L = 2810$ km can be appreciated on the left, while their combination with data from the SPL-Superbeam can be seen on the right.

In conclusion, the sign of Δm^2_{23} can be determined from data at an intermediate or long neutrino factory baseline alone for θ_{13} well inside the atmospheric regime. For the larger values of θ_{13}, the combination of data from the superbeam facility and a $L = 732$ m neutrino factory baseline also results in no fake sign solutions.

With lowering θ_{13} ($\theta_{13} > 1°$ for our central parameters), the sign can still be determined through the combination of superbeam and neutrino factory data at the intermediate or long distance.

Finally, for the range $\theta_{13} < 1°$, the sign cannot be determined, but the combination of data from the superbeam facility and an intermediate (or long) neutrino factory baseline is still important to reduce the fake solutions to those of type I, which do not interfere significantly with the determination of θ_{13} and δ.

Concerning the dependence on the solar parameters, it is not expected that the conclusions will change very much with lower sin 2 θ_{12} Δm^2_{12}. The argument for solutions of type II parallels that given in the previous subsection for the intrinsic fake solution, while the existence and position of the type I solutions is pretty insensitive to the solar parameters.

4.5.4 $\theta_{23} \rightarrow \pi/2 - \theta_{23}$ Degeneracy

The present atmospheric data indicate that θ_{23} is close to maximal, although not necessarily 45°. Super-Kamiokande results give 90% CL-allowed parameter regions for $\sin^2 2\theta_{23} > 0.88$, translating into the allowed range $35° < \theta_{23} < 55°$. Therefore even if the value of $\sin^2 2\theta_{23}$ is determined with great accuracy in disappearance measurements, there may remain a discrete ambiguity under the interchange $\theta_{23} \leftrightarrow \pi/2 - \theta_{23}$. If this θ_{23} ambiguity is not cleared up by the time of the neutrino factory operation, supplementary fake solutions may appear when extracting θ_{13} and δ, when the wrong choice of octant is taken for θ_{23}. Fake solutions follow from solving the system of equations, for fixed L and E_ν:

$$
\begin{aligned}
P''_{\nu_e\nu_\mu}(\theta'_{13}, \delta') &= P_{\nu_e\nu_\mu}(\theta_{13}, \delta) \\
P''_{\bar{\nu}_e\bar{\nu}_\mu}(\theta'_{13}, \delta') &= P_{\bar{\nu}_e\bar{\nu}_\mu}(\theta_{13}, \delta)
\end{aligned}
\tag{4.28}
$$

where $P''_{\bar{\nu}_e\bar{\nu}_\mu}$ denotes the oscillation probabilities on the exchange $\theta_{23} \rightarrow \pi/2 - \theta_{23}$.

It turns out that, within the allowed range for the parameters, there are generically two solutions to these equations. They should converge towards the true solutions and its intrinsic degeneracy, in the limit $\theta_{23} \rightarrow \pi/4$. It is called again solution I that which mirrors nature's choice and solution II that which mirrors the intrinsic degeneracy. Because of this parenthood, solution I is a priori expected to present generically less L and E dependence than solution II, and be thus more difficult to eliminate in the combination.

It is easy and simple to obtain the analytical form of the fake degeneracies in the vacuum approximation, in which, from eqs. (4.7) we get

$$
\begin{aligned}
P''_{\nu_e\nu_\mu(\bar{\nu}_e\bar{\nu}_\mu)}(\theta'_{13}, \delta') &= c^2_{23} \sin^2 2\theta'_{13} \sin^2 \frac{\Delta m^2_{23}\, L}{4\, E} \\
&+ s^2_{23} \sin^2 2\theta_{12} \sin^2 \frac{\Delta m^2_{12}\, L}{4\, E} \\
&+ J' \cos\left(\delta' \mp \frac{\Delta m^2_{23}\, L}{4\, E} \right) \frac{\Delta m^2_{12}\, L}{4\, E} \sin\left(\frac{\Delta m^2_{23}\, L}{4\, E} \right)
\end{aligned}
\tag{4.29}
$$

4.5.4.1 Atmospheric Regime

For large θ_{13}, fake θ_{23} solutions are given by

$$\begin{aligned}
\sin\delta' &\simeq \cot\theta_{23}\sin\delta \\
\theta'_{13} &\simeq \tan\theta_{23}\,\theta_{13} \qquad\qquad (4.30)\\
&+ \frac{\sin 2\theta_{12}\,\frac{\Delta m^2_{12}L}{4E}}{2\sin\frac{\Delta m^2_{23}L}{4E}}\left(\cos\!\left(\delta-\frac{\Delta m^2_{23}L}{4E}\right)-\tan\theta_{23}\cos\!\left(\delta'-\frac{\Delta m^2_{23}L}{4E}\right)\right)
\end{aligned}$$

This system describes two solutions. For one of them (I) the L- and E-dependent terms in eqs. (4.30) tend to cancel for $\theta_{23}\to\pi/4$, resulting in $\theta'_{13}=\theta_{13}, \delta'=\delta$ in this limit. The other solution (II) coincides in this limit with that for the intrinsic degeneracy, eq. (4.24), as expected. For both fake θ_{23} solutions, deep in the atmospheric regime the shift $\theta'_{13}-\theta_{13}$ is positive (negative) for $\theta_{23}>(<)\pi/4$. Also, from eqs. (4.30), no fake solutions are expected for $|\cot\,\theta_{23}\,\sin\,\delta|>1$. In the plots of figs. 4.19 and 4.20 are the solutions to eqs. (4.28), including matter effects, for θ_{23} at the two extremes of the 90% CL-allowed interval. It is to note that for large θ_{13} there is one solution (I) that is more facility-independent than the other, although the E, L dependence is sizable for both solutions (see for instance the curves for $\delta=90°$ in figs. 4.20) when θ_{23} is so far from maximal.

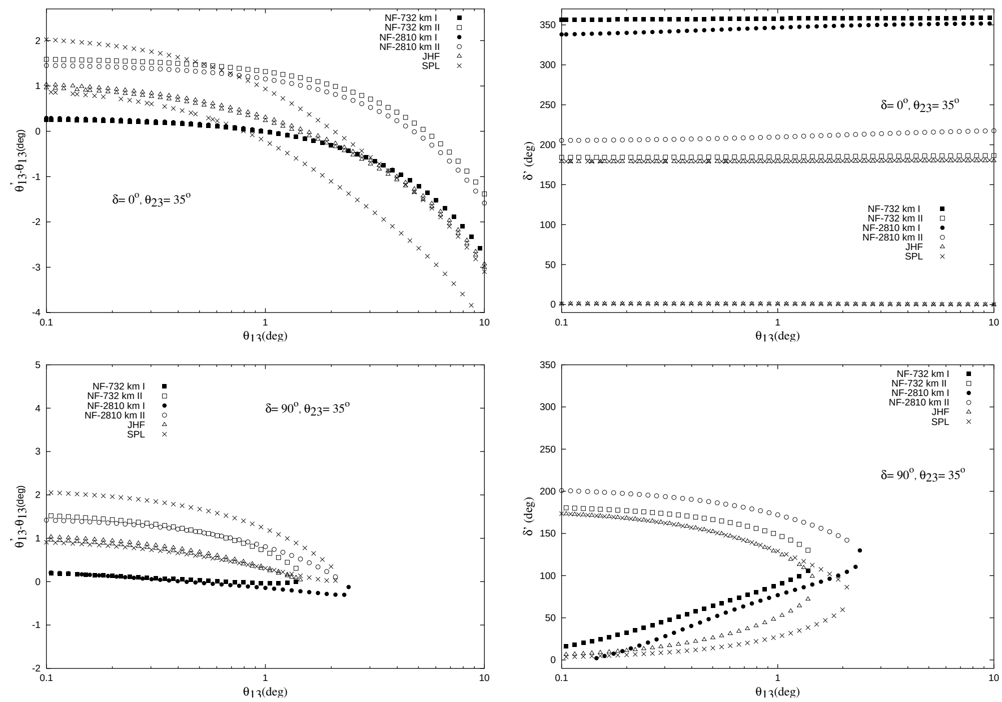

Figure 4.19. $\theta'_{13}-\theta_{13}$ (left) and δ' (right) for the θ_{23} fake solution as functions of θ_{13}, for $\theta_{23}=35°$, for fixed values of $\delta=0°$ (up) and $\delta=90°$ (down).

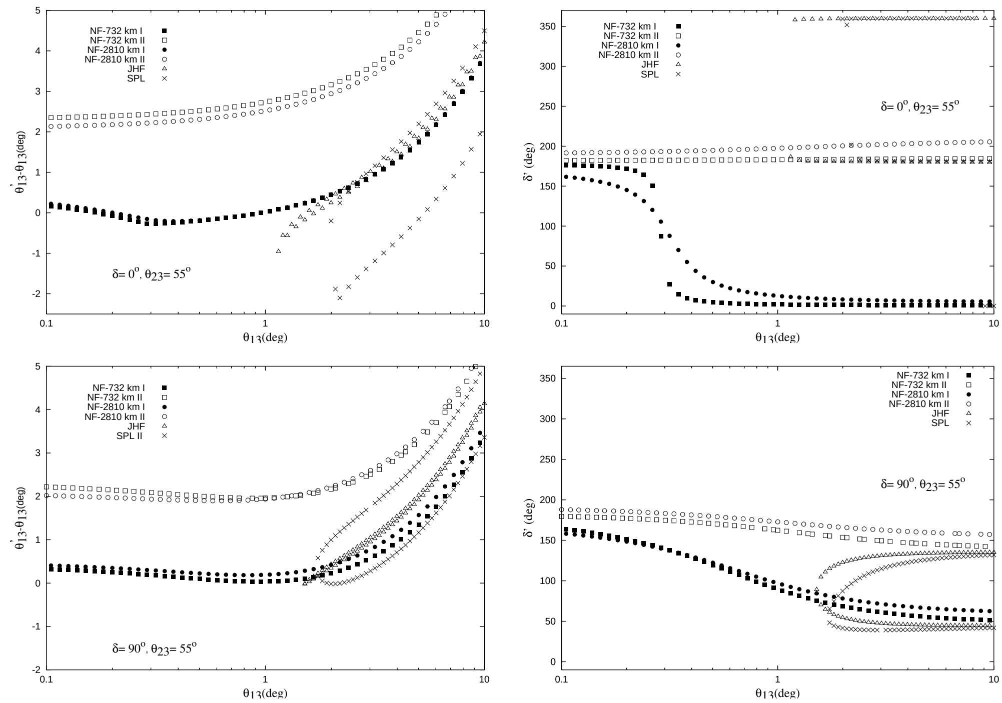

Figure 4.20. $\theta'_{13} - \theta_{13}$ (left) and δ' (right) for the θ_{23} fake solution as functions of θ_{13}, for $\theta_{23} = 55°$, for fixed values of $\delta = 0°$ (up) and $\delta = 90°$ (down).

The fits with the wrong choice of octant for θ_{23} and central values of θ_{23} at the limit of the currently allowed domains, confirm the expectations above and indicate a situation close to that for the fake sign degeneracies, albeit slightly more difficult. For instance, at the $L = 2810$ km baseline of the neutrino factory alone, still some fake θ_{23} solutions remain down to $\theta_{13} > 2°$, but again they all disappear when combined with the SPL superbeam data. As an illustration, in figs. 4.21 are the results for $\theta_{23} = 35°$ and $\theta_{13} = 4°$, at the SPL Superbeam facility (left) and the $L = 2810$ km Neutrino Factory baseline (right). The same exercise but for an $L = 732$ km baseline of the neutrino factory, results in the elimination of the θ_{23} degeneracies only for $\theta_{13} \geq 8°$.

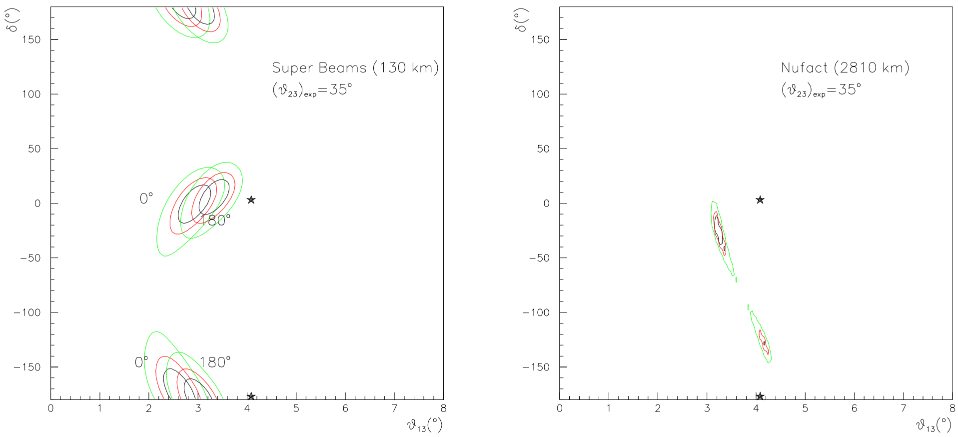

Figure 4.21. Fake solutions due to θ_{23} degeneracies for SPL-Superbeam results (left) and a $L = 2810$ km Neutrino Factory baseline (right), for $\theta_{23} = 35°$, $\theta_{13} = 4°$ and $\delta = -90°, 0°, 90°, 180°$. The combination of the results from both experiments resolves the degeneracies.

4.5.4.2 Solar Regime

For $\theta_{13} \to 0°$, there are again two fake solutions if the following condition is met:

$$\tan^2\theta_{23} < \frac{1}{\sin^2 \frac{\Delta m^2_{23} L}{4E}} \tag{4.31}$$

Otherwise no solution exists. This is important for the larger possible values of θ_{23} and well reflected in figs. 4.20, which show the exact solutions for $\theta_{23} = 55°$. Indeed no fake θ_{23} degeneracies appear in the superbeam facilities in this case, for θ_{13} in the solar regime.

For $\theta_{13} \to 0°$, eqs. (4.28) can be solved to first order in $\epsilon_{23} \equiv \tan\theta_{23} - 1$. Solution I becomes in this limit:

$$\begin{cases} \text{if} \ \ \cos 2\theta_{23} \cot\left(\dfrac{\Delta m^2_{23}\, L}{4\, E}\right) > 0 \ \ \text{then} \ \ \delta' \simeq 0 \\ \text{if} \ \ \cos 2\theta_{23} \cot\left(\dfrac{\Delta m^2_{23}\, L}{4\, E}\right) < 0 \ \ \text{then} \ \ \delta' \simeq \pi \end{cases}$$

$$\theta'_{13} \simeq \sin 2\theta_{12} \frac{\Delta m^2_{12}\, L}{4\, E} \left| \epsilon_{23} \csc\left(\frac{\Delta m^2_{23}\, L}{2\, E}\right) \right| \tag{4.32}$$

Similarly, solution II for $\theta_{13} \to 0°$ is given by:

$$\begin{cases} \text{if} \ \ \cot\left(\dfrac{\Delta m^2_{23}\, L}{4\, E}\right) > 0 \ \ \text{then} \ \ \delta' \simeq \pi \\ \text{if} \ \ \cot\left(\dfrac{\Delta m^2_{23}\, L}{4\, E}\right) < 0 \ \ \text{then} \ \ \delta' \simeq 0 \end{cases}$$

$$\theta'_{13} \simeq \sin 2\theta_{13} \frac{\Delta m^2_{12}\, L}{4\, E} \left(\left| \cot \frac{\Delta m^2_{23}\, L}{4\, E} \right| \pm \epsilon_{23} \cot \frac{\Delta m^2_{23}\, L}{2\, E} \right) \tag{4.33}$$

where the sign $\pm$ corresponds to the sign of $\cot\frac{\Delta m_{23}^2 L}{4E}$. The intrinsic degeneracy, eq. (4.25), is recovered for $\theta_{23} = 45°$. Note that, in the solar regime both fake θ_{23} solutions have a sizable L, E dependence, when θ_{23} is far from maximal. These two solutions can be seen in figs. 4.19 and 4.20 for small θ_{13}. Only for the neutrino factory setups do solutions I and II remain on the same curve in the solar and atmospheric regimes. In the case of the SPL and JHF facilities, they are mixed.

Figures 4.22 show the fits for $\theta_{13} = 0.6°$, for a Neutrino Factory at $L = 2810$ km (left) as well as the same combined with the results from the SPL superbeam facility (right): only one fake solution remains in the latter, which results from the merging of solution I for superbeams and solution II for the neutrino factory, owing to the finite resolution.

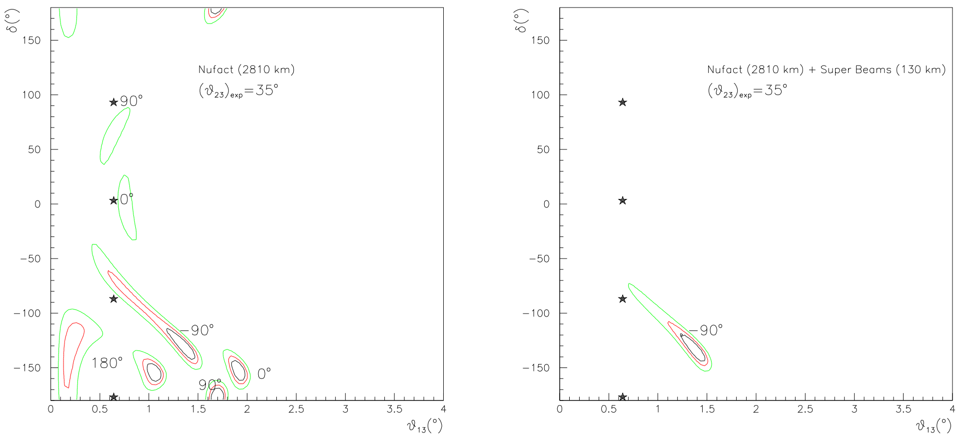

Figure 4.22. Fake solutions due to θ_{23} degeneracies for a $L = 2810$ km Neutrino Factory baseline (left) and its combination with a SPL-Superbeam (right). The central values are $\theta_{13} = 0.6°$ and $\delta = -90°, 0°, 90°, 180°$. The real θ_{23} chosen is $< 45°$, while the fits have been performed with $\theta_{23} > 45°$.

In general, the Neutrino Factory and SPL-Superbeam combination brings an enormous improvement to the solution of these fake degeneracies, particularly for large θ_{13}. The conclusions are rather parallel to those for the fake sign(Δm_{23}^2) solutions, with the caveat that for the θ_{23} ambiguities, solution I, which is harder to resolve, is not that close to satisfying $\sin\delta' = \sin\delta$, and it is thus potentially more harmful to the measurement of CP violation.

As regards the dependence on the solar parameters, the arguments of the previous two subsections can be repeated for solutions I and II, when θ_{23} is close to maximal. When θ_{23} is farther from $\pi/4$, the situation is more confusing since both solutions have a dependence on the solar parameters and a detailed exploration of the whole LMA parameter space is necessary.

4.5.5 The Silver Channels

4.5.5.1 Resolving Intrinsic Degeneracies

One possibility that can help very much to remove degeneracies further is to measure also the $\nu_e \rightsquigarrow \nu_\tau$ and $\bar{\nu}_e \rightsquigarrow \bar{\nu}_\tau$ transition probabilities. The relevance of these *silver* channels in reducing intrinsic degeneracies was studied in ref. [DMM02], in the atmospheric regime. The approximate oscillation probabilities in vacuum for $\nu_e \rightsquigarrow \nu_\tau$ ($\bar{\nu}_e \rightsquigarrow \bar{\nu}_\tau$) are:

$$\begin{aligned} P_{\nu_e\nu_\tau(\bar{\nu}_e\bar{\nu}_\tau)} &= c_{23}^2 \sin^2 2\theta_{13} \sin^2\left(\frac{\Delta m_{23}^2\, L}{4\,E}\right) + s_{23}^2 \sin^2 2\theta_{12} \left(\frac{\Delta m_{12}^2\, L}{4\,E}\right)^2 \\ &- J \cos\left(\pm\delta - \frac{\Delta m_{23}^2\, L}{4\,E}\right) \frac{\Delta m_{12}^2\, L}{4\,E} \sin\left(\frac{\Delta m_{23}^2\, L}{4\,E}\right) \end{aligned} \tag{4.34}$$

They differ from those in eq. (4.7) by the interchange $\theta_{23} \to \pi/2 - \theta_{23}$ and by a change in the sign of the interference term.

For the intrinsic degeneracies in the atmospheric regime, it follows that the sign of $\theta_{13}' - \theta_{13}$ will be opposite to that for the golden $\nu_e \leftrightsquigarrow \nu_\mu$ ($\bar{\nu}_e \leftrightsquigarrow \bar{\nu}_\mu$) channels given in eqs. (4.24). In the solar regime, the intrinsic solutions in these silver channels will thus be identical to eqs. (4.25) upon exchanging $\delta' = 0$ and π, and the combination of the golden and silver channels remains a promising option.

4.5.5.2 Resolving Fake θ_{23} Solutions

When considering only $\nu_e \rightsquigarrow \nu_\tau$ and $\bar{\nu}_e \rightsquigarrow \bar{\nu}_\tau$ oscillations, the location of the fake solutions related to the θ_{23} ambiguity, in the atmospheric regime, is

$$\begin{aligned} \sin\delta' &\simeq \tan\theta_{23} \sin\delta \\ \theta_{13}' &\simeq \cot\theta_{23}\,\theta_{13} \\ &- \sin 2\theta_{23} \frac{\frac{\Delta m_{12}^2\, L}{4\,E}}{2\sin\frac{\Delta m_{23}^2\, L}{4\,E}} \left(\cos\left(\delta - \frac{\Delta m_{23}^2\, L}{4\,E}\right) - \cot\theta_{23} \cos\left(\delta' - \frac{\Delta m_{23}^2\, L}{4\,E}\right)\right) \end{aligned} \tag{4.35}$$

Thus the shift $\theta_{13}' - \theta_{13}$ at large θ_{13} would have the opposite sign to that in eq. (4.30).

In the solar regime, on the other hand, solution I for the ν_τ appearance measurement is the same as that in eq. (4.32), while solution II is different, namely:

$$\begin{cases} \text{if } \cot\left(\dfrac{\Delta m^2_{23}\,L}{4\,E}\right) > 0 \text{ then } \delta' \simeq 0 \\ \text{if } \cot\left(\dfrac{\Delta m^2_{23}\,L}{4\,E}\right) < 0 \text{ then } \delta' \simeq \pi \end{cases} \tag{4.36}$$

$$\theta'_{13} \simeq \sin 2\theta_{12} \frac{\Delta m^2_{23}\,L}{4\,E} \left(\left| \cot \frac{\Delta m^2_{23}\,L}{4\,E} \right| \mp \varepsilon_{23} \cot \frac{\Delta m^2_{23}\,L}{4\,E} \right) \tag{4.37}$$

The condition for the existence of solutions in the solar regime is also different:

$$\cot^2\theta_{23} < \frac{1}{\sin^2\left(\frac{\Delta m^2_{23} L}{4E}\right)} \tag{4.38}$$

A detailed analysis for a realistic experimental setup is being done now, but it is expected that the combination of the two appearance measurements $\nu_e \rightsquigarrow \nu_\mu$ and $\nu_e \rightsquigarrow \nu_\tau$ for both polarities can help to resolve the dangerous solution I associated with the θ_{23} ambiguity, for θ_{13} in the atmospheric regime.

Finally, we recall that the disappearance measurements (e. g.$\nu_\mu \rightsquigarrow \nu_\mu$) should also be helpful in reducing these ambiguities for large θ_{23}. If the angle θ_{23} will turn out to be close to maximal (as the best-fit point now indicates), the θ_{23} degeneracies will be of very little relevance.

4.5.5.3 Resolving Fake sign(Δm^2_{23}) Solutions

As for the removal of the fake sign(Δm^2_{23}) degeneracies, the silver channels will also help, for qualitatively the same reason as in the combination of facilities with opposite value of cot $\frac{\theta_{13}\,L}{4\,E}$. For maximal θ_{23}, the solution of type I in the silver channel is the same in vacuum as that in the golden $\nu_\mu \leftrightsquigarrow \nu_e$ channel, and it is thus not expected to disappear in the combination of the two appearance measurements. The solution of type II, instead, has an opposite displacement in θ_{13} in the atmospheric regime and a difference of 180° in the phase in the solar one.

Chapter 5

New Long Baseline Experiments: How It All Fits Together

5.1 Beta Beam

The β-beam was first introduced in [Zuc01], [Zuc02]. It involves producing a beam of β-unstable heavy ions, accelerating them to some reference energy, and allowing them to decay in the straight section of a storage ring, resulting in a very intense neutrino beam. Two ions have been identified as ideal candidates: ^{6}He, to produce a pure $\bar{\nu}_e$ beam, and ^{18}Ne, to produce a pure ν_e beam. The golden subleading transitions $\nu_e \rightsquigarrow \nu_\mu$ and $\bar{\nu}_e \rightsquigarrow \bar{\nu}_\mu$ can be measured through the appearance of muons in a distant detector.

As in the case of muon-induced neutrino beams, the β-beam offers the unique features of being *pure* (only one neutrino species, in contrast to a conventional beam, where knowledge of the spectrum always involves a sizable systematic uncertainty).

One of the most attractive features of the β-beam is that it leverages existing CERN facilities. The original design, whose feasibility with existing technology has been demonstrated [A+03], envisions a "low-"γ scenario, in which ions are produced by a new facility (EURISOL), accelerated by the present SPS to $\gamma \leqslant 150$, and stored in a storage ring (also a new facility) with straight sections pointing to the experimental area.

An underground location where a very massive neutrino detector could be located has been identified in the Fréjus tunnel, roughly 130 km from CERN. This baseline is ideal for exploring the first peak of the atmospheric oscillation, the optimal environment to search for CP-violating effects. A new, very large cavern excavated in the Fréjus tunnel would host a megaton water Cerenkov detector UNO-style. The capabilities of such a detector are well-matched to this energy range, and the low neutrino energies produced by the low-γ option (in the range of a few hundred MeV) require a very large mass to compensate for the tiny cross-sections.

Furthermore, the existing design calls for a conventional low-energy "super-beam" based on the proposed SPL proton driver, that would deliver a total power-on-target of about 4 MW, resulting in a very intense neutrino beam. The physics reach of such a super-beam has been studied in detail, both alone [SuperBeams01], and together with a low-γ β-beam [Mez03], [BLM04]. The results of these studies can be summarized as follows:

- Neither the SPL super-beam nor the low-γ β-beam, by themselves, result in fully-satisfactory performance, especially compared to other proposed facilities such as T2K [T2K01]. The performance is limited, in spite of the large detector mass by the small cross-sections, by systematics due to the SPL super-beam backgrounds (both beam- and detector-related) and by the intrinsic degeneracies identified in [BCGGC+01].
- A combination of the super-beam and β-beam would explore a large range of the parameter space (θ_{13}, δ).
- The sign of the atmospheric Δm^2_{23} cannot be determined because matter effects are negligible.

5.1.1 Energy Regimes

We explored different scenarios increasing the energy of the originally proposed β-beam, with a corresponding increase in baseline to keep $\langle E_\nu \rangle / L$ approximately constant, and also when the constraints are a fixed detector distance (CERN-Fréjus) and the maximum γ achievable at the current and an refurbished SPS.

There are three reasons to expect an improvement of sensitivity with higher γ values:

- The rates (and thus the sensitivity to θ_{13} if the backgrounds are kept under control) increase linearly with $\langle E_\nu \rangle$ at fixed $\langle E_\nu \rangle / L$.
- At longer baselines, measurement of the neutrino mass hierarchy becomes possible, as matter effects become more sizable. This is illustrated in figure 5.1, which shows the $\nu_e \rightsquigarrow \nu_\mu$ oscillation probability for neutrinos and antineutrinos, as a function of the baseline, for neutrino energy constrained to the first atmospheric peak, i.e. $E/L = \left|\Delta m^2_{23}\right| / 2\,\pi$. The difference between the neutrino and antineutrino oscillation probabilities induced by matter effects becomes comparable to that due to CP-violation for $L \sim 1000\,\mathrm{km}$.
- Increased neutrino energy enhances the energy dependence of oscillation signals. This is extremely useful in resolving the correlations and degeneracies in parameter space [C+00], [BCGGC+01]. Energy dependence is particularly helpful for energies close to the peak of the atmospheric oscillation [BCGGC+02]. Figure 5.2 compares the vacuum probabilities for $\nu_e \rightsquigarrow \nu_\mu$ and $\bar{\nu}_e \rightsquigarrow \bar{\nu}_\mu$ with $\theta_{13} = 6°$ and $\delta = 40°$ to those of the intrinsic-degenerate solution at $\left\langle E_{\nu(\bar{\nu})} \right\rangle$. The neutrino and antineutrino probabilities cross at the $\left\langle E_{\nu(\bar{\nu})} \right\rangle$, but are quite different at other energies. Thus spectral information can definitely help in disentangling them.

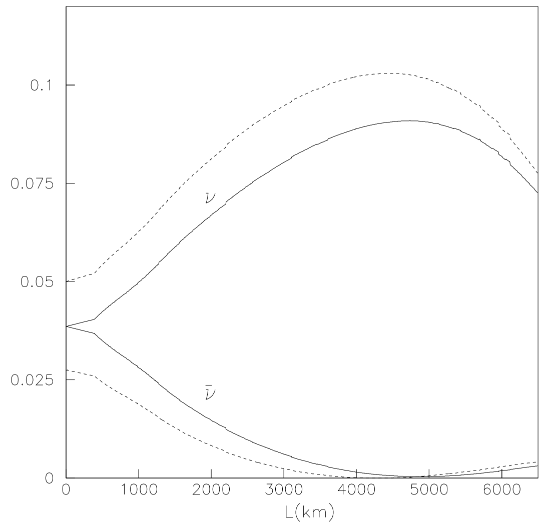

Figure 5.1. $P_{\nu_e\nu_\mu}$ and $P_{\bar{\nu}_e\bar{\nu}_\mu}$ as a function of the baseline L, at a neutrino energy $E/L = |\Delta m^2_{23}|/2\pi$ and for $\theta_{13} = 8°$ and $\delta = 0°$ (solid) and $90°$ (dashed).

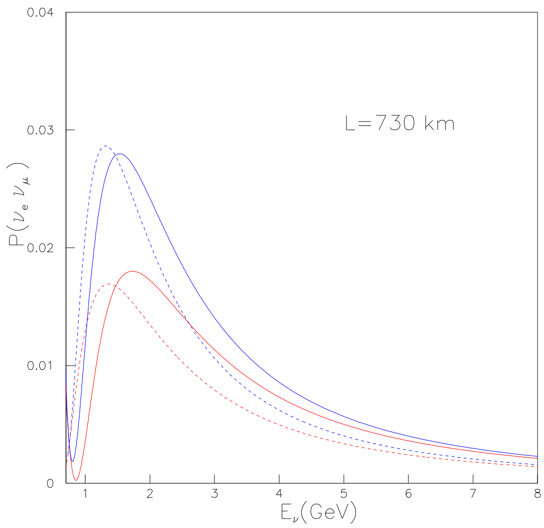

Figure 5.2. $P(\nu_e \rightsquigarrow \nu_\mu)$ and $P(\bar{\nu}_e \rightsquigarrow \bar{\nu}_\mu)$ as a function of the energy, at $L = 730$ km, for $\theta_{13} = 6°$ and $\delta = 40°$ (solid) and for the degenerate solution at $\theta'_{13}(\langle E_\nu \rangle)$, $\delta'(\langle E_\nu \rangle)$ with $\langle E_\nu \rangle = 1.5\,\text{GeV}$ (dashed).

From a technical point of view, designs aiming at higher γ factors are conceivable by direct extrapolation of existing technology, and would not require a long R&D program. A "medium-"γ scenario ($\gamma \leqslant 600$) could be realized at CERN by accelerating ions in a refurbished SPS with super-conducting magnets, or in LHC (up to $\gamma = 2488$ for ^{6}He and $\gamma = 4158$ for ^{18}Ne). Another candidate would be Fermilab, where a combination of the existing Main-Injector and Tevatron could accelerate ions to γ factors of a few hundred.

Two blocks of three scenarios for the β-beam alone are considered. With a fixed $\langle E_\nu \rangle / L$ on the oscillation peak:

- Setup-1, low energy: $\gamma = 60$ for ^{6}He and $\gamma = 100$ for ^{18}Ne, with $L = 130$ km (CERN-Fréjus).
- Setup-2, medium energy: $\gamma = 350$ for ^{6}He and $\gamma = 580$ for ^{18}Ne, with $L =$ 732 km (e.g. CERN-Gran Sasso with a refurbished SPS or with the LHC, FNAL-Soudan with Tevatron).
- Setup-3, high energy: $\gamma = 1500$ for ^{6}He and $\gamma = 2500$ for ^{18}Ne, with $L =$ 3000 km (e.g. CERN-Canary islands with the LHC).

And with the constraints of a fixed distance CERN-Fréjus and the maximum γ achievable at the SPS:

- Setup-4: $L = 130$ km (CERN-Fréjus) at the optimal γ accessible to the SPS.
- Setup-5: $\gamma = 150$ (maximum achievable at the SPS) for both ions, at the optimal baseline.
- Setup-6: $\gamma = 350$ for both ions at $L = 730$ km, a symmetric version of Setup-2.

In all cases we assume the same number of ions, 2.9×10^{18} ^{6}He and 1.1×10^{18} ^{18}Ne decays per year. This seems reasonable, as one does not expect losses with a refurbished SPS (to extrapolate, for instance, Setup-1 and Setup-2 at CERN). For the LHC one could compensate for injection losses due to the different optics with a different acceleration scheme with more or longer bunches (thus more ions). Although these luminosities have been estimated for simultaneous ion circulation (fixing the ratio of γ's to 1.67) they may be achievable even if the ions circulate separately at the same γ, by injecting more bunches. While these intensities are realistic for the CERN-SPS, the same has not been demonstrated for other accelerators like the Tevatron or LHC.

5.1.2 Neutrino Fluxes

Neglecting small Coulomb corrections, the electron energy spectrum produced by an "allowed" nuclear β-decay at rest is described by:

$$\frac{dN^{\text{rest}}}{dp_e} \sim p_e^2 \, (E_e - E_0)^2 \tag{5.1}$$

where E_0 is the electron end-point energy and E_e and p_e are the electron energy and momentum. For ^{6}He, $E_0 = 3.5\,\text{MeV} + m_e$, while for ^{18}Ne, $E_0 = 3.4\,\text{MeV} + m_e$.

We are interested instead in the neutrino spectrum resulting from ion decays after they are boosted by some fixed γ. In the ion rest frame the spectrum of the neutrino is

$$\frac{dN^{\mathrm{rest}}}{d\cos\theta\, dE_\nu} \sim E_\nu^2\,(E_0 - E_\nu)\,\sqrt{(E_0 - E_\nu)^2 - m_e^2} \tag{5.2}$$

After performing the boost and normalizing the total number of ion decays to be N_β per year, the neutrino flux per solid angle in a detector located at a distance L aligned with the straight sections of the storage ring is:

$$\frac{d\Phi^{\mathrm{lab}}}{dS\,dy}\,(\theta \simeq 0) \simeq \frac{N_\beta}{\pi\,L^2}\,\frac{\gamma^2}{g(y_e)}\,y^2\,(1-y)\,\sqrt{(1-y)^2 - y_e^2} \tag{5.3}$$

where $0 \leqslant y = \frac{E_\nu}{2\,\gamma\,E_0} \leqslant 1 - y_e,\ y_e = m_e/E_0$ and

$$g(y_e) \equiv \frac{1}{60}\left(\sqrt{1-y_e^2}\,(2 - 9\,y_e^2 - 8\,y_e^4) + 15\,y_e^4\log\!\left(\frac{y_e}{1-\sqrt{1-y_e^2}}\right)\right) \tag{5.4}$$

This expression has certain similarities with the electron neutrino fluxes at a Neutrino Factory. One similarity is that the fluxes are known very accurately and the $\nu_\mu(\bar{\nu}_\mu)$ appearance signal has no background from contamination of the beam. The latter is true for the Neutrino Factory only to the extent that the charge of final-state leptons can be determined, which requires a magnetized device (thus, in particular, prevents the use of massive water detectors).

Figure 5.3 shows these fluxes for different reference setups as a function of the neutrino energy. Although integrated fluxes at all the reference setups are nearly identical, about $10^{11}\,\bar{\nu}_e/\nu_e\,m^{-2}\,\mathrm{year}^{-1}$, setups 2, 3 and 5, 6 have the advantage that the appearance signal's energy dependence should be more significant, while at low energy the neutrino energy resolution is worsened by the Fermi motion.

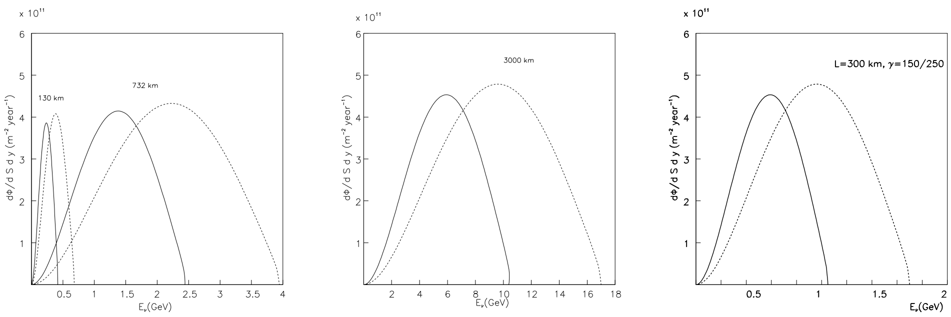

Figure 5.3. Fluxes for setups 1 and 2 (left), 3 (center) and 4 (right) as function of the neutrino energy for $\bar{\nu}_e$ (solid) and ν_e (dashed).

The Neutrino Factory flux of $10^{12}\,\bar{\nu}_e/\nu_e\,m^{-2}\,\mathrm{year}^{-1}$ at the optimum baseline of 3000 km is a factor 10 higher, but $\langle E_\nu\rangle/L$ for setups 2 and 3 is matched to the atmospheric splitting, while at the Neutrino Factory it is not. The oscillation probabilities are thus smaller in the latter.

5.1.3 Measurements

The parameters (θ_{13}, δ) are best studied by probing the appearance channels for neutrino oscillations in the atmospheric energy range: golden ($\nu_\mu \leftrightsquigarrow \nu_e$) [DGH99] [C+00] and silver ($\nu_\tau \leftrightsquigarrow \nu_e$) [DMM02] channels have been identified. In all setups but Setup-3, neutrino energies are below τ threshold, therefore only the golden channel is available.

The disappearance transition $\nu_e \rightsquigarrow \nu_e$ can also be measured. This is an important complement to the golden channel, because the intrinsic degeneracy in the golden measurement can be resolved: the disappearance measurement depends on θ_{13}, but not on δ. The synergy between the appearance and disappearance channels for a β-beam is thus analogous to that between superbeam and reactor experiments [MMS+03].

5.1.4 Cross-Sections

The (anti-)neutrino cross–sections relevant in the different setups are quite different. While in the low energy option quasi-elastic events are dominant and the cross-section grows rapidly with energy, in the highest-energy option samples are mostly deep-inelastic scattering and the growth is linear in the neutrino energy. For the medium-energy options, there is a sizable contribution from both types of events, as well as resonant channels. Figure 5.4 shows the cross-sections per nucleon and per neutrino energy used in this analysis.

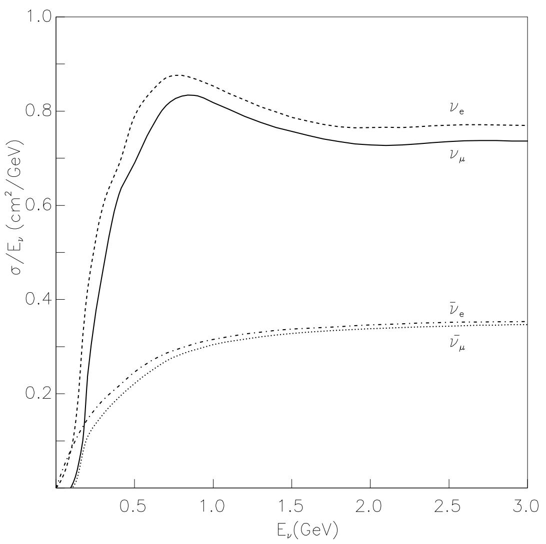

Figure 5.4. Cross-section per nucleon for an isoscalar target, divided by neutrino energy in GeV.

Asymptotically the number of events grows linearly with γ. Table 5.1 shows the number of charged-current events expected in one year, per kiloton. The number of events is somewhat sensitive to the isotopic composition of the target, as free protons in water contribute significantly to the anti-neutrino event rates.

Setup	γ	L(km)	$\bar{\nu}_e$ CC	ν_e CC	$\langle E_\nu \rangle$ (GeV)
1	60/100	130	4.7	32.8	0.23/0.37
2	350/580	730	57.5	224.7	1.35/2.18
3	1500/2500	3000	282.7	993.1	5.80/9.39
4	150/250	300	22.8	115.6	0.58/0.94

Table 5.1. Number of charged-current events without oscillations per kiloton-year for reference setups. The average neutrino energy is also shown.

Interestingly, the detector mass can be reduced linearly with γ without changing the number of events. This offers the possibility of moving from the large water Cerenkov detector required in the lowest-energy option to a less massive but more granular detector in the higher-energy ones.

5.1.5 Detectors: Efficiencies and Backgrounds

The signature for the golden subleading transitions $\nu_e \rightsquigarrow \nu_\mu$ and $\bar{\nu}_e \rightsquigarrow \bar{\nu}_\mu$ in a β-beam is the appearance of prompt muons which must be separated from the main background of prompt electrons due to the bulk $\nu_e/\bar{\nu}_e$ charged interactions. Since there is only one neutrino species in the beam, no charge identification is required. Furthermore, to compensate the small cross sections, specially for Setup-1, very massive detectors are needed. In addition, good energy resolution is required in order to resolve parameter degeneracies. As demonstrated by Super-Kamiokande [Super-Kamiokande98], massive water detectors are capable of offering simultaneously excellent particle identification and good energy resolution, particularly in the range of few hundred MeV to about 1 GeV, where most of the interactions are quasi elastic, yielding simple event topologies (a typical QE interaction is characterized by a single ring from the final muon, the scattered proton being below Cerenkov threshold thus invisible). As energy increases, deep inelastic processes start to dominate the cross section and the event topology becomes more complicated. The turn-over region is about 1.5 GeV. The neutrino spectra in Setup-2 extend all the way up to 4 GeV. Nevertheless, as it will be shown below, water is still the best option in this range.

For neutrinos energies up to 10 GeV, as considered in Setup-3, deep inelastic CC and NC events are dominant and water is no longer suitable. Massive tracking calorimeters are the best option in this range [CDG00] [C+00].

5.1.5.1 Signal Selection and Background Suppression in Water

We have considered a Megaton-class water detector, as proposed by the UNO collaboration [G+] with a fiducial mass of 400 kiloton, for both setups I and II. The response of the detector was studied using the NUANCE [Cas02] neutrino physics generator and detector simulation and realistic reconstruction algorithms as described in [SuperBeams01].

Particle identification in water exploits the difference in the Cerenkov patterns produced by showering ("e-like") and non-showering ("μ-like") particles. Besides, for the energies of interest the difference in Cerenkov opening angle between an electron and a muon can also be exploited. Furthermore, muons which stop and decay (100% of μ^+ and 78% of μ^-) produce a detectable delayed electron signature that can be used as an additional handle for background rejection.

For this study, we have used a particle identification criterion similar to the one used by the Super-Kamiokande collaboration, which is based on a maximum likelihood fit of both μ-like and e-like hypotheses. Figure 5.5 shows the particle identification estimator P_{id}, for electron-like events (solid line) and for muon-like events (dashed line). The normalization is arbitrary. A cut at $P_{\mathrm{id}} > 0$ (PID cut) separates optimally the e-like and μ-like populations. Since most ν_μ events are followed by a muon-decay signature, the background is further reduced by accepting only events with a delayed coincidence.

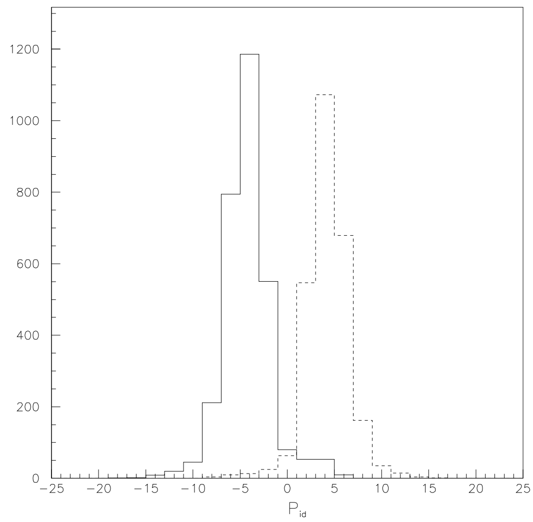

Figure 5.5. Rejection of ν_e^{CC} background in a water Cerenkov detector. The particle ID estimator P_{id} is shown in arbitrary units for the electron-like background (left, solid line) and muon-like signal (right, dashed).

To summarize, the appearance event selection requires:

- The event must be fully contained in the fiducial volume. This is necessary to guarantee a good measurement of the energy as well as to exploit the muon-decay signature.
- A single ring in the event.
- The PID estimator must be muon-like, $P_{\mathrm{id}} > 0$.
- The event must show a delayed signature (muon decay signature).

For the disappearance $\nu_e \rightsquigarrow \nu_e$ ($\bar{\nu}_e \rightsquigarrow \bar{\nu}_e$) transitions, the signal is a CC interaction with an electron (positron) in the final state. In setups 1 and 2 this channel is included with a conservatively estimated 50% flat efficiency and negligible background. The energy resolution is strongly affected by the non-QE contamination for this sample, and so the posterior analysis in setups 4–6 are refined to include the effect of migrations. While the background level for this large signal can be safely neglected in comparison with other systematic errors, a matrix of efficiencies should be used to account for the signal migrations. Table 5.2 shows these matrices for ^{6}He and ^{18}Ne at various γ's. Efficiencies are quite high, especially at lower energies where they reach 80-90%.

Ion	γ	$\epsilon_{ij}^{\mathrm{dis}}$
^{6}He	120	$\begin{pmatrix} 0.89 & 0.25 & 0.10 \\ 0.04 & 0.62 & 0.40 \\ 0.00 & 0.023 & 0.38 \end{pmatrix}$
^{18}Ne	120	$\begin{pmatrix} 0.83 & 0.35 & 0.21 \\ 0.073 & 0.46 & 0.36 \\ 0.0015 & 0.043 & 0.22 \end{pmatrix}$
^{6}He	150	$\begin{pmatrix} 0.89 & 0.21 & 0.086 \\ 0.045 & 0.63 & 0.25 \\ 0.00 & 0.041 & 0.52 \end{pmatrix}$
^{18}Ne	150	$\begin{pmatrix} 0.83 & 0.33 & 0.16 \\ 0.078 & 0.47 & 0.27 \\ 0.0019 & 0.059 & 0.33 \end{pmatrix}$

Table 5.2. Fractional migration matrices ($\epsilon_{ij}^{\mathrm{dis}}$) of the CC ν_e disappearance signal for different values of γ.

5.1.5.2 Atmospheric Background

An important background for any accelerator-based experiment to control arises from atmo- spheric neutrinos. A detector like Super-Kamiokande will expect approximately 120 ν_μ and $\bar{\nu}_\mu$ interactions per kiloton-year (including the disappearance of ν_μ into ν_τ). Of these, 32 atmospheric ν_μ and $\bar{\nu}_\mu$ per kiloton-year pass all the selection cuts (one non-showering ring, accompanied by a delayed coincidence from muon decay). The reconstructed spectrum of those events scaled by a factor 1/500 is shown in figure 5.6 (solid line) alongside the signal for three example setups, assuming $\theta_{13}=1°$.

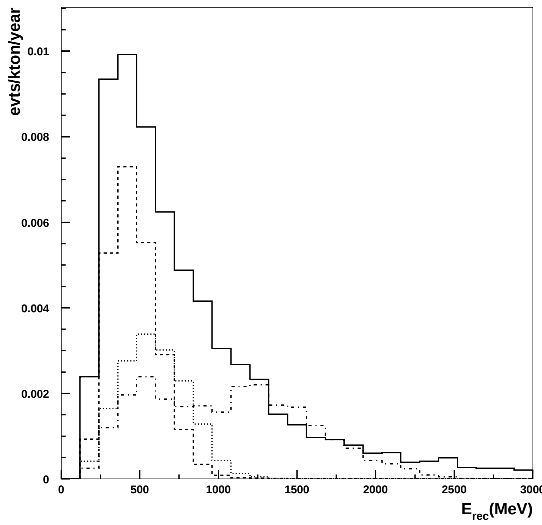

Figure 5.6. Solid line: energy spectrum of atmospheric ν_μ and $\bar{\nu}_\mu$ background per kiloton-year, scaled down by a factor 1/500. Dashed, dotted and dash-dotted lines: energy spectrum of signal events per kiloton-year for $\gamma=120, 150$ and 350 assuming $\theta_{13}=1°$.

There are two additional handles to further reduce the atmospheric background. First, at a given γ, we know the end-point of the signal spectrum, and there is no efficiency penalty for excluding events above the maximum beam energy. This cut obviously works best for lower-γ scenarios. Table 5.3 shows the effect of the end-point cut for different γ's. For higher γ, it is also helpful to set a *lower* energy cut. Requiring $E \geqslant 500$ MeV, for instance, is free for the $\gamma = 350$ option, since this bin is not considered in the analysis anyway.

γ	Selection	$E_{\rm max}$ cut	$E_{\rm min}$ cut	$\cos\theta_l$ cut
120	32	19	19	15
150	32	24	24	15
350	32	30	19	5

Table 5.3. Surviving atmospheric ν_μ background per kton-year after cuts: on the high-energy end-point of the β-beam neutrino spectrum ($E_{\rm max}$), the low-energy tail ($E_{\rm min}$) for setup 6, and the lepton scattering angle ($\cos\theta_l$).

Second, a directional cut is also possible, since the beam arrives from a specific, known direction but the atmospheric background is roughly isotropic. While the neutrino direction cannot be measured directly, it is increasingly correlated with the observable lepton direction at high energies. Figure 5.7 illustrates this correlation for three reference setups. Thus, a directional cut is more effective as γ increases, but is never perfectly efficient. To compare the power of this cut for the different setups, we define it to achieve a 90% efficiency in all cases: $\cos\theta_l > 0.45$ for $\gamma = 350$, $\cos\theta_l > -0.3$ for $\gamma = 150$ and $\cos\theta_l > -0.5$ for $\gamma = 120$. The remaining atmospheric background for each setup is summarized in Table 5.3. Thanks to the directional cut, background rejection for the highest γ is a factor three better than the alternative scenarios.

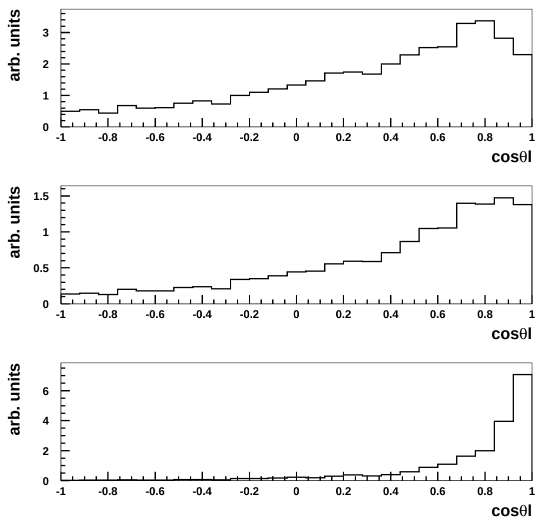

Figure 5.7. Cosine of the reconstructed neutrino-lepton scattering angle for three setups: $\gamma = 120$ (top), $\gamma = 150$ (middle) and $\gamma = 350$ (bottom).

Even with energy and directional cuts, 5 to 15 atmospheric ν_μ background events per kiloton-year remain, compared to the expected intrinsic beam-induced detector background (mostly due to NC single-pion production) of $\mathcal{O}(10^{-2})$ events. To reduce atmospheric contamination to a negligible level (say ten times below the intrinsic background) would require a rejection factor $\mathcal{O}(10^4)$, although since the atmospheric background can be well measured a rejection factor 5–10 times less stringent is probably tolerable.

This rejection factor can be achieved by timing of the parent ion bunches. It is estimated [Mez03] that a rejection factor of 2×10^4 is feasible with bunches 10 ns in length. Based on the present results, a less demanding scheme for the number of bunches and bunch length could be workable.

5.1.6 Systematic Errors

For setups 4–6 we have included the two systematic errors that will likely dominate. First, the uncertainty in the fiducial mass of the near and far detectors, which we estimate as a $\pm 5\%$ effect on the expected far-detector rate. Second, the uncertainty on the ratio of anti-neutrino/neutrino cross sections, which we assume a near detector can measure with an accuracy of $\pm 1\%$.

To include these errors, two new parameters are added to the fits: A, the global normalization, and x, the relative normalization of anti-neutrino to neutrino rates. More precisely, if $n_{\mu,e}^{i,\pm}$ is the number of measured muon and electron events in the energy bin i for the antineutrino $(+)$ or neutrino $(-)$ beam, and $N_{\mu,e}^{i,\pm}(\theta_{13},\delta)$ is the expected number for some values of the unknown parameters (θ_{13},δ), then we minimize the following χ^2 function:

$$\begin{aligned}\chi^2(\theta_{13},\delta,A,x) = 2\sum_{i,f=e,\mu}\Bigg\{ & \quad A\,x\,N_f^{i,+} - n_f^{i,+} + n_f^{i,+}\log\left(\frac{n_f^{i,+}}{A\,x\,N_f^{i,+}}\right)\\ & + \; A\,N_f^{i,-} - n_f^{i,-} + n_f^{i,-}\log\left(\frac{n_f^{i,-}}{A\,N_f^{i,-}}\right)\Bigg\}\\ & + \; \frac{(A-1)^2}{\sigma_A^2} + \frac{(x-1)^2}{\sigma_x^2}\end{aligned}$$

where $\sigma_A = 0.05$ and $\sigma_x = 0.01$. The minimization in the parameters A and x for fixed values of θ_{13} and δ can be done analytically to leading order in the deviations $A-1$ and $x-1$, that is solving the linearized system:

$$\frac{\partial\chi^2}{\partial A} = 0 \qquad \frac{\partial\chi^2}{\partial x} = 0 \tag{5.5}$$

5.1.7 Signal and Backgrounds in Setup-1

The PID cut eliminates almost completely the electron background, leaving a residual back- ground due to ν_e^{NC} and diffractive events in which a single pion is confused with a muon. The low energy of Setup-1 (particularly in the case of the antineutrinos) results in negligible backgrounds for ^{6}He. In the case of ^{18}Ne, diffractive events result in an integrated background fraction below 10^{-2}. The efficiency is rather large but drops dramatically below 300 MeV. Background ratio and efficiency as a function of the energy in Setup-1 are shown in figure 5.8.

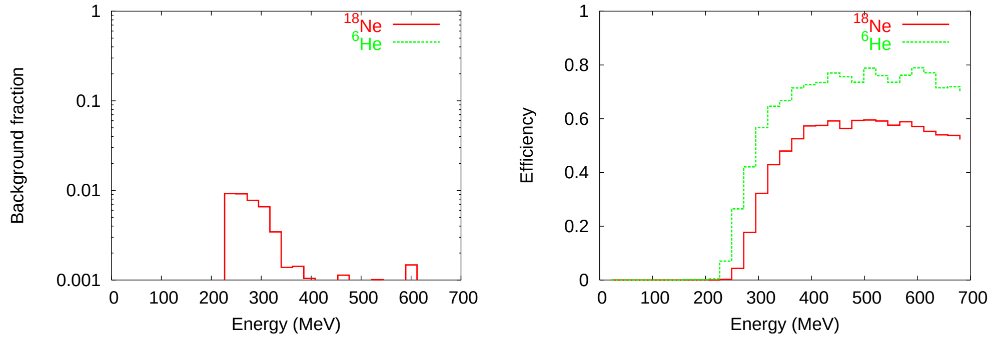

Figure 5.8. Background fraction (left) and efficiency (right) as a function of the true neutrino energies for ^{6}He and ^{18}Ne in water in Setup-1.

A major drawback of Setup-1 is that no energy binning is possible, since the neutrino energy is of the order of the Fermi motion. This is illustrated in figure 5.9 where the reconstructed neutrino energy is plotted against the true energy. As it can be seen the events are almost uncorrelated. Therefore, spectral information cannot be used and one has to do with the integrated signal, which cannot resolve the intrinsic degeneracies.

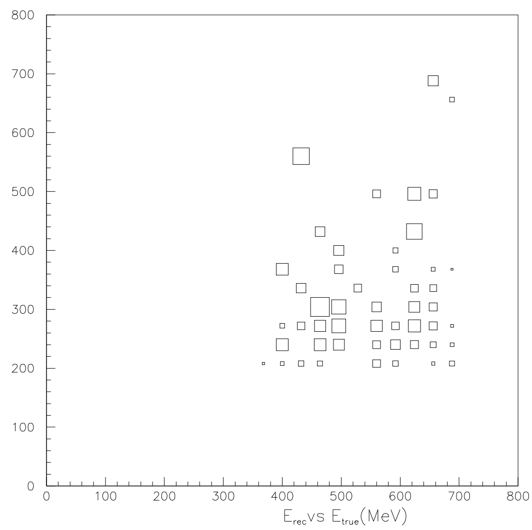

Figure 5.9. Reconstructed versus true neutrino energy for ^{18}Ne. The lack of correlation shows that the event energy information is completely washed out by Fermi motion.

5.1.8 Signal and Backgrounds in Setup-2

Figure 5.10 shows the reconstructed energy spectrum for both signal and background in Setup-2. Notice that, as for Setup-1, the backgrounds are smaller for ^{6}He than for ^{18}Ne, and that both neutrino and antineutrino backgrounds tend to cluster at low energies. A cut demanding that the reconstructed energy be larger than 500 MeV suppresses most of the residual backgrounds at a modest cost for the efficiency.

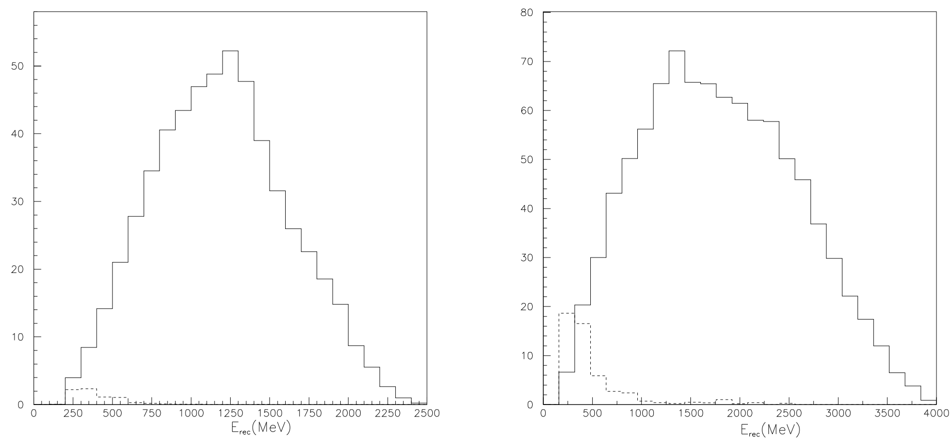

Figure 5.10. Reconstructed energy for signal and background in Setup-II (the absolute normalization is arbitrary) for ^{6}He (left) and ^{18}Ne (right).

Figure 5.11 shows the reconstructed energy (solid line), the QE component (dotted line) and the non-QE component (dashed line) for events passing the selection criteria. Notice that the non-QE contamination is high, specially for neutrino events. This spoils sizeably the resolution, since the neutrino energy is reconstructed under the hypothesis that the interaction was QE. The effect is illustrated in figure 5.12, which shows the reconstructed versus true energy for antineutrinos in Setup-2 for QE events only (left) and all events (QE and non QE) that pass the selection criteria (right). Notice the excellent correlation between reconstructed and true energy in the case of QE events, which is, however, spoiled by the non-QE events. We take into account this effect by computing a matrix that describes the migrations between the true and the reconstructed neutrino energy. Migration matrices have also been computed for the backgrounds. Figures 5.13 and 5.14 show those matrices (in the form of lego-plots) for ^{6}He and ^{18}Ne respectively. The integrated efficiencies are quite high ($30 - 50\%$) for background fractions below 3×10^{-3}.

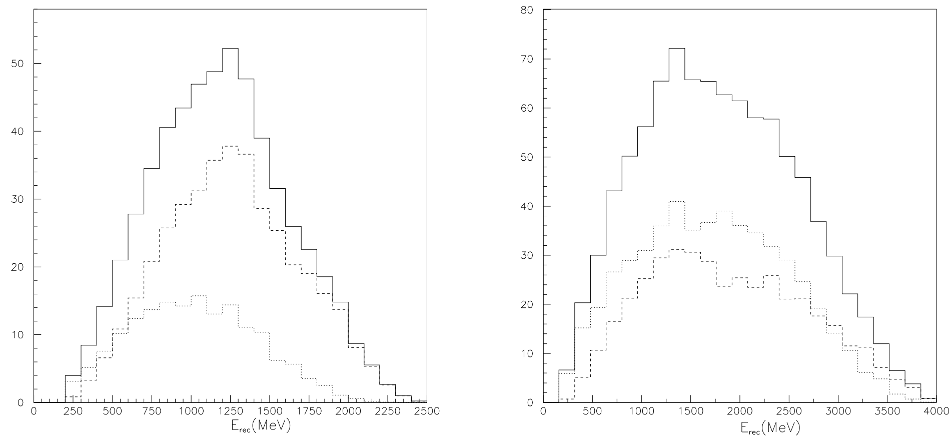

Figure 5.11. Reconstructed energy (solid line), the QE component (dotted line) and the non-QE component (dashed line) for signal-like events (arbitrary normalization) for ^{6}He (left) and ^{18}Ne (right).

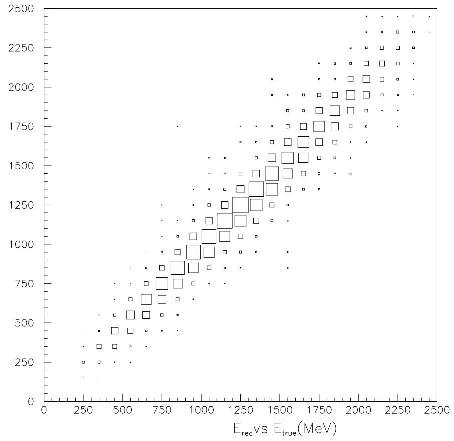

Figure 5.12. Reconstructed versus true energy for antineutrinos in Setup-II for QE events on the left and for signal-like events (QE and non-QE events) on the right.

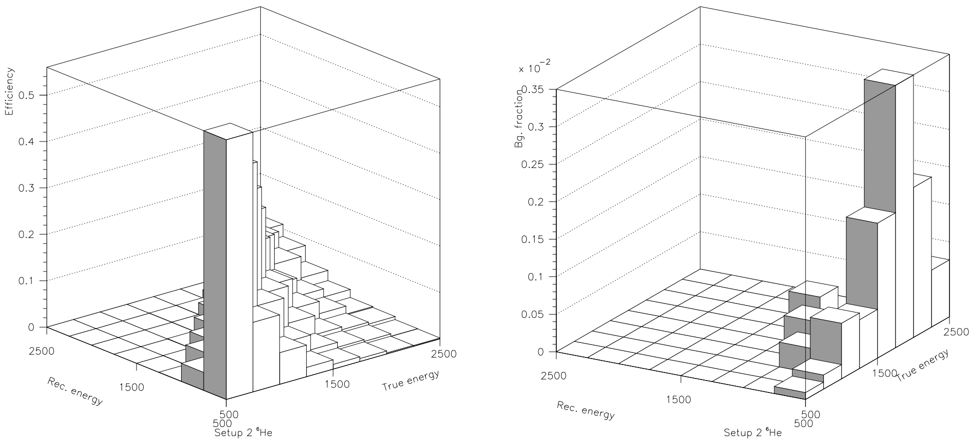

Figure 5.13. Efficiencies and background fractions as a function of the true and reconstructed neutrino energies for ^{6}He in water in Setup-II.

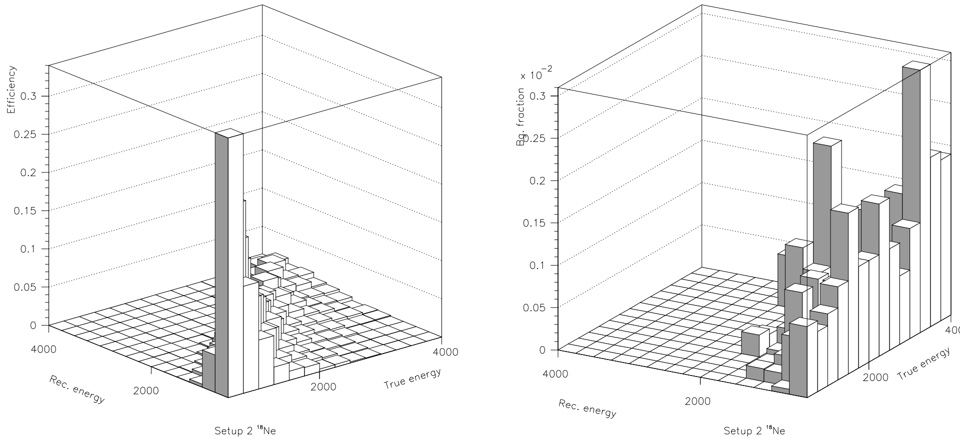

Figure 5.14. Efficiencies and background fractions as a function of the true and reconstructed neutrino energies for ^{18}Ne in water in Setup-II.

One possibility to control still better the backgrounds would be to have a tunable γ. In this way one could characterize the signal at a given energy reducing the background coming from higher energy events maximally.

5.1.9 Setup-3

The neutrino spectra for Setup-3 extends up to a few GeV, well in the deep inelastic regime, where a tracking calorimeter (possibly a massive version of MINOS) could offer better performance than water. The performance of such a device (a 40 kiloton magnetized calorimeter) for the case of the Neutrino Factory has been extensively studied [CDG00] [C+00]. However, the neutrino energy for that setup was higher (mean energy of about 25 GeV to compare with mean energy of about 5 GeV here) and the charge of the muon had to be measured, which is not the case here. We expect a similar performance, with efficiencies better than 30% and background fractions better than 10^{-4}. We also assume that the neutrino energy can be reconstructed also for CC events. Energy bins of 1 GeV will be considered and we discard events with neutrino energies below 1 GeV.

5.1.10 Optimization of the SPS β-beam

The following sensitivity plots are used to optimize the physics performance of different β-beams:

- Sensitivity to CP violation: region on the plane (θ_{13}, δ) where the phase δ can be distinguished from both $\delta = 0°$ and $\delta = 180°$ for any best fit value of θ_{13}, at 99% confidence level or better.
- Sensitivity to θ_{13}: region on the plane (θ_{13}, δ) where the angle θ_{13} can be distinguished from $\theta_{13} = 0$ for any best fit value of δ, at 99% confidence level or better.

5.1.10.1 Optimal γ for the CERN-Fréjus baseline

One frequently considered standard setup adopts the CERN-Fréjus baseline $L = 130$ km and $\gamma = 60/100$ for ^{6}He/^{18}Ne [Mez03] [BLM04]. This setup appears to be far from optimal even if the baseline is kept fixed. A higher-γ beam increases the event rate and allows the energy dependence of the signal to be analyzed. Taking the identical γ's for ^{6}He and ^{18}Ne, figure 5.15 shows the γ-dependence of the 99% CL δ and θ_{13} sensitivity, as defined above. The stars indicate the values of the setup corresponding to $\gamma = 60/100$. Clearly the CP-violation sensitivity is significantly better for larger γ. For $\gamma \geqslant 100$ the sensitivity to CP violation and θ_{13} changes rather slowly. This is not surprising, since increasing γ at fixed baseline does not reduce the flux significantly at low energies (see figure 5.16), just as for a Neutrino Factory. In the absence of backgrounds, there is no penalty associated with higher γ, although in practice, the non-negligible backgrounds result in a small decrease in θ_{13} sensitivity at higher γ, for some values of δ.

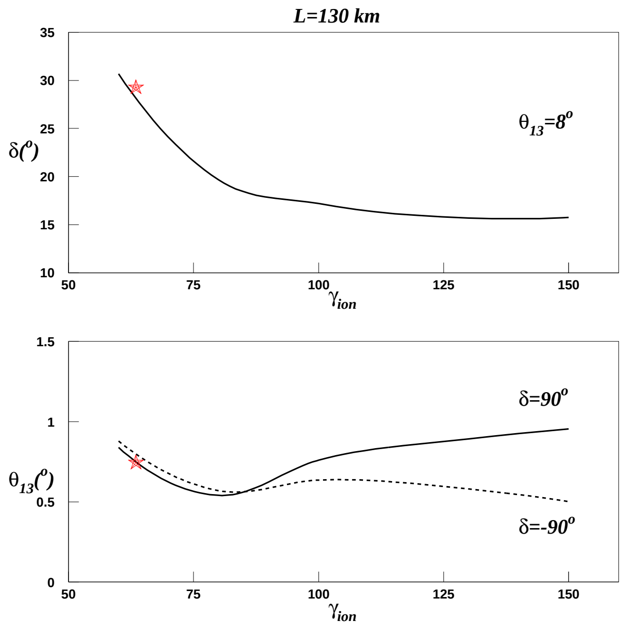

Figure 5.15. γ-dependence of 99% confidence level δ sensitivity at $\theta_{13} = 8°$ (top) and θ_{13} sensitivity (bottom) for $\delta = +90°$ (solid) and $\delta = -90°$ (dashed), assuming $L = 130$ km and $\gamma(^6\text{He}) = \gamma(^{18}\text{Ne})$. The stars indicate the values for the $\gamma = 60/100$ option.

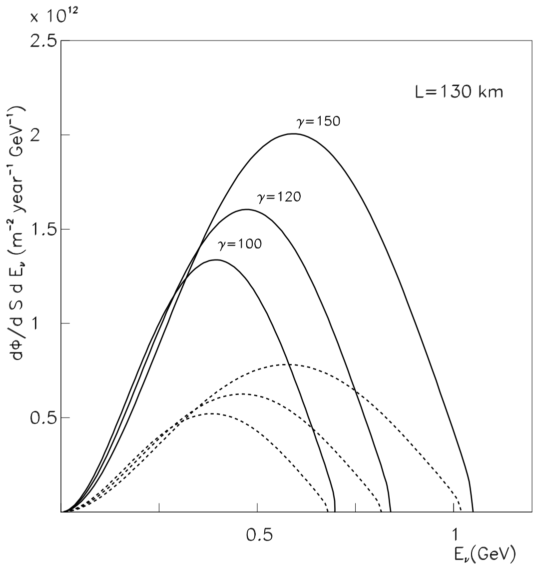

Figure 5.16. Energy spectra of ν_e (dashed) and $\bar{\nu}_e$ (solid) at $L = 130\,\mathrm{km}$ for $\gamma = 100, 120,$ 150.

Although there is no unique optimal γ within the wide range $\gamma = 100$—150 when the baseline is fixed to $L = 130$ km, we will take for illustration an intermediate $\gamma = 120$ to define Setup-4; a different choice of $\gamma > 100$ will not make a significant difference.

There appears to be no advantage to the asymmetric choice $\gamma(^{18}\mathrm{Ne})/\gamma(^{6}\mathrm{He}) =$ 1.67. The asymmetric option is always comparable in sensitivity to a symmetric one with the smaller γ of the two, so a symmetric γ configuration is adopted for Setup-4.

5.1.10.2 Optimal L for maximum ion acceleration $\gamma = 150$

As stated before, physics performance should improve with increasing γ, if the baseline is correspondingly scaled to remain close to the atmospheric oscillation maximum, due to the (at least) linear increase in rate with γ. This growth in sensitivity eventually saturates for a water detector, which becomes inefficient in reconstructing neutrino energies in the inelastic regime. Figure 5.17, where the number of CC appearance candidates selected (for unit oscillation probability) is plotted as a function of γ (for γ/L fixed), confirms this expectation. Saturation occurs for $\gamma \simeq 400$, above the maximum acceleration possible at the CERN-SPS, since the flux is still large in the quasi-elastic region (see figure 5.16).

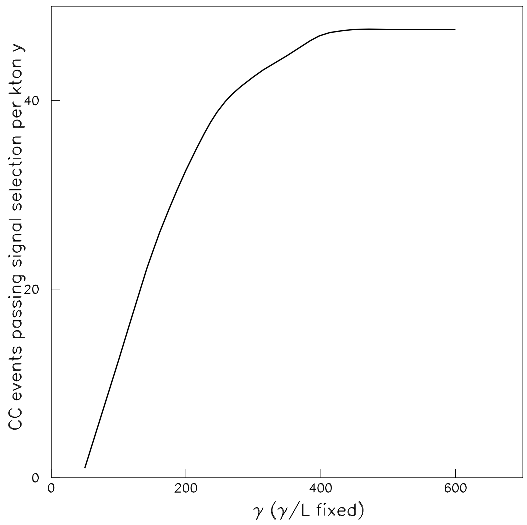

Figure 5.17. Number of CC appearance candidates (from ^{18}Ne) for unit oscillation probability, as a function of γ, holding γ/L fixed.

Fixing γ to the CERN-SPS maximum value we next study the optimal baseline and how the symmetric γ setup compares with the asymmetric one.

Figure 5.18 shows the $|\delta|$ and θ_{13} sensitivities as a function of the baseline for $\gamma = 150/150$ and the asymmetric case $\gamma = 150/250$. The best CP sensitivity is achieved around $L \simeq 300(350)$ km for symmetric (asymmetric) beams. The baseline dependence of θ_{13} sensitivity leads to similar conclusions, although the importance of choosing the optimum baseline is more pronounced. A significant loss of θ_{13} sensitivity results if the baseline is too short, as in Setup-4.

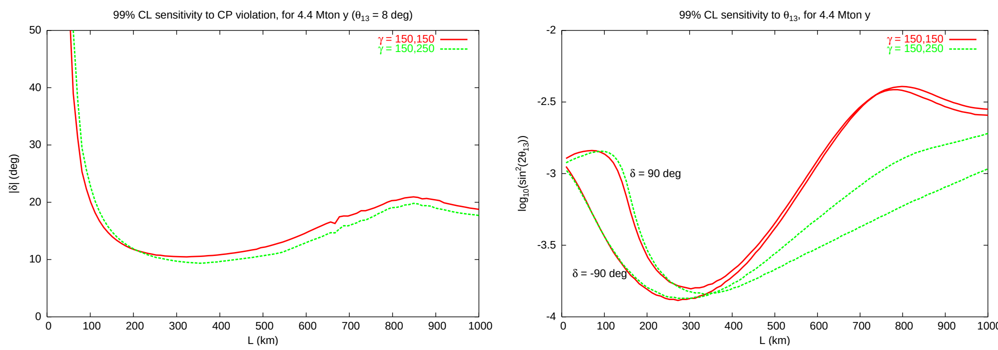

Figure 5.18. Left: minimum value of $|\delta|$ distinguishable from 0 and 180° at 99% CL (for $\theta_{13} = 8°$) vs. baseline for $\gamma = 150/150$ (red) and $\gamma = 150/250$ (green). Right: minimum value of θ_{13} distinguishable from 0 at 99% CL (for $\delta = +90°$ and $\delta = -90°$ as shown).

Setup-5 is hence defined as $\gamma = 150/150$ for $L = 130$ km. Similar results are expected for the asymmetric option $\gamma = 150/250$ with slightly shorter baseline.

5.1.11 Determination of θ_{13} and δ

The simultaneous measurement of θ_{13} and δ is affected by correlations [C+00] and the so called intrinsic degeneracy [BCGGC+01], which results in either a proliferation of disconnected regions of parameter space, where the oscillation probabilities are very similar to be distinguished, or artificially large uncertainties in both parameters when these regions overlap.

As has been discussed before, these degeneracies can be resolved either combining different experiments with different E/L or matter effects, or exploiting, whenever this is possible, the energy dependence of the signal within one experiment.

One of the main advantages of going to higher energies and longer baselines in the β-beam is precisely to have some significant energy resolution which allows to resolve these degeneracies.

5.1.11.1 Setups 1–3

In figure 5.19 we compare the reach concerning CP-violation on the plane (θ_{13}, δ), i.e. the range of parameters where it is possible to distinguish with a 99% CL, δ from 0 or 180° for the different setups and 10 years of running in each case. We assume that both ions are bunched and accelerated simultaneously. We thus include the results from the measurement of both polarities. The remaining oscillation parameters are fixed close to their best fit values.

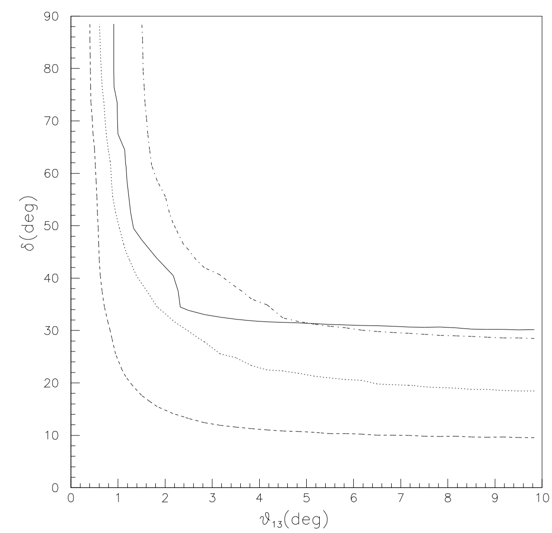

Figure 5.19. Region where δ can be distinguished from $\delta = 0°$ or $\delta = 180°$ with a 99% CL for Setup-1 (solid), Setup-2 with the UNO-type detector of 400 kton (dashed) and with the same detector with a factor 10 smaller mass (dashed-dotted). In all cases we consider 10 years of running time for both polarities.

The solid line corresponds to the Setup-1. The dashed lines correspond to Setup-2 for the UNO detector described in the previous section and for a detector scaled down by a factor of 10. Surprisingly the small water Cerenkov in Setup-2 performs similarly to the UNO detector in Setup-1, while the performance of the latter in Setup-2 is spectacular and clearly comparable with the Neutrino Factory. One of the reasons for this improvement is precisely the resolution of correlations. This can be seen in fig. 5.20, where we compare the result of the fits for setups 1, 2 and 3. While the intrinsic degeneracies are present for the low-energy option, they tend to get resolved in the higher one, even with the smaller detector.

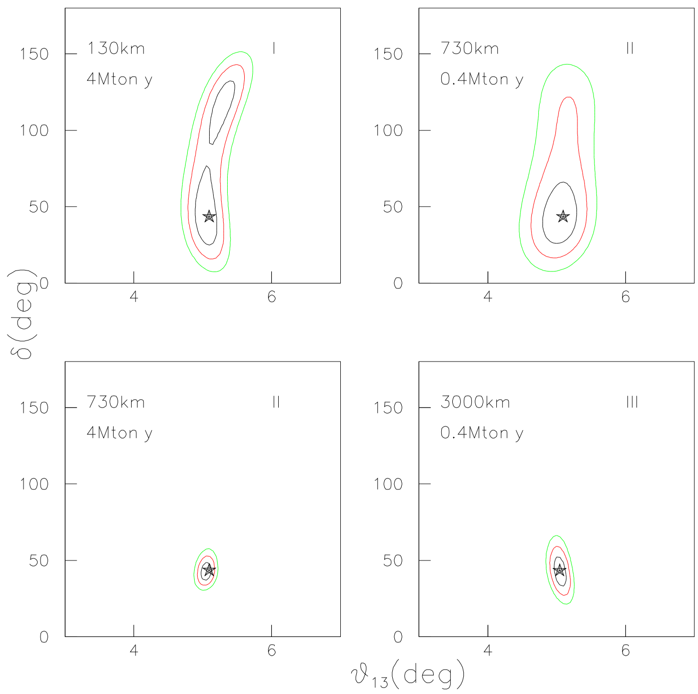

Figure 5.20. 1, 2 and 3 σ contours on the plane (θ_{13}, δ) in the setups 1, 2 for the 40 kton and 400 kton detectors and for Setup-3 in 10 years of running time. The "true" values of the parameters are indicated by a star.

The necessity to suppress backgrounds due to charge misidentification forces a very stringent cut in the momentum of the muon when searching for "wrong sign" muons at the Neutrino Factory. This cut translates in practice to throwing away neutrino energies below 5 GeV, thus losing precious spectral information. In that respect, the presence of two neutrino species in the Neutrino Factory is a disadvantage, compared with the β-beam, where one has only one neutrino species and the ability to identify low energy muons in water, separating them clearly from backgrounds (as opposed to a tracking calorimeter, where a muon of momentum less than about 1 GeV cannot be easily separated from the pion background).

Although other systematic errors, such as the knowledge of the flux or the error on the backgrounds and efficiencies have not been included in this study, they are very unlikely to change the conclusion concerning the comparison of the three setups of the β-beam, since they would affect them in a similar manner. However all systematic errors should be included in a fair comparison of the β-beam and the Neutrino Factory, since they might be quite different in both machines.

5.1.11.2 Setups 4–6

Figure 5.21 compares the CP-violation and θ_{13} exclusion plots for the three setups assuming, for the moment, that the discrete ambiguities in sign(Δm^2_{23}) and sign(cos θ_{23}) can be ignored because correct assignments have been made. Also included for reference is the previously considered Setup-1. Although the highest γ option remains best, the performance of Setup-5 is comparable. Even the sensitivity of the much-improved CERN-Fréjus scenario in Setup-4 is considerable. Although only the range (− 90°, + 90°) is shown, to make it easier to read the y-scale, the region around 180° has a similar pattern.

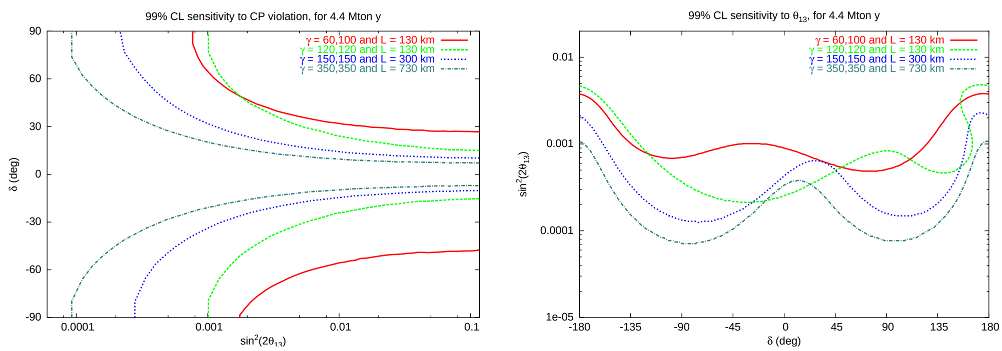

Figure 5.21. Left: CP-violation exclusion plot at 99% CL for the three reference setups 4 (dashed), 5 (dotted) and 6 (dashed-dotted) compared with the standard (solid) setup 1. Right: exclusion plot for θ_{13} at 99% CL with the same setups. The discrete ambiguities are assumed to be resolved.

Figure 5.22 shows typical fits for the three setups at several true values of θ_{13} and δ. While both setups 5 and 6 manage to resolve the intrinsic degeneracy essentially everywhere in the sensitivity range, this is not the case for Setup-4; there (when the fake solution gets closer to and merges with the true one) the errors in θ_{13} and δ are sometimes strongly enhanced by the intrinsic degeneracy. This effect is not necessarily noticeable in the exclusion plot for CP violation.

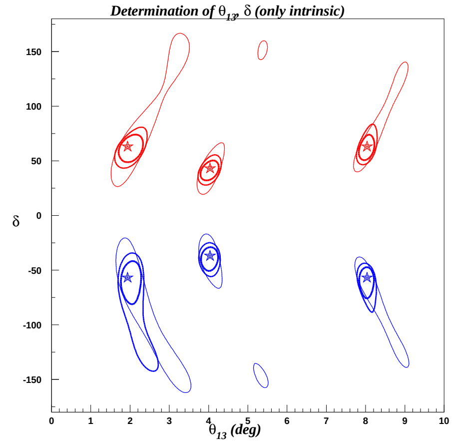

Figure 5.22. Determination of (θ_{13}, δ) at 99% CL for setups 6 (thicker line), 5 (intermediate) and 4 (thinner line) and six different true values of the parameters indicated by the stars, assuming the correct sign(Δm^2_{23}) and sign$(\cos\theta_{23})$.

5.1.12 Determination of sign(Δm^2_{23})

The sign of Δm^2_{23} is an essential missing piece of information to determine the structure of the neutrino mass matrix. The measurement of this quantity cannot be done from the measurement of neutrino oscillations in vacuum, so matter effects need to be sizable. In Setup-I, matter effects are too small to allow the determination of this unknown, however this is no longer the case for the intermediate baseline setup.

In figure 5.23 we show the exclusion plot for the sign of Δm^2_{23} on the plane (θ_{13}, δ) at 99% CL. The measurement of the sign is possible in a very significant region of parameter space. In particular for the largest detector, it can be measured for $\theta_{13} \geqslant 4°$, simultaneously with θ_{13} and δ.

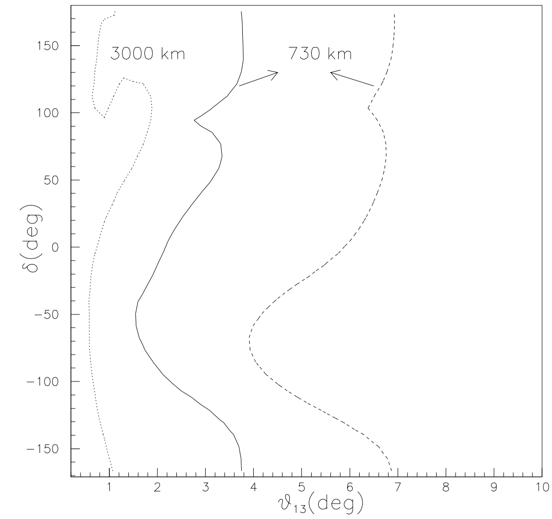

Figure 5.23. Regions where the true sign(Δm^2_{23}) = + 1 can be measured at 99% CL (i.e. no solution at this level of confidence exists for the opposite sign). The lines correspond to Setup-2 with the 400 kton water Cerenkov (solid) and the 40 kton one (dashed) in 10 years of running time.

5.1.13 Effect of the Eight-fold Degeneracies

By the time any β-beam begins, it is probable that a number of uncertainties in the oscillation parameters besides θ_{13} and δ will remain, in particular the discrete ambiguity in sign(Δm^2_{23}) or the octant of θ_{23}. Both questions are theoretically important and the possibility of answering them with a β-beam is attractive. These ambiguities are problematic, if they can't be resolved, because they can bias the determination of the parameters (θ_{13}, δ), that is, the solutions surviving with the wrong assignment of the sign and/or the octant lie at different values of θ_{13} and δ than the true ones.

Generically, an eight-fold degeneracy of solutions appears when only the golden channel is measured and no energy dependence is available. There are two solutions in the absence of the discrete ambiguities, the true and the intrinsic one. Each gets an false image for the wrong assignment of the sign [MN01], for the octant [FL96] [BMW02a] and for both.

The intrinsic solution and its three images are strongly dependent on the neutrino energy and therefore can be excluded, in principle, when the energy dependence of the oscillation signal is significant. On the other hand images of the true solution are energy independent and impossible to resolve unless there are additional measurements (e.g. disappearance measurements or the silver channel), or when there are significant matter effects.

Figure 5.24 shows fits including the discrete ambiguities on the plane (θ_{13}, δ) for the three setups and different choices of the true θ_{13} and δ. In Setup-4 we generically find the full eight-fold degeneracy, while in setups 5 and 6 the intrinsic solution and its images are typically excluded, thanks to the stronger energy dependence.

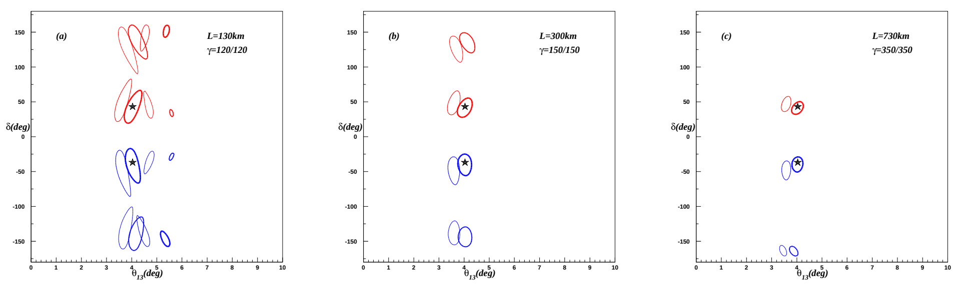

Figure 5.24. Solutions for (θ_{13}, δ) for the true values $\delta = \pm\, 40$ and $\theta_{13} = 4°$ in (a) Setup-4, (b) Setup-5 and (c) Setup-6 without discrete ambiguities, with the sign, octant and mixed ambiguities ordered from thicker to thinner-line contours.

Some general observations concerning these results include:

- Presence of the intrinsic degenerate solution or its images as in Setup-4 is problematic, because it implies a significant increase in the measurement errors of θ_{13} and δ (as shown in figure 5.22) for some values of δ.
- When only the images of the true solution survive, as in setups 5 and 6, they interfere with the measurement of θ_{13} and δ by mapping the true solution to another region of parameter space. In vacuum [MN01] [BCGGC+01]:
  - Wrong sign: $\theta_{13} \to \theta_{13}$, $\delta \to \pi - \delta$
  - Wrong octant: $\theta_{13} \to \tan\theta_{23}\,\theta_{13} + \mathcal{O}(\Delta m^2_{12})$, $\sin\delta \to \cot\theta_{23}\sin\delta$

  Since these different regions occur for different choices of the discrete ambiguities they cannot overlap and one ends with a set of distinct measurements of θ_{13}, δ with different central values but similar errors (see the middle and right plots of figure 5.24).
- In vacuum, CP violating solutions are mapped into CP violating solutions, therefore the effects of degeneracies on the exclusion plot for CP violation are often small, even when degeneracies are a problem. In matter, on the other hand, δ shifts in the fake solutions are enhanced by matter effects and for some central values of (θ_{13}, δ) the fake solutions may move closer to the CP conserving lines than the true solution, resulting in an apparent loss of sensitivity to CP violation. This effect is visible in figure 5.24 where the fake-sign solution, which in vacuum should be located at $\sim -140°$ for $\delta = -40°$, gets shifted towards the CP conserving line for longer baselines where matter effects are larger.

Figures 5.25 and 5.26 show the range of (θ_{13}, δ) where sign(Δm^2_{23}) and sign($\cos\theta_{23}$) can be measured respectively. Asymmetric γ options are also included, since there are some differences. As expected, sensitivity to the discrete ambiguities is better for large θ_{13} and larger γ. In Setup-4 there is essentially no sensitivity anywhere on the plane.

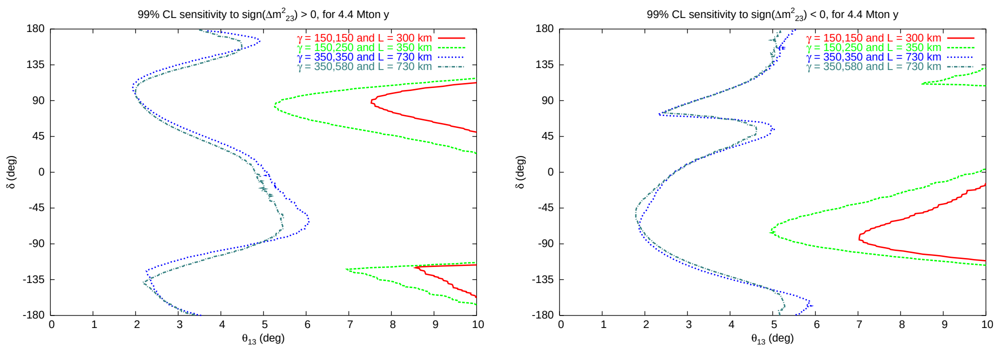

Figure 5.25. Region on the plane (θ_{13}, δ) in which sign(Δm^2_{23}) can be measured at 99% CL for $\theta_{23} = 40.7°$ and positive (left) and negative (right) Δm^2_{23}. Symmetric and asymmetric beam options are shown for Setup-5 (300 km, solid and dashed, respectively) and Setup-6 (730 km, dotted and dash-dotted). There is no sensitivity for Setup-5.

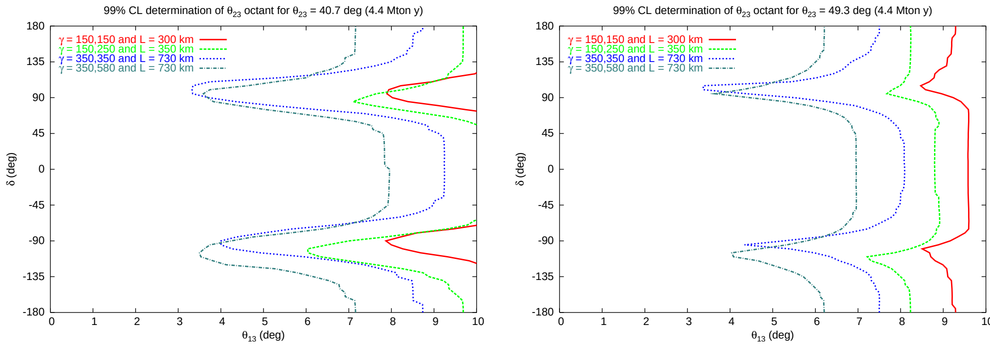

Figure 5.26. Region on the plane (θ_{13}, δ) in which sign$(\cos\theta_{23})$ can be measured at 99% CL for $\theta_{23} = 40.7°$ (left) and $\theta_{23} = 49.3°$ (right). Setups 5 (300 km, solid: symmetric, dashed: asymmetric) and 6 (730 km, dotted: symmetric, dash-dot: asymmetric) are shown. There is no sensitivity for Setup-5.

Sensitivity to the discrete ambiguities and their bias in the determination of the parameters θ_{13} and δ could be significantly improved if data for any of the setups is combined with $\nu_\mu \rightsquigarrow \nu_\mu$ disappearance measurements, for instance in a superbeam experiment. This combination is studied in [DFMR05] for the original β-beam with significant improvement in sensitivity to the mass hierarchy, even without matter effects.

One of the most important limitations of the β-beam, compared to the superbeam or the Neutrino Factory, is its inability to measure the atmospheric parameters (θ_{23}, Δm^2_{23}) with precision. At the very least, information from T2K phase-I should be included, since otherwise the uncertainty on these parameters will seriously compromise sensitivity to θ_{13} and δ. Synergies in resolving degeneracies, between the β-beam and T2K, should also be exploited.

Another interesting observation is that atmospheric neutrinos can be measured in the same megaton detector considered here. A study [HMS05] combining atmospheric data with T2K phase-II has found a large improvement in sensitivity of the latter to both discrete ambiguities when θ_{13} is not too small ($> 4°$).

5.2 Electron-Capture Beam

Yet another kind of neutrino beam, which shares many properties with the β-beam, is the electron-capture beam. The option of a monochromatic neutrino beam from atomic electron capture in ^{150}Dy was first presented in [Lin04] and then discussed both in its physics reach and the machine feasibility in the CERN Joint Meeting of BENE/ECFA for Future Neutrino Facilities in Europe. The subsequent analysis showed that this conception could become operational when combined with the recent discovery of nuclei far from the stability line, having super allowed spin-isospin transitions to a giant Gamow-Teller resonance kinetically accessible [A+04]. Thus the rare-earth nuclei above ^{146}Gd have a small enough half-life for electron capture processes. In an electron-capture facility, the neutrino energy is dictated by the chosen boost of the ion source and the neutrino beam luminosity is concentrated at a single known energy.

Electron capture is the process in which an atomic electron is captured by a proton of the nucleus leading to a nuclear state of the same mass number A, replacing the proton by a neutron and a neutrino. Its probability amplitude is proportional to the atomic wavefunction at the origin, so that it becomes competitive with the nuclear β^+ decay at high Z. Kinetically, it is a two body decay of the atomic ion into a nucleus and the neutrino, so that the neutrino energy is well defined and given by the difference between the initial and final nuclear mass energies (Q_{EC}) minus the excitation energy of the final nuclear state. In general, the high proton number Z nuclear beta-plus decay (β^+) and electron-capture (EC) transitions are very disfavored, because the energetic window open Q_β/Q_{EC} does not contain the important Gamow-Teller strength excitation seen in (n, p) reactions. There are a few cases, however, where the Gamow-Teller resonance can be populated (see fig. 5.27) having the occasion of a direct study of the "missing" strength. For the rare-earth nuclei above ^{146}Gd, the filling of the intruder level $h_{11/2}$ for protons opens the possibility of a spin-isospin transition to the allowed level $h_{9/2}$ for neutrons, leading to a fast decay. The properties of a few examples of interest for neutrino beam studies are given in Table 5.4.

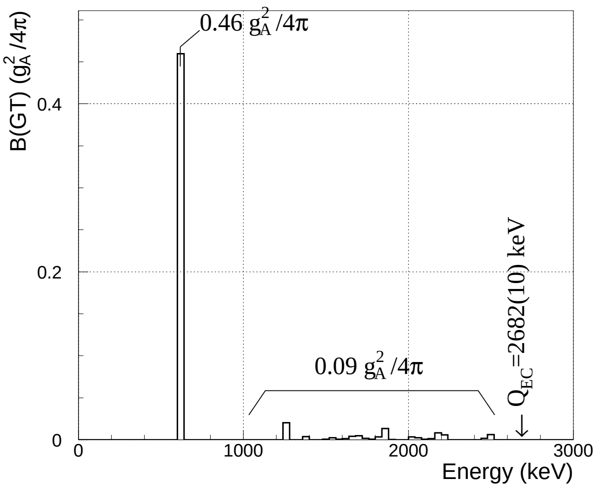

Figure 5.27. Gamow-Teller strength distribution in the EC/β^+ decay of ^{148}Dy.

Decay	$T_{1/2}$	BR_ν	EC/β^+	E_{GR}	Γ_{GR}	Q_{EC}	E_ν	ΔE_ν
$^{148}\mathrm{Dy} \to ^{148}\mathrm{Tb}^*$	3.1 m	1	96/4	620	$\simeq 0$	2682	2062	$\simeq 0$
$^{150}\mathrm{Dy} \to ^{150}\mathrm{Tb}^*$	7.2 m	0.64	100/0	397	$\simeq 0$	1794	1397	$\simeq 0$
$^{152}\mathrm{Tm}2^- \to ^{152}\mathrm{Er}^*$	8.0 s	1	45/55	4300	520	8700	4400	520
$^{150}\mathrm{Ho}2^- \to ^{150}\mathrm{Dy}^*$	72 s	1	77/33	4400	400	7400	3000	400

Table 5.4. Four fast decays in the rare-earth region above ^{160}Gd leading to the giant Gamow-Teller resonance. Energies are given in keV. The first column gives the life-time, the second the branching ratio of the decay to neutrinos, the third the relative branching between electron capture and β^+, the fourth is the position of the giant GT resonance, the fifth its width, the sixth the total energy available in the decay, the seventh is the neutrino energy $E_\nu = Q_{\mathrm{EC}} - E_{\mathrm{GR}}$ and the eighth its uncertainty.

A proposal for an accelerator facility with an EC neutrino beam follows the structure of the β-beam, with partially stripped EC-unstable ions accelerated at the PS and stored in a decay ring with straight sections pointing to the detector. It shares some of the most attractive features of the β-beam concept: the integration of the CERN accelerator complex and the synergy between particle physics and nuclear physics communities.

5.2.1 Neutrino Flux

A neutrino (of energy E_0) that emerges from radioactive decay in an accelerator will be boosted in energy. In the laboratory, the measured energy distribution as a function of the angle (θ) and Lorentz gamma (γ) of the ion at the moment of decay can be expressed as $E = E_0/[\gamma\,(1-\beta\cos\theta)]$. The angle θ in the formula expresses the deviation between the actual neutrino detection and the ideal detector position in the prolongation of one of the long straight sections of the decay ring. The neutrinos are concentrated inside a narrow cone around the forward direction. If the ions are kept in the decay ring longer than the half-life, the energy distribution of the neutrino flux arriving to the detector in absence of neutrino oscillations is given by:

$$\frac{d^2N_\nu}{dS\,dE} = \frac{1}{\Gamma}\frac{d^2\Gamma_\nu}{dS\,dE}N_{\mathrm{ions}} \simeq \frac{\Gamma_n}{\Gamma}\frac{N_{\mathrm{ions}}}{\pi L^2}\gamma^2\,\delta(E - 2\,\gamma\,E_0) \tag{5.6}$$

with a dilation factor $\gamma \gg 1$ and where N_{ions} is the total number of ions decaying to neutrinos. For an optimum choice with $E \sim L$ around the first oscillation maximum, Eq. (5.6) says that lower neutrino energies E_0 in the proper frame give higher neutrino fluxes. The number of events will increase with higher neutrino energies as the cross section increases with energy. To conclude, in the forward direction the neutrino energy is fixed by the boost $E = 2\,\gamma\,E_0$, with the entire neutrino flux concentrated at this energy. As a result, such a facility will measure the neutrino oscillation parameters by changing the γ's of the decay ring (energy dependent measurement) and there is no need of energy reconstruction in the detector.

Furthermore, the neutrino beam has only one flavor, ν_e, so there are no beam backgrounds, as is the case for the β-beam and the Neutrino Factory (when the charge of the produced muon can be measured), and in contrast to the conventional neutrino beams from the decay of pions.

5.2.2 Physics with an EC-beam

An EC-beam can work at different energies to exploit the energy dependence of the neutrino oscillation. It is able to study the detailed energy dependence by means of choosing different γ and so different discrete energy values. In an electron capture facility the neutrino energy is dictated by the chosen boost of the ion source and the neutrino beam luminosity is concentrated at a single known energy which may be chosen at will for the values in which the sensitivity for the (θ_{13}, δ) parameters is higher. This is in contrast to beams with a continuous spectrum, where the intensity is shared between sensitive and non sensitive regions.

Moreover, the definite energy would help in the control of both the systematics and the detector background. By knowing the expected energy of the neutrino, a mild cut in the reconstructed neutrino energy can get rid of most of the detector background. In the beams with a continuous spectrum, the neutrino energy *has to* be reconstructed in the detector. In water-Cerenkov detectors, this reconstruction is made from supposed quasielastic events by measuring both the energy and direction of the charged lepton. This procedure suffers from non-quasielastic background, from kinematic deviations due to the nuclear Fermi momentum and from dynamical suppression due to exclusion effects [Ber72].

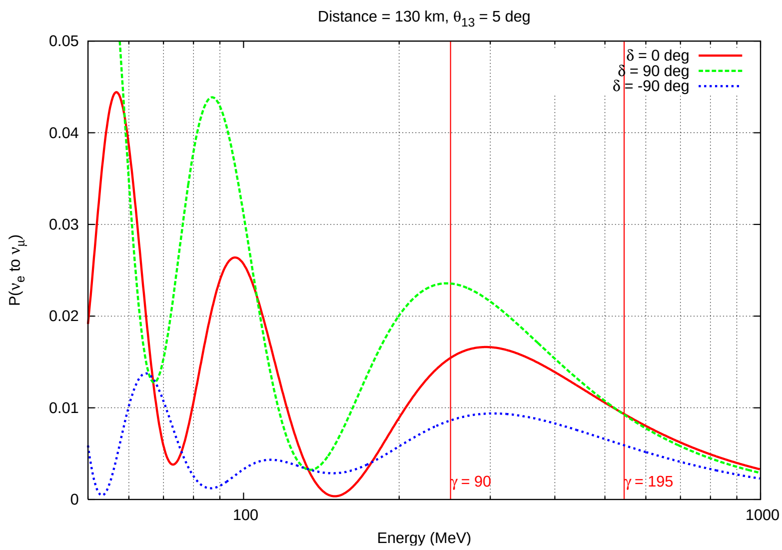

Figure 5.28. The appearance probability $P(\nu_e \rightsquigarrow \nu_\mu)$ for neutrino oscillations as a function of the LAB energy E, with fixed distance between source and detector and for $\theta_{13} = 5°$. The three curves refer to different values of the CP violating phase δ. The two vertical lines are the energies proposed.

5.2.3 Considered Setups

There have been two setups proposed for an electron capture beam. Both combine two different energies for the same ^{150}Dy ion. In all cases the fluxes are 10^{18} decaying ions/year, a water Cerenkov detector with fiducial mass of 440 kton and both appearance ($\nu_e \rightsquigarrow \nu_\mu$) and disappearance ($\nu_e \rightsquigarrow \nu_e$) events are considered.

- Setup I is associated with a five year run at $\gamma = 90$ plus a five year run at $\gamma = 195$ (the maximum energy achievable at present SPS), with a baseline $L = 130$ km from CERN to Fréjus.
- Setup II is associated with a five year run at $\gamma = 195$ plus a five year run at $\gamma = 440$ (the maximum achievable at the upgraded SPS with proton energy of 1000 GeV), with a baseline $L = 650$ km from CERN to Canfranc.

5.2.3.1 Perspectives for Setup I

For the Setup I the corresponding fit with two parameters is shown in figure 5.29 for selected values of θ_{13} from 8° to 1° and covering a few values of δ. As observed, the principle of an energy dependent measurement (illustrated here with two energies) is working to separate out the two parameters. With this configuration, the precision obtainable for the mixing is much better than that for the CP phase. As seen, even mixings of 1° are still distinguishable. And this is for a simultaneous fit of θ_{13} and δ.

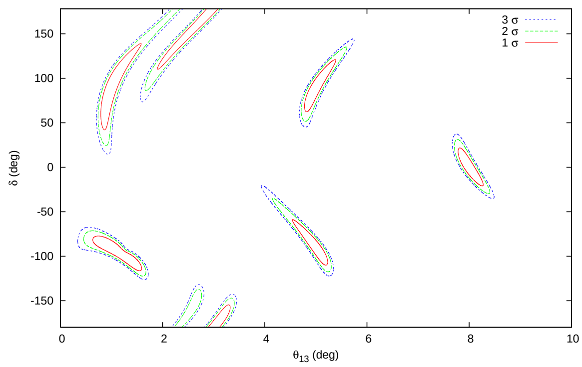

Figure 5.29. Simultaneous fits of (θ_{13}, δ) in Setup I for different central “true” values of these parameters.

At the time of the operation of this proposed facility, it could happen that the connecting mixing θ_{13} is already known from the approved experiments for second generation neutrino oscillations, like Double CHOOZ, Daya-Bay, T2K and NOVA. To illustrate the gain obtainable in the sensitivity to discover CP violation from the previous knowledge of θ_{13}, the precision to obtain δ is then much better than that of figure 5.29, as will be shown later.

5.2.3.2 Perspectives for Setup II

In the case of Setup II the longer baseline for $\gamma = 195$ leads to a value of E/L well inside the second oscillation (see fig. 5.30). In that case the associated strip in the (θ_{13}, δ) plane has a more pronounced curvature, so that the two parameters can be better disentangled. The results of the simultaneous fits for several central chosen values of (θ_{31}, δ) are given in figure 5.31 for a two-parameter fit. Qualitatively, one notices that the precision reachable for the CP phase is better than that in the case of Setup I. This improvement in the CP phase determination has been obtained with the neutrino channel only, using two appropriate different energies. One may discuss in this Setup II the sensitivity to discover $\theta_{13} \neq 0$ by giving the χ^2 fit, for each θ_{13}, to the value $\theta_{13} = 0$. This is given in fig. 5.32. Although it is somewhat dependent on the δ-value, most values of θ_{13} are in general distinguishable for zero.

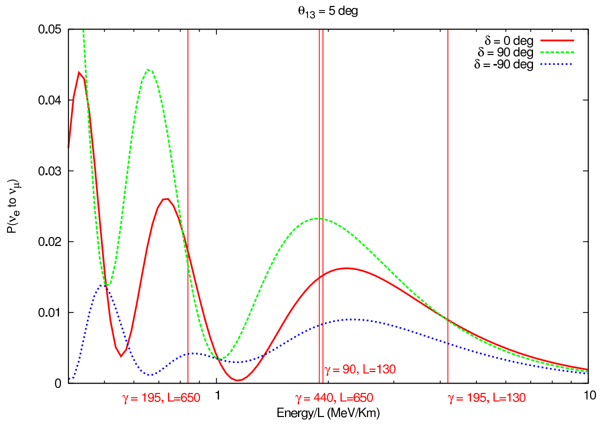

Figure 5.30. $P(\nu_e \rightsquigarrow \nu_\mu)$ as a function of E/L for a fixed $\theta_{13} = 5°$. The three curves refer to different values of the CP violating phase δ. The vertical lines are the energies for both Setup I and II.

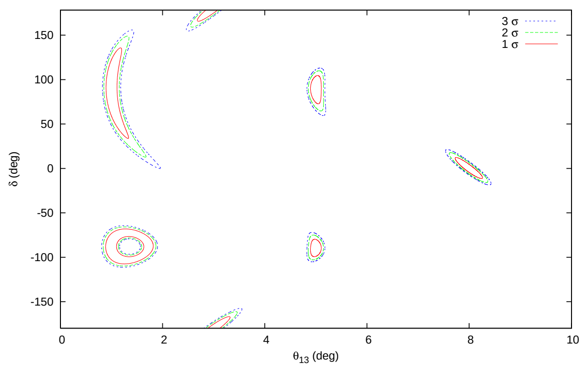

Figure 5.31. Simultaneous fits of (θ_{13}, δ) in Setup II for different central "true" values of these parameters.

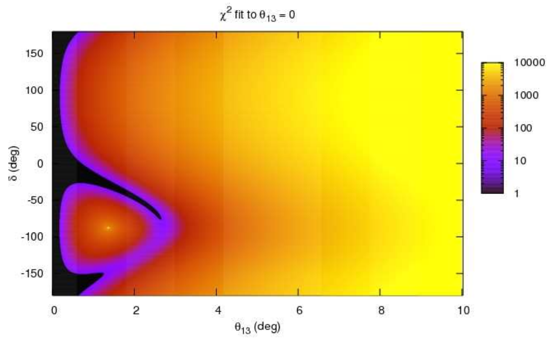

Figure 5.32. Setup II. Sensitivity to $\theta_{13} \neq 0$ for a two parameter (θ_{13}, δ) fit. The black region is indistinguishable from $\theta_{13} = 0$, and the rest is colored according to the value of the χ^2 fit to $\theta_{13} = 0$.

The corresponding exclusion plots for CP violation in the two setups are compared when both θ_{13} and δ are unknown. The sensitivity to discover CP violation has been studied by obtaining the χ^2 fit for $\delta = 0°$, $180°$ if the assumed value is a given δ. For 99% CL, the sensitivities to see CP violation in both Setups are compared in fig. 5.33. In both cases, a two-parameter fit is assumed, i.e., θ_{13} previously unknown. For Setup I, a non-vanishing CP violation becomes significant for $\theta_{13} > 4°$, with values of the phase δ around 30° or larger to be distinguished from zero. For Setup II, the sensitivity to CP violation is better and significant even at 1° in certain cases, depending on the hemisphere for the value of the phase δ.

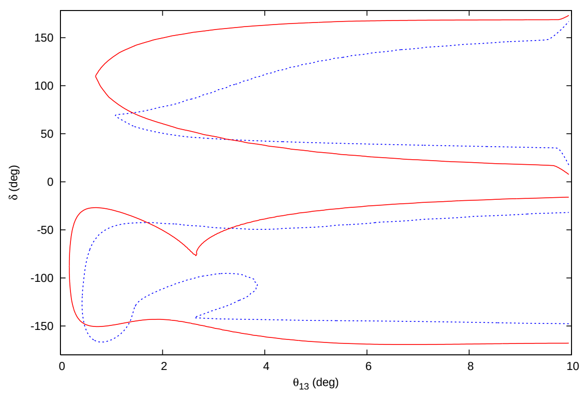

Figure 5.33. CP violation exclusion plot at 99% CL, if θ_{13} is still unknown, for the two reference setups: I (broken blue line) and II (continuous red line).

If θ_{13} is previously known, the corresponding analysis for the sensitivity to discover CP violation is presented in figure 5.34. In this case, the χ^2 fit is made with the single parameter δ. One may notice that the improvement in this sensitivity is impressive, suggesting that going step by step in the determination of the neutrino oscillation parameters by means of several generation experiments is very rewarding. Setup II provides better sensitivity to the discovery of CP violation than Setup I. In the best case, i.e., θ_{13} already known at the time of the proposed experiment with Setup II, figure 5.35 shows the sensitivity to discover CP violation to be distinguished from $\delta = 0°, 180°$.

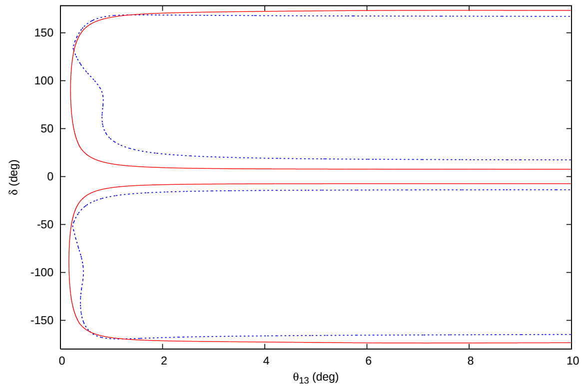

Figure 5.34. CP violation exclusion plot at 99% CL, if θ_{13} is previously known, for the two reference Setups: I (broken blue line) and II (continuous red line).

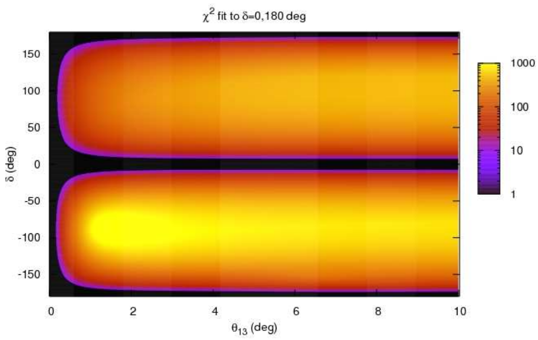

Figure 5.35. Setup II. CP violation sensitivity for the statistical distribution of events depending on the single parameter δ, assuming previous information on the value of θ_{13}.

Although the proposed scenarios look very promising, the ambiguities coming from the sign of Δm^2_{23} and the octant of θ_{23} can be problematic and reduce significantly the sensitivity. The eight-fold degeneracy of solutions is expected to appear if only one energy is measured. The power of the EC-beam to disentangle these ambiguities, combining several energies and/or combining its measurements with another facility remains to be explored.

Chapter 6
Conclusions

The experimental discovery of neutrino oscillations has shown the existence of neutrino masses, otherwise extremely difficult to measure because of their smallness. Furthermore, it has shown that a mixing between flavor and mass eigenstates happens in the leptonic sector, in a way similar to the quark sector with the CKM matrix. All this has expanded the minimal Standard Model to accommodate 7 new fundamental parameters (the three neutrino masses, three mixing angles and a CP-violating phase). Past experiments have been able to measure with some precision the two squared-mass differences (Δm^2_{12}, Δm^2_{23}) and two mixing angles (θ_{12}, θ_{23}), and to set an upper limit to the other mixing angle (θ_{13}). Still, a direct measure of $\theta_{13} > 0$ and the phase δ is missing, and if $\delta \neq 0°, 180°$ it would imply the existence of CP violation in the leptonic sector. Finally, a couple of unknowns remain among the oscillation parameters: the mass hierarchy (the sign of Δm^2_{23}), and the octant of θ_{23}.

The current and next generation of long baseline neutrino experiments are in a good position to find the unknown fundamental parameters, and measure with better precision the ones already known. There are exciting proposals that would be able to explore a sizable region in the parameter space, like a Neutrino Factory, Superbeams, β-beams and EC-beams. Each one has its own merits and drawbacks.

Superbeams and the Neutrino Factory are affected in their ultimate sensitivity by the uncertainty in the hadronic production cross-sections. In particular, the measure of $p + \text{target} \to \pi^{\pm}, K$ differential cross-sections provided by HARP will be an essential input for current experiments like K2K and MiniBooNE as well as for the future facilities and also for atmospheric neutrino experiments.

A Neutrino Factory from muon storage rings, with muon energies of a few dozen GeV, still provides the ultimate sensitivity through wrong sign muon searches. At the hypothetical time of the Neutrino Factory, the value of the parameters θ_{13} and δ may still be both unknown and will have to be simultaneously measured.

In the determination of the unknown parameters there are two effects that spoil their measurement, in the form of correlations and degeneracies. For a given pair (θ_{13}, δ) the reconstruction of the true solution comes out in general accompanied by fake ones, which might interfere severely with the measurement of CP violation. One of the fake solutions comes from the intrinsic correlation between δ and θ_{13}, and the others come from the discrete ambiguities in sign(Δm^2_{23}) and the octant of θ_{23}.

There is an enormous potential to eliminate these degeneracies in combining the data from a superbeam and the Neutrino Factory. Because of the sizable matter effects, Neutrino Factory baselines that are optimal to measure CP violation imply a considerably smaller ratio L/E than in the proposed superbeam facilities. A Neutrino Factory with baseline $L = 2810$ km together with a superbeam would be able to resolve all the degeneracies and deliver a clean measurement of θ_{13} and leptonic CP violation down to $\theta_{13} > 1°$. Even for values down to $\theta_{13} > 0.5°$ only the ambiguity associated with the octant of θ_{23} would remain a problem, if θ_{23} were far from maximal.

β-beams and EC-beams could provide a sensitivity of the same order, but to get a fair comparison with superbeams and the Neutrino Factory a full study of how they are affected by systematics and, for EC-beams, the degeneracies, must be done.

Superbeams and the Neutrino factory are two successive steps in the path towards the discovery of leptonic CP violation, with a solid perspective offered by the combination of their physics results.

Appendix A
Software Tools and Design

A.1 Numerical Simulations

Exploration of the physics reach of the different long baseline neutrino experiments requires an intensive numerical simulation.

The neutrino flux must be correctly characterized for the source, which in the case of the Neutrino Factory, β-beams or EC-beams comes from the analytic formulas, but for superbeams it requires a full Monte Carlo simulation. The fluxes must be then extrapolated to the detector, by solving the exact oscillation formulas, and taking into account matter effects, which implies the diagonalization of the hermitian neutrino mass matrix. The number of events recorded in the detector must be evaluated knowing the different cross-sections involved —to know them and estimate both the efficiencies and the background rejection factors typically involve a heavy Monte Carlo simulation. Finally, all this process must be carried out for all the allowed parameter space, to get the χ^2 that allow for the reconstruction of the oscillation parameters (or to compute the limits in the sensitivity to them).

A.2 Implementation

To address the numerical simulations we have developed several programs. The results of the Monte Carlo simulations of the neutrino source and the detector have been taken from external sources.

Because the parameter space is very large, the efficiency of the programs has been addressed with special care. We chose to program the basic components in C++ so we could benefit of the fast execution of its compiled binaries, and also follow an object-oriented approach to carry the simulations in an orderly manner. We have defined the following main interfaces:

- **Nature**, a *singleton* that knows about the true values of the oscillation parameters, including neutrino masses and mixing angles. It is the object who answers questions of the type "what is the probability of the oscillation $\nu_e \rightsquigarrow \nu_\mu$ for a certain energy?".

- **Source**, which knows about the neutrino fluxes $\frac{d^2N_i}{dE\,d\Omega}$ as a function of the energy, including every type of neutrino present in the beam, and in particular, including the beam background. It hides the details of the beam production, whether it is known analytically like the case of a Neutrino Factory or a β-beam, or from a Monte Carlo simulation, like in the case of superbeams.

- **Detector**, which knows about the kind of detector and its fiducial mass, the cross sections σ_i for each neutrino species and energy, as well as the efficiencies ϵ_i and detector backgrounds.

- **Experiment**, composed of a source and detector located at a certain distance. It is the object that internally will compute the number of events (for any requested energy bin) taking into account everything that is necessary:

$$\begin{aligned}
\left(\frac{d^2N_i}{dE\,\mathrm{dS}}\right)_{\exp} &= \sum_j \frac{1}{L^2}\frac{d^2N_i}{dE\,d\Omega}P_{j\rightsquigarrow i} \\
\left(\frac{dN_i}{\mathrm{dS}}\right)_{\exp} &= \int\left(\frac{d^2N_i}{dE\,\mathrm{dS}}\right)_{\exp} dE \\
\frac{dN_{\mathrm{evt}\,i}}{dE} &= \epsilon_i\left(\frac{d^2N_i}{dE\,\mathrm{dS}}\right)_{\exp}\sigma_i \\
N_{\mathrm{evt}\,i} &= \int \frac{dN_{\mathrm{evt}\,i}}{dE}\,dE
\end{aligned}$$

These parts appear as classes and functions in a library, which also has a Python interface. A χ^2-based study usually follows the generation of the large datasets for the observables in a neutrino experiment.

We have also developed a few programs to explore interactively the neutrino oscillation phenomenology. They can be used to quickly get familiarized with the neutrino oscillation physics by playing with the parameters and seeing their effect immediately. For the same reason, they can be used as an educational tool.

The programs include the graphical evolution of the neutrino wavefunction for 2-family mixing, as seen in the mass and flavor basis, an automatic plotter for the neutrino flavor oscillation as a function of the energy or the baseline, for a given set of oscillation parameters and taking into account if desired the MSW effect, and an automatic fitter to see rough reconstructions in the (θ_{13}, δ) plane for a certain combination of neutrino experiments. These programs have been developed with the Qt toolkit.

Another step in the availability of software is the conversion of the analysis programs in web tools. Simply accessing a web page is much easier than downloading and compiling a program, and so we have also developed some programs to explore online the phenomenology of neutrino oscillations.

A.3 Availability

Scientific research requires reproducibility. To develop our programs we have made extensive use of Free Software. Free Software is not about price, it is about freedom. It is software that respects the *user*'s freedom, the freedom to

- run it for any purpose
- study how it works and adapt it to your needs (access to the source code is a precondition for this)
- make copies for your colleagues/friends
- modify it to improve it or suit it for your needs, and release your improvements to the rest of the community

Making our code available to the rest of the community and relying only on Free Software ensures that anyone can trace, check and reproduce our results. It also allows others to push research further without having to start from scratch.

In our work we have in particular much profited from

- The GNU Scientific Library (GSL) (`http://www.gnu.org/software/gsl/`)
  A numerical library for C/C++ that provides a wide range of mathematical routines.
- Qt (`http://trolltech.com/products/qt`)
  A C++ graphics library.
- Maxima (`http://maxima.sourceforge.net/`)
  A system for the manipulation of symbolic and numerical expressions.

as well as many other utilities like gnuplot, emacs, gcc and CVS.

All our libraries and interactive programs can be downloaded from the following location: `http://evalu29.uv.es/software/`

Our web tools can be found at `http://evalu29.uv.es/pop/`

Several persons have showed their interest in using the programs we have developed. We are very pleased for it, and would like to continue encouraging this practice.

Bibliography

[A+02] M. Anfreville et al., *The drift chambers of the Nomad experiment*, Nucl. Instrum. Meth. **A481**, 339–364 (2002), hep-ex/0104012.

[A+03] B. Autin et al., *The acceleration and storage of radioactive ions for a neutrino factory*, J. Phys. **G29**, 1785–1796 (2003), physics/0306106.

[A+04] A. Algora et al., *beta decay of Dy-148: Study of the Gamow-Teller giant state by means of total absorption spectroscopy*, Phys. Rev. **C70**, 064301 (2004).

[BCGGC+01] J. Burguet-Castell, M. B. Gavela, J. J. Gomez-Cadenas, P. Hernandez and O. Mena, *On the measurement of leptonic CP violation*, Nucl. Phys. **B608**, 301–318 (2001), hep-ph/0103258.

[BCGGC+02] J. Burguet-Castell, M. B. Gavela, J. J. Gomez-Cadenas, P. Hernandez and O. Mena, *Superbeams plus neutrino factory: The golden path to leptonic CP violation*, Nucl. Phys. **B646**, 301–320 (2002), hep-ph/0207080.

[Ber72] J. Bernabeu, *Quasielastic electron and neutrino interactions and the exclusion effects*, Nucl. Phys. **B49**, 186–205 (1972).

[BGL+04] G. D. Barr, T. K. Gaisser, P. Lipari, S. Robbins and T. Stanev, *A three-dimensional calculation of atmospheric neutrinos*, Phys. Rev. **D70**, 023006 (2004), astro-ph/0403630.

[BKS98] J. N. Bahcall, P. I. Krastev and A. Y. Smirnov, *Where do we stand with solar neutrino oscillations?*, Phys. Rev. **D58**, 096016 (1998), hep-ph/9807216.

[BLM04] J. Bouchez, M. Lindroos and M. Mezzetto, *Beta beams: Present design and expected performances*, AIP Conf. Proc. **721**, 37–47 (2004), hep-ex/0310059.

[BMW02a] V. Barger, D. Marfatia and K. Whisnant, *Breaking eight-fold degeneracies in neutrino CP violation, mixing, and mass hierarchy*, Phys. Rev. **D65**, 073023 (2002), hep-ph/0112119.

[BMW02b] V. Barger, D. Marfatia and K. Whisnant, *Off-axis beams and detector clusters: Resolving neutrino parameter degeneracies*, Phys. Rev. **D66**, 053007 (2002), hep-ph/0206038.

[BooNe] E. Church et al. (BooNe Collaboration), *A proposal for an experiment to measure muon-neutrino → electron-neutrino oscillations and muon-neutrino disappearance at the Fermilab Booster: BooNE*, FERMILAB-PROPOSAL-0898.

[C+] M. G. Catanesi et al., *Proposal to study hadron production for the neutrino factory and for the atmospheric neutrino flux*, CERN-SPSC-99-35.

[C+00] A. Cervera et al., *Golden measurements at a neutrino factory*, Nucl. Phys. **B579**, 17–55 (2000), hep-ph/0002108.

[C+07] M. G. Catanesi et al., *Particle identification algorithms for the HARP forward spectrometer*, Nucl. Instrum. Meth. **A572**, 899–921 (2007).

[Cas02] D. Casper, *The nuance neutrino physics simulation, and the future*, Nucl. Phys. Proc. Suppl. **112**, 161–170 (2002), hep-ph/0208030.

[CDG00] A. Cervera, F. Dydak and J. Gomez Cadenas, *A large magnetic detector for the neutrino factory*, Nucl. Instrum. Meth. **A451**, 123–130 (2000).

[Cer04] A. Cervera Villanueva, *First physics results from the HARP experiment at CERN*, (2004), hep-ex/0406053.

[DFMR05] A. Donini, E. Fernandez-Martinez and S. Rigolin, *Appearance and disappearance signals at a beta-beam and a super-beam facility*, Phys. Lett. **B621**, 276–287 (2005), hep-ph/0411402.

[DGH99] A. De Rujula, M. B. Gavela and P. Hernandez, *Neutrino oscillation physics with a neutrino factory*, Nucl. Phys. **B547**, 21–38 (1999), hep-ph/9811390.

[DHH68] R. J. Davis, D. S. Harmer and K. C. Hoffman, *Search for neutrinos from the sun*, Phys. Rev. Lett. **20**, 1205–1209 (1968).

[DMM02] A. Donini, D. Meloni and P. Migliozzi, *The silver channel at the neutrino factory*, Nucl. Phys. **B646**, 321–349 (2002), hep-ph/0206034.

[FHL01] M. Freund, P. Huber and M. Lindner, *Systematic exploration of the neutrino factory parameter space including errors and correlations*, Nucl. Phys. **B615**, 331–357 (2001), hep-ph/0105071.

[FL96] G. L. Fogli and E. Lisi, *Tests of three-flavor mixing in long-baseline neutrino oscillation experiments*, Phys. Rev. **D54**, 3667–3670 (1996), hep-ph/9604415.

[FW] R. Fruhwirth and E. Widl, *Track-based alignment using a Kalman filter technique*, Prepared for 1st LHC Detection Alignment Workshop, Geneva, Switzerland, 4-6 Sep 2006.

[G+] M. Goodman et al., *Physics Potential and Feasibility of UNO*, PREPRINT-SBHEP01-3.

[Gai00] T. K. Gaisser, *Atmospheric neutrino flux: A review of calculations*, Nucl. Phys. Proc. Suppl. **87**, 145–151 (2000), hep-ph/0001027.

[GALLEX99] W. Hampel et al. (GALLEX Collaboration), *GALLEX solar neutrino observations: Results for GALLEX IV*, Phys. Lett. **B447**, 127–133 (1999).

[GCH02] J. J. Gomez-Cadenas and D. A. Harris, *Physics opportunities at neutrino factories*, Ann. Rev. Nucl. Part. Sci. **52**, 253–302 (2002).

[Gee98] S. Geer, *Neutrino beams from muon storage rings: Characteristics and physics potential*, Phys. Rev. **D57**, 6989–6997 (1998), hep-ph/9712290.

[HARP06] M. G. Catanesi et al. (HARP Collaboration), *Measurement of the production cross-section of positive pions in p Al collisions at 12.9-GeV/c*, Nucl. Phys. **B732**, 1–45 (2006), hep-ex/0510039.

[HARP07] M. G. Catanesi et al. (HARP Collaboration), *Measurement of the production of charged pions by protons on a tantalum target*, Eur. Phys. J. **C51**, 787–824 (2007), arXiv:0706.1600 [hep-ex].

[HLW02] P. Huber, M. Lindner and W. Winter, *Superbeams versus neutrino factories*, Nucl. Phys. **B645**, 3–48 (2002), hep-ph/0204352.

[HMS05] P. Huber, M. Maltoni and T. Schwetz, *Resolving parameter degeneracies in long-baseline experiments by atmospheric neutrino data*, Phys. Rev. **D71**, 053006 (2005), hep-ph/0501037.

[K2K] T. Ishida (K2K Collaboration), *Neutrino oscillation experiment K2K at KEK-PS (KEK E362)*, Prepared for International Workshop on Kaon, Muon, and Neutrino Physics and the Future at KEK, Tsukuba, Japan, 31 Oct - 1 Nov 1997.

[K2K06] M. H. Ahn et al. (K2K Collaboration), *Measurement of neutrino oscillation by the K2K experiment*, Phys. Rev. **D74**, 072003 (2006), hep-ex/0606032.

[Kos] D. G. Koshkarev, *Proposal for a Decay Ring to Produce Intense Secondary Particle Beams at the SPS*, CERN/ISR-DI/74-62.

[Lin04] M. Lindroos, Neutrino beta beam facility, Workshop on Terrestrial and Cosmic Neutrinos, Leptogenesis and Cosmology - Benasque Center for Science, 21 July 2004, Talk in http://benasque.ecm.ub.es/benasque/2004neutrinos/.

[Mez03] M. Mezzetto, *Physics reach of the beta beam*, J. Phys. **G29**, 1771–1776 (2003), hep-ex/0302007.

[MMS+03] V. Martemyanov, L. Mikaelyan, V. Sinev, V. Kopeikin and Y. Kozlov, *The Kr2Det project: Search for mass-3 state contribution |U(e3)|**2 to the electron neutrino using a one reactor - two detector oscillation experiment at Krasnoyarsk underground site. ((B))*, Phys. Atom. Nucl. **66**, 1934–1939 (2003), hep-ex/0211070.

[MN01] H. Minakata and H. Nunokawa, *Exploring neutrino mixing with low energy superbeams*, JHEP **10**, 001 (2001), hep-ph/0108085.

[MNS62] Z. Maki, M. Nakagawa and S. Sakata, *Remarks on the unified model of elementary particles*, Prog. Theor. Phys. **28**, 870 (1962).

[Pau77] W. Pauli, *Fhunf Arbeiten zum Ausschliessungsprinzip und zum Neutrino*, Wissenschaftliche Buchgesellschaft (1977).

[Pon57] B. Pontecorvo, *Mesonium and antimesonium*, Sov. Phys. JETP **6**, 429 (1957).

[RC53] F. Reines and C. L. Cowan, *A Proposed experiment to detect the free neutrino*, Phys. Rev. **90**, 492–493 (1953).

[Ric00] B. Richter, *Conventional beams or neutrino factories: The next generation of accelerator-based neutrino experiments*, (2000), hep-ph/0008222.

[SAGE99] J. N. Abdurashitov et al. (SAGE Collaboration), *Measurement of the solar neutrino capture rate by SAGE and implications for neutrino oscillations in vacuum*, Phys. Rev. Lett. **83**, 4686–4689 (1999), astro-ph/9907131.

[SNO01] Q. R. Ahmad et al. (SNO Collaboration), *Measurement of the charged current interactions produced by B-8 solar neutrinos at the Sudbury Neutrino Observatory*, Phys. Rev. Lett. **87**, 071301 (2001), nucl-ex/0106015.

[SuperBeams01] J. J. Gomez-Cadenas et al. (CERN working group on Super Beams Collaboration), *Physics potential of very intense conventional neutrino beams*, (2001), hep-ph/0105297.

[Super-Kamiokande98] Y. Fukuda et al. (Super-Kamiokande Collaboration), *Evidence for oscillation of atmospheric neutrinos*, Phys. Rev. Lett. **81**, 1562–1567 (1998), hep-ex/9807003.

[Super-Kamiokande99] T. Kajita (Super-Kamiokande Collaboration), *Atmospheric neutrino results from Super-Kamiokande and Kamiokande: Evidence for nu/mu oscillations*, Nucl. Phys. Proc. Suppl. **77**, 123–132 (1999), hep-ex/9810001.

[T2K01] Y. Itow et al. (The T2K Collaboration), *The JHF-Kamioka neutrino project*, (2001), hep-ex/0106019.

[Wan73] C. L. Wang, *Empirical formula for pion production in proton proton collisions up to 1500 gev*, Phys. Rev. **D7**, 2609–2613 (1973).

[ZS88] H. W. Zaglauer and K. H. Schwarzer, *THE MIXING ANGLES IN MATTER FOR THREE GENERATIONS OF NEUTRINOS AND THE MSW MECHANISM*, Z. Phys. **C40**, 273 (1988).

[Zuc01] P. Zucchelli, *A novel concept for a anti-nu/e neutrino factory*, (2001), hep-ex/0107006.

[Zuc02] P. Zucchelli, *A novel concept for a anti-nu/e / nu/e neutrino factory: The beta beam*, Phys. Lett. **B532**, 166–172 (2002).